The Dissertation Committee for Robert Gardiner Stevens IV
certifies that this is the approved version of the following dissertation:

Alignment Effects of Hydrogen Reflection by Si(100)

Committee:

Greg O. Sitz, Supervisor

Michael Downer

Manfred Fink

Graeme Henkelman

John Keto

Alignment Effects of Hydrogen Reflection by Si(100)

by

Robert Gardiner Stevens IV, B.S.

DISSERTATION

Presented to the Faculty of the Graduate School of

The University of Texas at Austin

in Partial Fulfillment

of the Requirements

for the Degree of

DOCTOR OF PHILOSOPHY

THE UNIVERSITY OF TEXAS AT AUSTIN

August 2015

Alignment Effects of Hydrogen Reflection by Si(100)

Publication No. _____

Robert Gardiner Stevens IV, Ph.D.
The University of Texas at Austin, 2015

Supervisor: Greg O. Sitz

Previous scattering experiments have shown a dependence of reflectivity on the alignment of the angular momentum vector of molecular hydrogen incident on a surface of Pd(111), Isakson 2001. In these past experiments orthohydrogen was preferentially aligned relative to the surface by preparing the J=3 state. This J=3 state has multiple values for its m_J quantum number and therefore there is a distribution in J=3 alignment. Within I will discuss the design of a new laser that can efficiently pump parahydrogen from the J=0 state, which has no distribution in m_J and therefore the resulting J=2 state can be aligned with much better precision. Evidence suggests (Isakson, 2001) that the perpendicular alignment of the angular momentum vector with respect to the surface (helicopter-type motion) was less reflective than the parallel alignment (cartwheeler-type motion) for orthohydrogen when interacting with Pd(111). Within a study of the preservation of these alignments, both helicopter and cartwheeler, for aligned J=3 initial states will be attempted as

they reflect off of the unreactive Si(100) surface. This study will strongly influence future studies, ones off of reactive surfaces such as Pd(111), and dictate if loss of alignment can explain the perceived decreased reflectivity.

Table of Contents

List of Tables

List of Figures

Chapter 1

Introduction

In the study of dynamics at surfaces our goal is a deterministic equation governing the interaction of molecules as they approach a surface. It is experimentally observed that some molecules in the presence of some surfaces break apart upon that surface and stay partially bound; the molecule is said to **dissociatively adsorb**. This may be misleading because the molecule as a whole no longer exists: it is purely its constituent atoms at this point which are bound to the surface. These atoms may drift over the surface then recombine with another atom to come off the surface as a molecule again; this is **associative desorption**. We wish to know what physical quantities can influence the probability to dissociatively adsorb.

For the apparatus described within, we cannot directly measure molecules that have adsorbed onto the surface. Instead we infer that any molecules that reflect off, i.e.. do not adsorb, can be simply related to the **sticking probability**:

$$1 = P_{sticking} + P_{reflect} \tag{1.1}$$

$P_{sticking}$ is sometimes referred to as the **sticking coefficient**. It is

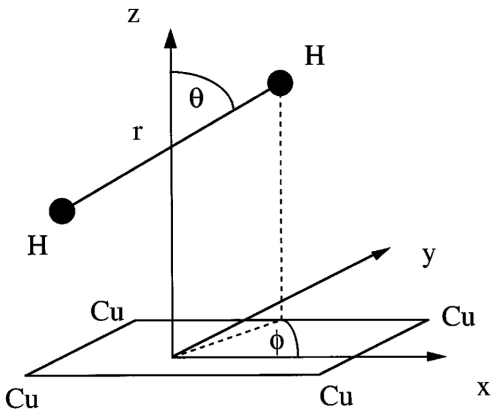

Figure 1.1: Sketch of the coordinate system used in describing diatomic molecules' approach to a surface [1]

$P_{reflect}$ that we can measure directly. This is known as the King and Wells method and is widely established to be accurate for sticking probabilities of 10% and higher.

1.1 The Coordinate System

Let us first describe the standard coordinate system of a diatomic molecule (such as hydrogen) approaching a surface. Figure 1.1 is equivalent to the description below.

We describe the surface in Cartesian coordinates. The surface has extent in x and y, can be assumed to be perfectly flat for now, and on the length scale of a molecule ($\approx 1\text{Å} = 10^{-8}cm$) the surface is essentially infinite ($\approx 1cm \times 1cm$). The height of the molecule's center of mass above the surface is z.

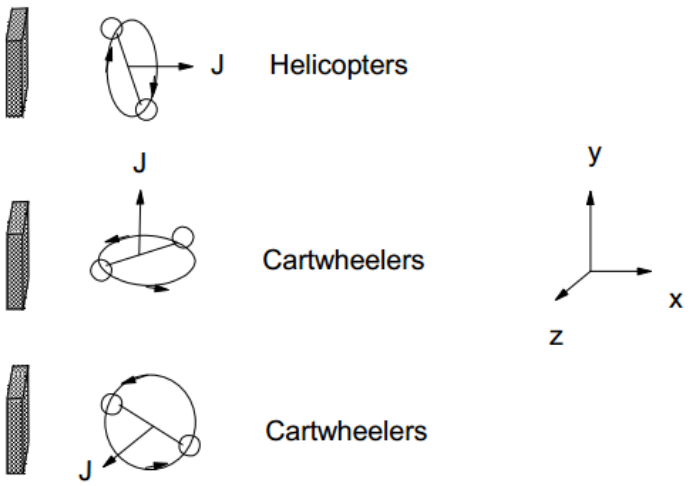

Figure 1.2: This figure depicts the 'cartwheeler' and 'helicopter' definitions described in the text. Source: Isakson [2]

The molecule has its own coordinate system to describe the nuclei and electrons. We will use cylindrical coordinates. There is the bond axis, r, on which both nuclei will lie. Rotations around this axis, variations in ϕ, produce no change. Thus the molecule is symmetric about ϕ and validating our choice of coordinate system. With the last variable, θ we are able to discuss the molecule's **alignment**. It is chosen that $\theta = 0°$ makes the bond axis r parallel to z, thus making the molecule's **J** parallel to the surface normal.

This thesis discusses the effects on alignment during the reflection of hydrogen from an unreactive surface; we are to compare cases where the molecule comes in at $\theta = 90°$ to those where the *average* $\theta = 0°$, but more on that later.

It is useful to define two simple language terms for these different alignments. Molecules that have their bond axis perpendicular to the surface nor-

mal, $\theta = 90°$, are said to be **helicopters** while molecules that have their bond axis parallel to the surface normal, $\theta = 0°$, we define as **cartwheelers**. Figure 1.2 depicts this. In nature, there will be very few true cartwheelers or helicopters and most will be in some mixture of both alignments. We use these terms to simplify our explanations.

With a modicum of physical intuition, one would already suspect that molecules in a helicopter configuration would have a higher probability to adsorb, i.e. higher sticking coefficient, because in this configuration the nuclei are equidistant to the surface atoms and thus would *both* be available to form bonds to the surface atoms. Our goal here is to measure how the alignment is perturbed when reflected from a surface. This is necessary for future experiments which will seek to justify the above conjecture.

1.2 The Lennard-Jones Model

We will digress slightly to discuss a model that is historically significant and provides a qualitative model of gas-surface dynamics. The Lennard-Jones model was first proposed in 1932 in his landmark paper: [22]. Figure 1.3 is a reproduction of a plot in [22] found in [3]. It should be noted that it is *a one-dimensional model*, thus it does not capture any of the orientation effects we wish to discuss.

From figure 1.3 we see the competition of two potential energies: the molecule-surface interaction, curve 1, and the intermolecular interaction, curve 2. What may be misleading at first about this figure is that the distance from

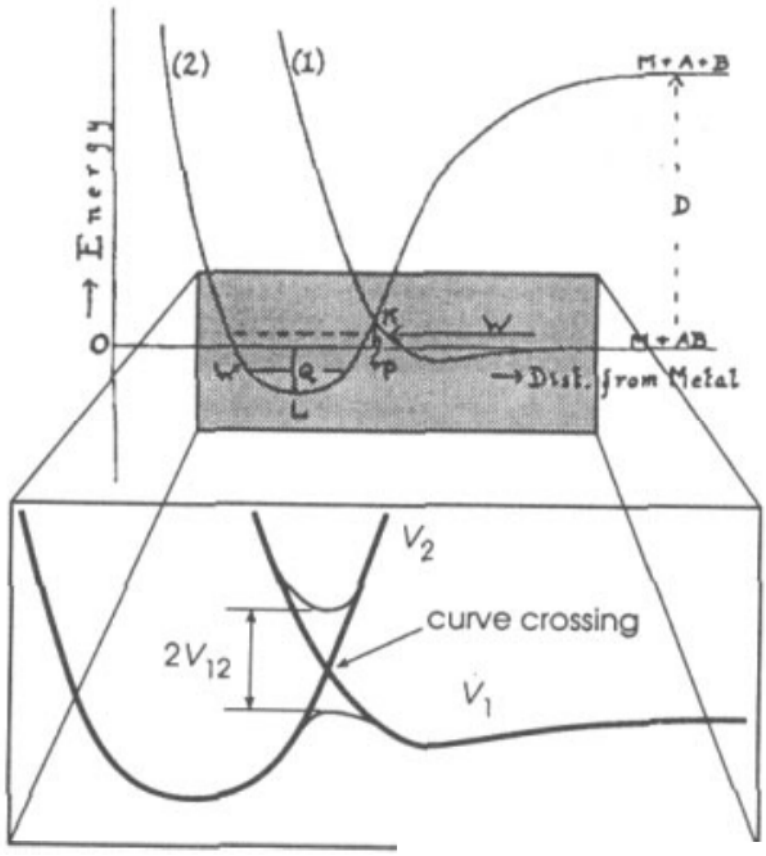

Figure 1.3: A reproduction of the Lennard-Jones potential found in [3]. The top plot shows two competing potential energy curves. Curve 1 is the potential between the surface and the molecule. Curve 2 is the intermolecular potential. The bottom panel shows a zoomed in portion of the crossing point between 1 and 2.

the surface, z, is drawn while the bond length variable, r, is omitted and clearly of primary importance if we wish to discuss increases in that variable (i.e. bond breaking). There is an inconsistency in that the bond is instantaneously elongated when transitioning from curve 1 to curve 2. In Lennard-Jones' own words: "[such diagrams] do not lend themselves to generalization when more than one coordinate is necessary to specify a configuration" [3] from [22]. Figure 1.3 is meant only to aid discussions.

When the molecule is far from the surface, large z, we expect no contribution to the potential, thus curve 1 approaches 0. When it gets arbitrarily close to the surface, small z, we expect some Coulombic repulsion to become exceedingly strong as the electrons of the molecule try to approach the electrons of the surface. One could also think of this as a Fermionic repulsion in which the molecular electrons try to occupy the same states of the surface electrons; the end result is the same: the molecule cannot get too close before it is pushed away.

When the molecule is far from the surface it should only experience the potential binding the nuclei together. Thus curve 2 approaches the molecular binding energy D at large z. Since dissociation on the surface is observed, there must be a potential greater than D corresponding to the atoms breaking their internal bond and forming bonds with the surface at some z value near the surface. The atoms cannot travel into the surface thus another increasing repulsion term for very small z.

As we can see from the figure 1.3, specifically the lower panel, there

is a slight rise in the potential before adsorption can take place regardless of diabatic or adiabatic modelling (see 1.2.1). This is called an **activation barrier** or the **activation energy**. The activation barrier is the minimum kinetic energy a molecule must have in order to be a candidate for adsorption. This is a key concept that will be elaborated on in further models. It is worthwhile to note that not all surfaces have activation barriers and while the surface of interest to this dissertation, silicon, has an extremely large activation barrier and is not the only term resulting in its very low sticking probability. The Lennard-Jones model provides us with this key concept but is very limiting in that this energy must be kinetic. The Lennard-Jones model does not consider alignment of the molecule or surface conditions and thus cannot provide any direct insight for the problem at hand. Nonetheless, it is a useful way point in our discussion.

1.2.1 Digression: Adiabatic vs. Diabatic

The Lennard-Jones model, section 1.2, gets us to a very important physics discussion: **diabatic** versus **adiabatic** approximations.

Take figure 1.3 as an example. In a diabatic approximation curves 1 and 2 are allowed to cross. That is, there are *two* ground states that coexist at the same point in the parameter-space. A molecule that comes in along curve 1 can make a radiation-less transition into curve 2 and then carry on to adsorption. The diabatic approximation has a key feature that can make discussions very confusing: there are multiple ground-states and it depends on

where you are.

In an adiabatic approximation, the two curves are combined to make two other curves, C and D, that do not cross at any point. One of these curves will be *the* ground state and the other will be an excited state that is seldom accessible. This combination process is akin to a rotation of coordinates or change of basis and need not be daunting to new students. Ultimately, we wish to be able to refer to a singular ground state that embodies all the dynamics in our discussion.

1.3 Modern Theory: Simulations & PES

As we progress beyond the Lennard-Jones model, which has severe limitations for this discussion, we will need to look at how modern modelling is performed. These physical simulations are essential to this field; to not briefly describe the key concepts of how a simulation is built up would neglect the many hours and efforts of brilliant scientists' hard work. However, it is the work of *other* scientists and generally outside the scope of this dissertation the exact how of the matter. For a more exhaustive explanation of the methods and techniques, I refer you to Darling and Halloway's excellent, albeit daunting, review article: [3].

1.3.1 Brief Overview of Simulation Methods

As will be apparent in the coming section, the physics equations governing a diatomic molecule interacting with a surface are not trivial. To gain

any sort of foothold on the problem, numerical simulations are required. The end result of these simulations are often times visualized as **Potential Energy Surfaces (PES)**, see section 1.3.2. Largely this discussion will follow that of section 2 in Darling and Holloway [3].

As always in quantum mechanics we start with the time-dependent Schrödinger equation:

$$-i\hbar\frac{\partial\Psi}{\partial t} = H\Psi \tag{1.2}$$

We write the Hamiltonian of the entire system as a series contributions from kinetic (H) and potential (V) energy terms of the nuclei (n) and electrons (e) followed by an interaction potential between the two:

$$H = H_n(\mathbf{R}) + H_e(\mathbf{r_e}) + V_n(\mathbf{R}) + V_e(\mathbf{r_e}) + V_{n-e}(\mathbf{R} - \mathbf{r_e}) \tag{1.3}$$

where $\mathbf{R}$ is the positions of all the nuclei (surface & molecule) and $\mathbf{r_e}$ is the positions of all the electrons.

The full wave-function for the system will be written as:

$$\Psi(\mathbf{R}, \mathbf{r_e}, t) = \Sigma_\nu \chi_\nu(\mathbf{r_e}; \mathbf{R})\psi_\nu(\mathbf{R}, t) \tag{1.4}$$

where $\chi_\nu(\mathbf{r_e}; \mathbf{R})$ is the set of electronic eigenfunctions that depend on both the positions of the electrons and nuclei.

Substituting equations 1.3 and 1.4 into 1.2 results in this hot mess:

$$
\begin{aligned}
-i\hbar\frac{\partial\Psi}{\partial t} &= (H_n(\mathbf{R}) + V_n(\mathbf{R}))\psi_\nu(\mathbf{R},t) \\
&\quad + \Sigma_\mu < \chi_\nu(\mathbf{r_e};\mathbf{R})|H_e(\mathbf{r_e}) + V_e(\mathbf{r_e}) + V_{n-e}(\mathbf{R}-\mathbf{r_e})|\chi_\mu(\mathbf{r_e};\mathbf{R}) > \\
&\quad + \Sigma_\mu C_{\nu\mu}\psi_\mu
\end{aligned}
$$

where all the coupling between nuclear and electronic motions, i.e. how the nuclei move in response to the electron motion, is hidden as $C_{\nu\mu}$:

$$C_{\nu\mu} = \Sigma_N - \frac{1}{m_N}(< \chi_\nu|\nabla_R|\chi_\mu > + \frac{1}{2} < \chi_\nu|\nabla_R^2|\chi_\mu >) \tag{1.5}$$

Here comes our first, and most commonly used, simplification: the **Born-Oppenheimer Approximation (BOA)** in which it is argued that due to the large mass disparity between the electrons and nuclei (at least a factor of $\approx$ 1800) the nuclei will not respond quickly to the electronic motions. The consequence of this is that the derivatives in $C_{\nu\mu}$ are small and subsequently $C_{\nu\mu}$ can be neglected. Periodically the BOA is also called the *adiabatic approximation* which is unnecessarily confusing and will be eschewed here.

We will be using an adiabatic form of the wave-function, which is independent of the BOA, in which the nuclear dependence of the electronic terms will be written parametrically on $\mathbf{R}$:

$$(H_e + V_n + V_e + V_{n-e})\chi_\nu(\mathbf{r_e};\mathbf{R}) = \epsilon_\nu(\mathbf{R})\chi_\nu(\mathbf{r_e};\mathbf{R}) \tag{1.6}$$

Thus we are able to fully separate the nuclear Schrödinger equation:

$$-i\hbar\frac{\partial\psi_\nu(\mathbf{R})}{\partial t} = (H_n + \epsilon_\nu(\mathbf{R}))\psi_\nu(\mathbf{R}) \tag{1.7}$$

Thus we can perform a "boot-strapping" method where we can solve equation 1.7 to find $\epsilon_\nu(\mathbf{R})$, substitute this into equation 1.6, solve, propagate the particles, and repeat. The end result of which is the potential energy surface, i.e. $\epsilon_\nu(\mathbf{R})$, for all the nuclear degrees of freedom.

Solving these equations is far from easy and requires sophisticated techniques such as the **Local Density Approximation (LDA)** and its associated **Generalized Gradient corrections/Approximation (GGA)**. These techniques are strongly dependent on knowing the **eXchange-Correlation function (XC)** which determines how electrons move between states. This is now far beyond the scope of this dissertation and well outside the author's area of expertise.

1.3.2 Potential Energy Surfaces

The end result of the calculations described in section 1.3.1 is an incredibly useful depiction of the molecular-surface interaction. **Potential Energy Surfaces (PES)** are plots widely used in this field depicting contours of constant energy against two of the six relevant coordinates described in section

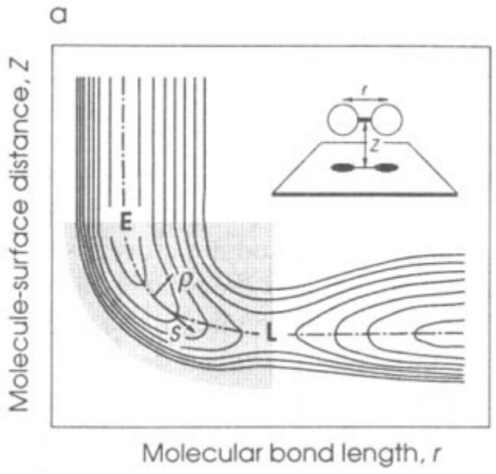

Figure 1.4: A generic PES showing key features as we vary the molecular-surface distance, z, and the resulting molecular bond length, r. This is not for the $H_2/Si(100)$ system. From [3].

1.1. Most often, we will look at PES for molecular distance above the surface, z, and the bond length, r. For a dissociative adsorption process, as z decreases r will rapidly increase once a critical height is reached. This makes the PES resemble an elbow and is the inspiration for the common-language term for these plots: **elbow potentials**. A generic example of one of these plots is shown in figure 1.4.

Looking at figure 1.4, we see a key feature: there is a barrier to desorption. This is the same phenomenon described in the Lennard-Jones model, section 1.2. It is equivalent to say the system is *activated*. There is a minimum energy, the activation energy, the molecule must exceed in order to dissociate. As a result if we were to plot the sticking probability versus incident kinetic energy of the molecule we would see a monotonic function. An example of this

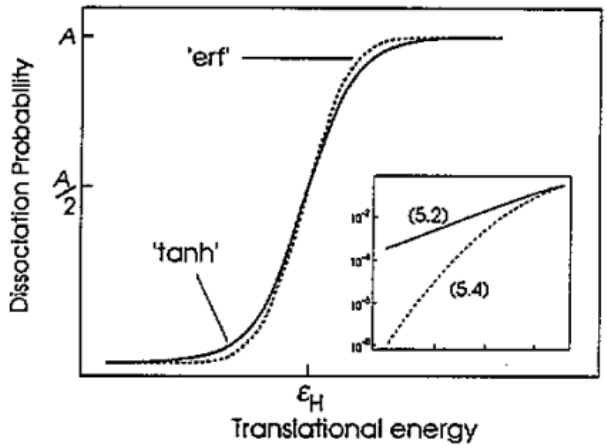

Figure 1.5: A generic sticking probability curve for a system that has a barrier or is activated. This is not for the $H_2/Si(100)$ system. The distinction between which function best describes this model system does not concern us here. From [3].

is shown in figure 1.5.

1.4 All About Silicon

Now that a strong base of fundamentals and language is established we can begin to discuss the specifics of our system. This section will start with a historical overview of the unique problems presented by silicon. From there we will move on to the relatively recent reactivity studies on Si(100) that demonstrate a key assumption in this experiment: the hydrogen will not stick. For all of this we will focus on the Si(100) 2x1 reconstruction since that is the sample we have experimented on.

1.4.1 The Insurmountable Barrier

The sticking coefficient of H_2 on Si(100) was first thought to be 'immeasurably small'. Early efforts to measure this, most prominently J. T. Law [23], found that sticking was approximately 10^{-6} until the surface saturated at approximately 2% of a monolayer (ML) at which point it fell below the lower limit Law could measure: 10^{-9}. Law was able to show that previous adsorption studies mistakenly measured *atomic* hydrogen sticking and molecular hydrogen had a much lower probability.

It was observed that this low sticking probability did not match the energetics of the system. If it were simply the case that the energy barrier were very large then experiments should show that when hydrogen desorbed it should be very energetic. It is not. **Temperature Programmed Desorption (TPD)** studies show that the adsorbed state is energetically favourable with a modest adsorption barrier of .6eV [4]. Figure 1.6 is a schematic showing the energetics akin to the Lennard-Jones model.

1.4.2 Hot Silicon

The first proposed solution to this riddle was phonon-assisted sticking whereby the *temperature of the surface* was suggested to greatly impact the sticking probability. While the effect is true, there is a strong dependence on surface temperature, see figure 1.9, the reasoning is not quite right.

Scanning Tunnelling Microscopy (STM) images, see figure 1.7, show that a clean Si(100) surface *dimerizes* into rows of two silicon atoms

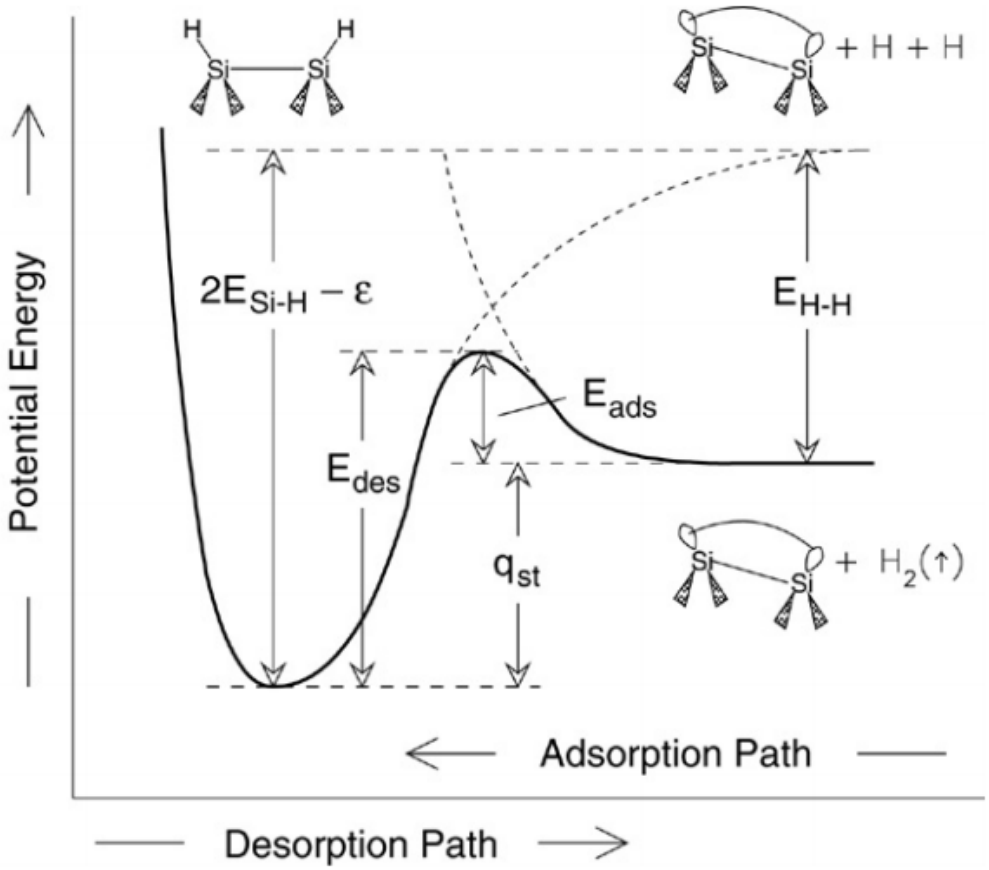

Figure 1.6: A diagram depicted the various energy levels at play in desorption and dissociation on Silicon. The table condenses several measured results for both Si(100) and Si(111). Source: Dürr and Höfer [4]

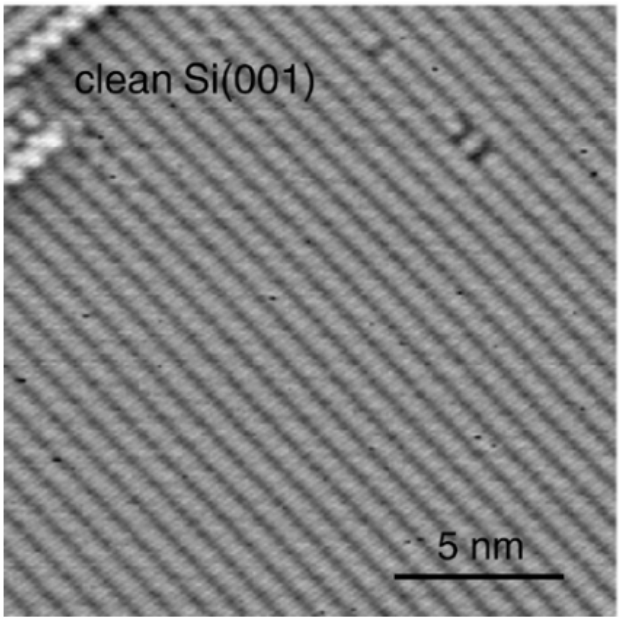

Figure 1.7: STM data showing how a clean Si(100) surface dimerizes into long running rows of pairs of atoms. Plot is taken from Dürr and Höfer [4].

bound together. Silicon, having 4 valence electrons, can make up to 4 molecular bonds. In bulk this means that each silicon atom binds to 4 of its neighbours. This symmetry is broken at the surface and surface atoms are left with 2 dangling bonds. It is energetically favourable to bind to a neighbouring surface atom filling 1 bond and leaving 1 empty. This is known as the 2x1 reconstruction. The side view of the 4x2 reconstruction depicted in figure 1.8 shows the 2x1 reconstruction. The actual 4x2 reconstruction requires neighbouring bonds to buckle in opposite directions. There is very little energy gained in doing this so it is only observed below 200K [4].

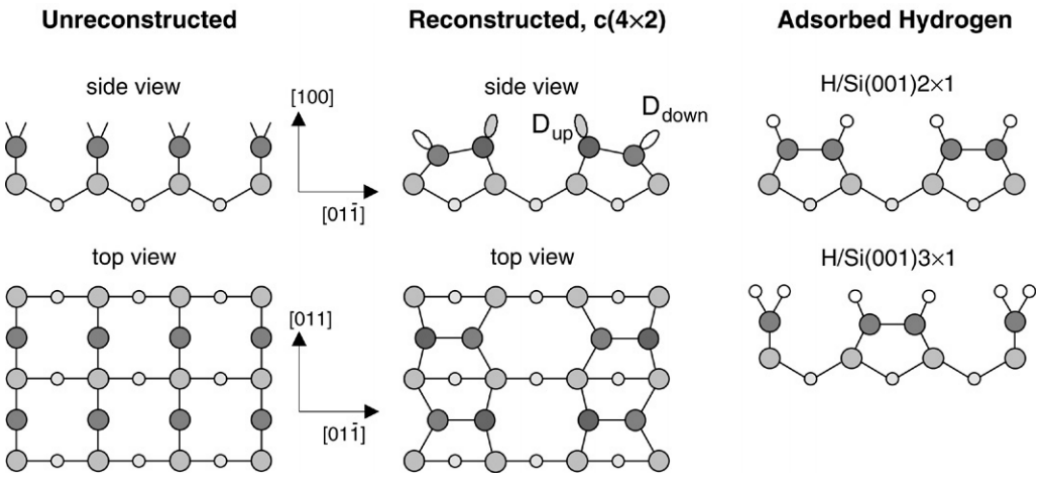

Figure 1.8: A cartoon showing how the silicon surface reconstructs into the 4x2 configuration where two neighbouring silicon atoms dimerize and then these dimers buckle in opposite directions with respect to their neighbors. The larger grey circles represent silicon atoms, the ellipses are their dangling bonds, and the small white circles are hydrogen atoms. Plot is taken from Dürr and Höfer [4].

1.4.3 Sticking Coefficients for H_2/Si(100)

The result of the dimerzation discussed in section 1.4.2 is that silicon is largely unreactive. This is a key fact for this study and cannot be overemphasized.

Figure 1.9 shows measurements of the sticking coefficient of H_2 off Si(100). As you can see, it is only as the surface temperature is increased that the coefficient begins to exceed Law's previously measured lower limit of 10^{-9}. All of our studies will be done with our silicon unregulated but in thermal contact with the laboratory, $\approx$ 300K.

As an interesting aside, the data in figure 1.9 are measured with a technique different from our own. By measuring the intensity of second harmonic generated light when a laser is reflected off the surface one can accurately measure the amount of hydrogen deposited on the surface. It must first be calibrated by exposing the surface to atomic hydrogen. The technique is eloquently explained in Dürr and Höfer [4]

1.5 Evidence for Rotational Interactions

In this section we will introduce three key pieces of evidence for interesting alignment phenomena. Here we look to motivate why scattering of aligned molecules are worthwhile to study. In brief terms, there is evidence that surfaces torque molecules even when they do not dissociate. Some systems' calculations show dissociation as a function of alignment.

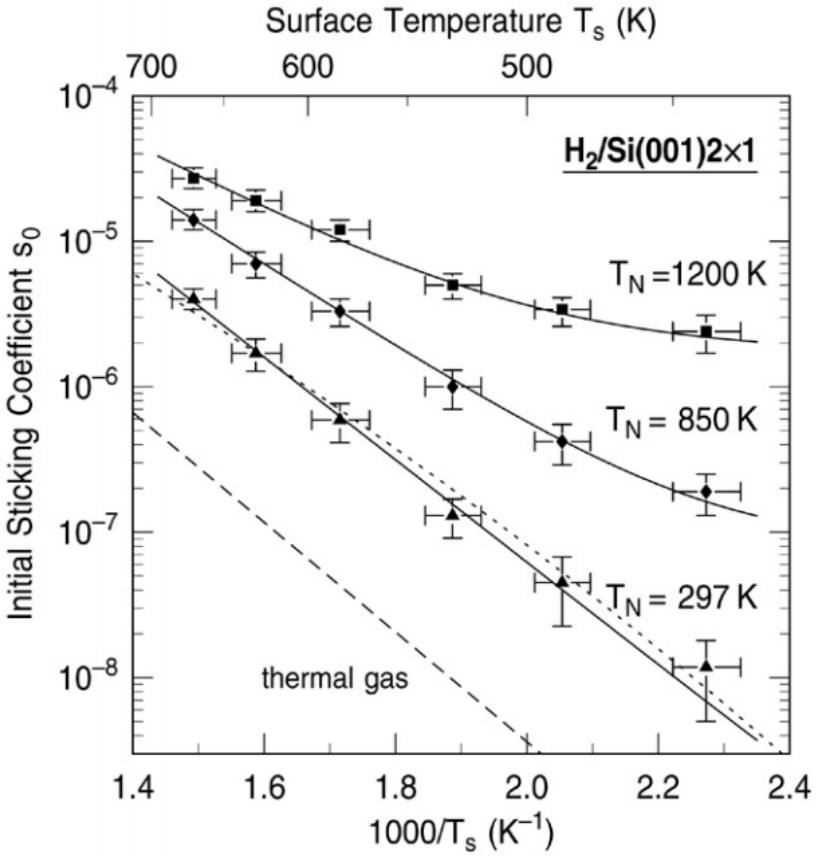

Figure 1.9: Experimental data showing the sticking probability of H_2 on Si(100) as a function of surface temperature for various nozzle (molecular) temperatures. Data originally published by Dürr in [5]. Plot is taken from Dürr and Höfer [4].

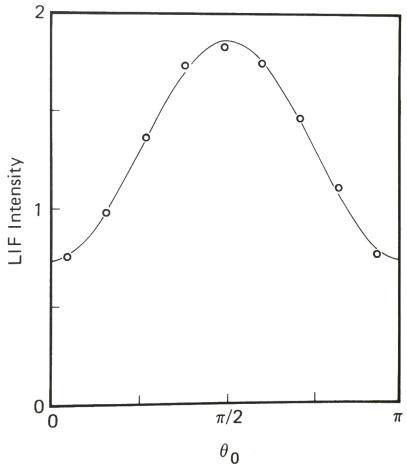

Figure 1.10: Experimental data showing the alignment of NO after inelastically scattered off Ag(111). This is preliminary evidence that an unaligned molecular beam can be torqued by a surface. Plot is taken from Scoles [6].

1.5.1 Rotational Alignment by a Surface

It has been previously observed that some surfaces inelastically scatter molecules into an aligned orientation [6]. Figure 1.10 shows how one can create an aligned sample of nitric oxide by scattering it off Ag(111). Quantization of alignments will be explained later in section 2.3. For now, it is clear significantly more molecules have an alignment of $\pi/2$ than 0 or π. We are still using the convention established earlier in section 1.1 so $\pi/2$ corresponds to molecules in a cartwheel configuration.

We must be careful here and note that NO is significantly more massive than H_2 and this will certainly influence the observed dynamics. No studies have been published that observe an alignment of H_2 after scattering from a surface. This is provided to demonstrate a surface can exert a torque on a

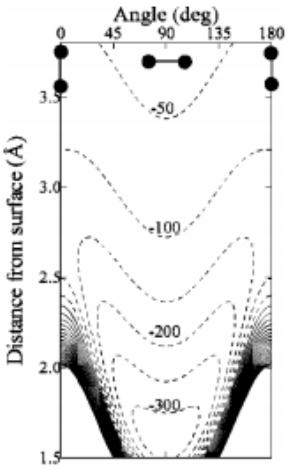

Figure 1.11: Results of calculations performed on H_2 scattered off Pd(111). This is presented to show the strong preference for the helicopter alignment to dissociate. From Crespos et al. [7].

molecule in the event of an inelastic scatter.

1.5.2 PES for H_2/Pd(111)

Calculations performed by Crespos et al. [7] demonstrate preferential desorption of H_2 in a helicopter configuration on palladium, see figure 1.11. Note that there is a deep well for the helicopter orientation. An attempt to demonstrate this phenomenon experimentally with the J=3 state was the subject of Isakson [2]. Palladium is a highly reactive surface and we cannot directly compare it to silicon. We provide this as evidence that indeed molecular orientation can play a large role when interacting with a surface.

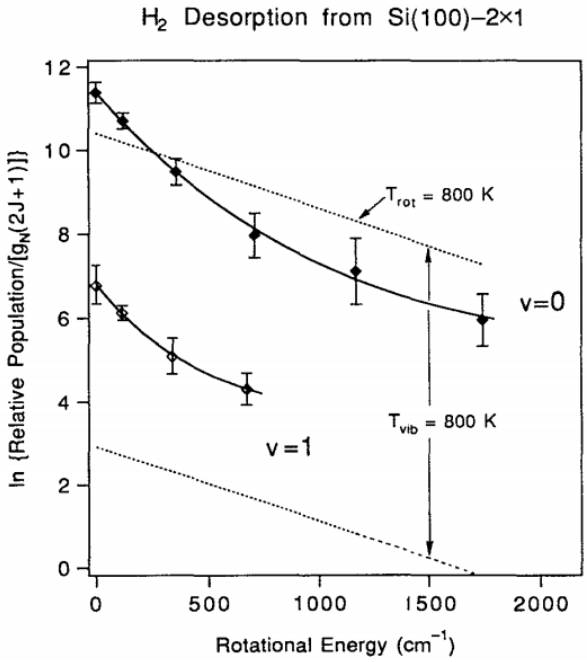

Figure 1.12: Experimental data showing frustration of higher rotational modes as hydrogen desorbs off silicon. From Shane et al. [8].

1.5.3 Rotational Frustration of Desorbing H_2 off Silicon

Our only evidence directly dealing with hydrogen and silicon in this section, experiments performed by Shane et al. [8] show a suppression of higher rotational modes, a so called frustration, for hydrogen desorbing from silicon. This frustration is seen as the distribution of angular momentum states departs from Boltzmann statistics determined by surface temperature. Figure 1.12 is from their paper.

This is the strongest evidence we have that something interesting is happening at the surface. There are some dynamics at play that heavily

influence the molecule's rotational state and its alignment. Note that there are currently no studies that look at an initially aligned sample. We know that a surface can polarize an unpolarized sample but what will happen to a sample that is already polarized?

1.6 Moving Forward

We wish to study how an interaction with a surface, but not a dissociative one, would affect the alignment of molecules. This is important for future studies that will look at alignment effects on desorption. These future studies will look for alignment effects using the same King and Wells method. It will be necessary to know if the alignment is destroyed or maintained after rebounding from the surface. These studies will be much more difficult if the alignment is destroyed. If the alignment is maintained the measurement will only need to be done at the incoming angle of alignment. This thesis will answer that question.

Chapter 2

Relevant Nonlinear Optics & Lasers

In this chapter we will first outline the relevant physics to laser operation then discuss the nonlinear optical effects we utilize in this experiment. The section on laser physics is largely an overview and should be considered a refresher for a physicist having already taken a course on lasers. However, the overview of nonlinear phenomena is necessary to understand how the measurements described in chapter 4 are feasible.

2.1 Laser Physics

For this experiment there are two lasers: the pump laser (section 3.3.1) and the probe laser (section 3.3.2). The pump prepares the molecules' quantum mechanical state, e.g. vibrational level or angular momentum and projection. The probe can selectively ionize molecular states and orientations. It is necessary to provide some details to their theory of operation so that we can describe how these two vital functions work. Both of these lasers begin as Nd:YAGs (Neodymium-doped Yttrium Aluminium Garnet) before we use several nonlinear processes to convert the wavelength.

2.1.1 Laser Theory of Operation

The following overview draws from the lecture notes of Professor Michael Downer [24] and Siegman's text [9].

For a light source to qualify as a laser beam the light must have a well defined wavelength or wavelengths, typically **monochromatic** in the case of the former, and it must be **synchronous** i.e. mode-locked or phased. To satisfy both requirements the key is to establish **population inversion** within a material. Thus our material must have a *single* excited state that has a *long lifetime*. The well defined excited state will satisfy the monochromatic requirement and the long lifetime will allow us to use **stimulated emission** resulting in a phased pulse.

We'll start by discussing a generalized state diagram of some lasing material. Figure 2.1 is the idealized four-state system of which Nd:YAG is an example. It is important that aside from our transition of interest, the other transitions are quick and radiation-less so that we can "pile atoms up" into the excited state. Once we have more atoms in the excited state than the ground state we have population inversion. By getting as many atoms as possible into this excited state we will have a more active stimulated emission process which will result in more intensity in our resulting laser beam.

Let us take a moment to explain stimulated emission [9]. Consider an atom that is in the long-lived excited state in figure 2.1. When this atom spontaneously relaxes it will emit a photon of energy E. If another photon,

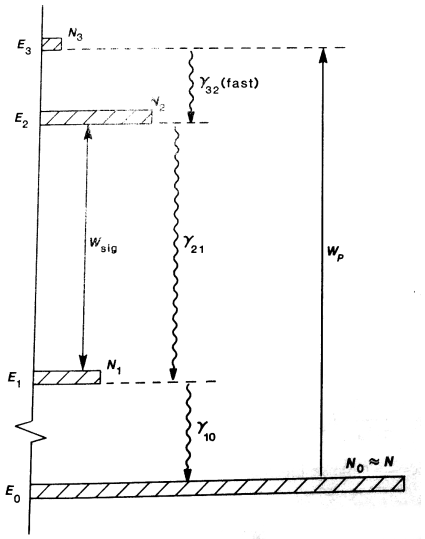

Figure 2.1: An idealized schematic of a 4-level laser system. The lasing transition will be from E_2 to E_1 and be of energy γ_{21}. From [9].

also of energy E, travels in the vicinity of the excited atom, the atom will be perturbed causing it to de-excite and releasing its own photon. We are left now with two photons of energy E. This process is depicted in figure 2.2.

As figure 2.1 implies, we drive the atoms up to the highest energy level by **pumping** the material, depicted as the W_P transition. This pumping for our Nd:YAGs is done with flash-lamps. Our flash-lamps are xenon discharge tubes that are set to breakdown with a high voltage repetitively. The flash-lamps are left in a minimal conducting state known as "simmering" and then pulsed, or "flashed", with a high voltage pulse. This will cause the lamp to emit a burst of bright white light. A small fraction of this light will be absorbed by the atoms and they will be excited into the high energy state. The light that is not adsorbed will be waste heat delivered to the YAG rod

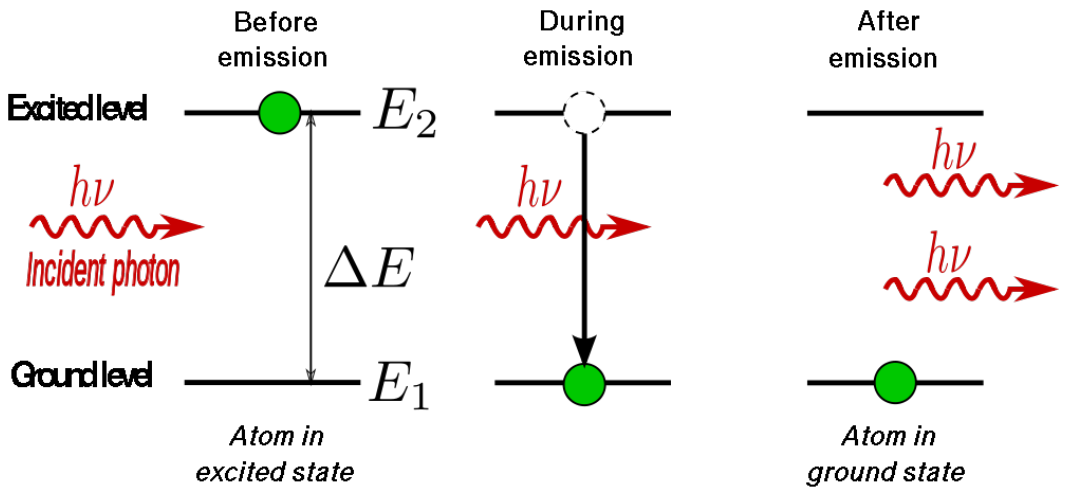

Figure 2.2: A depiction of stimulated emission. From [10].

and cladding/housing to be carried away by the cooling water.

This will all be all for naught if we do not have the lasing material inside a highly tuned **cavity**. Diagram 2.3 is a cartoon depicting a laser cavity. The cavity will collect any light that is on or near the propagation axis. First *spontaneous* emission will be collected by the cavity. As this light builds up, *stimulated* emission will begin to take over and will drive principle transitions downward collecting more photons. This is why population inversion is important: you can only get photons from atoms already in the excited state and if you have atoms build up in E_1 it can start re-adsorbing photons. With more and more passes the amount of light inside the cavity will begin to plateau. At this point we will open the cavity on one end thereby changing its quality or "Q" factor. This is known as **Q-Switching**. In our lasers a typical delay

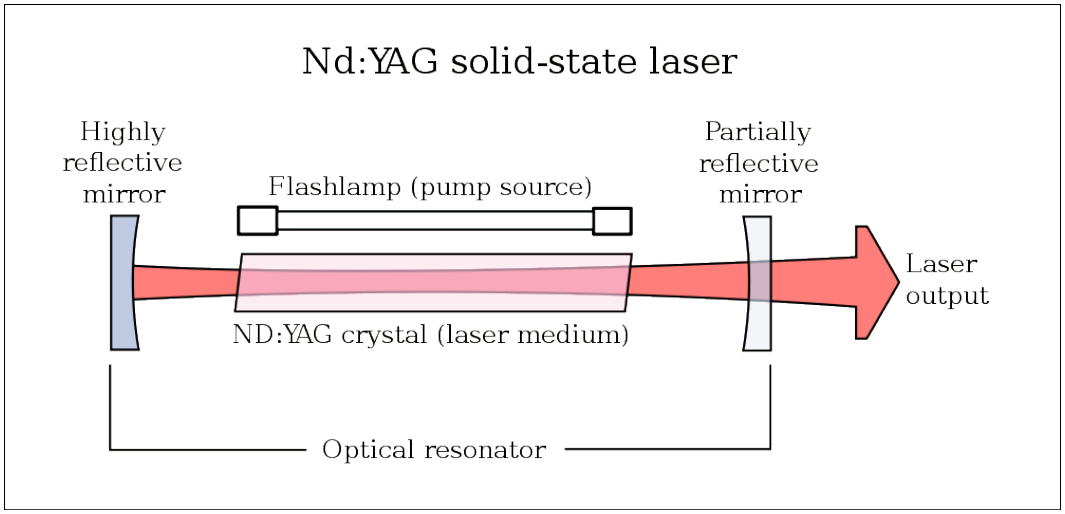

Figure 2.3: A diagram of an Nd:YAG laser cavity. A key difference between the depiction and our cavity is that instead of a partially reflective mirror we have a Q-Switch in the form of a Pockel's cell. The sketch depicts a continuous-wave (CW) laser. From [11].

between when the flash-lamps are fired and the Q is switched is $230\mu s$; this will be different for each laser and must be tuned for maximal power.

After the laser cavity there is an amplification step which operates on the same principles we have already discussed but in a single pass fashion. Laser amplification is a rich field unto itself. Siegman, the primary reference has 2 chapters on the matter. For brevity's sake we will eschew this and leave it as fact that after the oscillator cavity the beam is amplified before exiting. The beam passes through another piece of lasing material that has its population inverted but does not have a laser cavity around it.

For an Nd:YAG laser, such as the two in use in this experiment, the principle lasing wavelength is $1064nm$ with a pulse width of approximately $5ns$

and have a repetition rate of $10Hz$. This wavelength is immediately frequency doubled by a KDP crystal, see section 2.2.1, to $532nm$. Our pump laser is operated at a power of $\approx .420W$ and our probe laser begins as $3.1W$ before its various conversion processes, see section 3.3.2.

2.1.2 Dye Laser Theory

Using many of the laser concepts outlined in the laser theory of operation section, 2.1.1, we will explain the underlying principles of a dye laser. A dye laser is necessary to make a tunable source of laser radiation with a narrow line width and short pulse duration. In recent years, Titanium Sapphire (TiSaph) lasers have come to fill this role but would not work for this experiment because the line width is too broad. In this experiment we have one dye laser for the probe beam. This is essential to our experiment because the ionizing transitions we need to measure are at precise wavelengths between 200 and 202nm.

A schematic of our dye laser, a Quanta-Ray PDL-3, is shown in figure 2.4. The pumping source that is exciting the dye molecules is the frequency-doubled output of a Nd:YAG. The pump light is first split so that a small fraction of the pumping light is sent to the oscillator cuvette (lower-left) while the rest is sent to the amplifier cuvette (middle-right). This excites atoms in the dye molecules in both cuvettes into a dense *continuum of excited states*. What this allows is for laser radiation on any of these wavelengths by tuning the path length in the oscillator. To achieve this, the dye laser has an angle

tuned grating inside the black box on the lower-left; it is not accessible and doing so should never be attempted as it will destroy the calibration with the dial value. Only this wavelength will be amplified as the beam passes through the amplifier cuvette.

There is no Q-switching in a dye laser and every pulse is generated on a single-shot basis, much like the amplifier in the Nd:YAG laser. All stages are mechanically aligned to produce the most intense light.

In this experiment we use Rhodamine-640 dye which peaks at approximately 602nm and is tunable over a range of approximately 2nm. Figure 2.5 shows the tunability of Rhodamine 640 [12]. For $3.1W$ of incident power the dye laser can achieve approximately $.50W$ of output power dependent on the wavelength, concentration of the dye, age of the dye, and the relative in-tune state of the optics.

2.2 Nonlinear Optical Processes

In this section we will discuss the various nonlinear processes at work in this experiment. While one could make a very strong case that the section on lasers should also be classified as such this has not been the case historically. Some background knowledge will be assumed and everything will be presented in a classical model (i.e. Drude model). This discussion largely draws from R. Boyd [13].

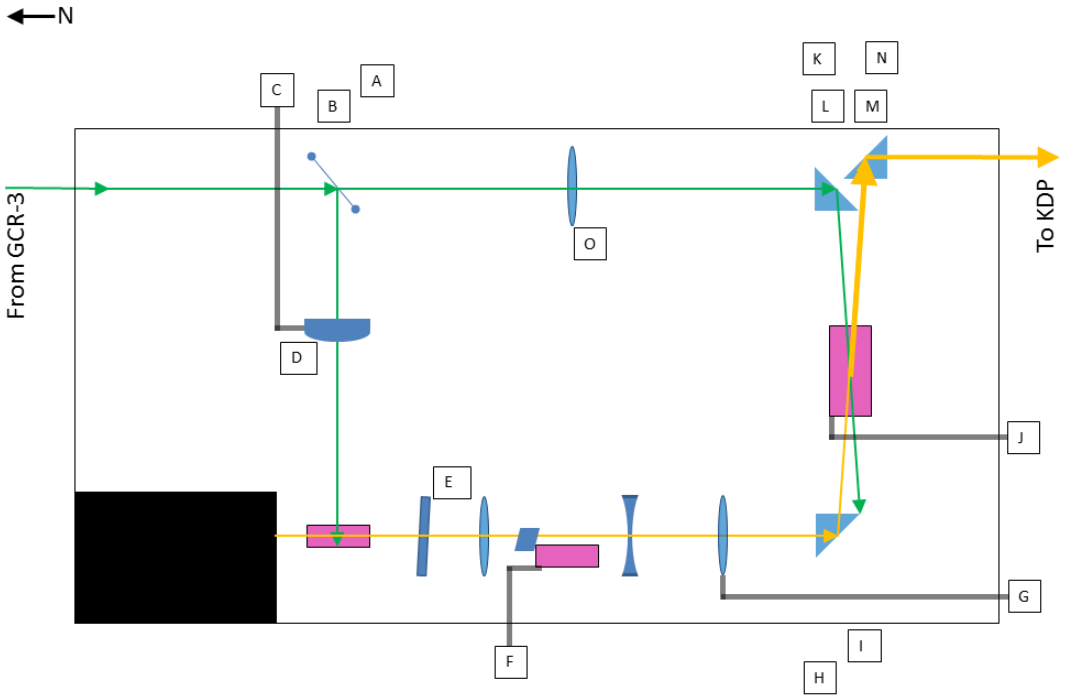

Figure 2.4: A diagram showing the PDL-3 of the author's own making. A: Horizontal Angle of Splitter; B: Vertical Angle of Splitter; C: Translation of Cylindrical Lens; D: Roll of Cylindrical Lens; E: Rotation of Mirror 1; F: Translation of Preamplifier; G: Translation of Divider 1; H: Horizontal Angle of Prism 1; I: Vertical Angle of Prism 1; J: Translation of Amplifier.

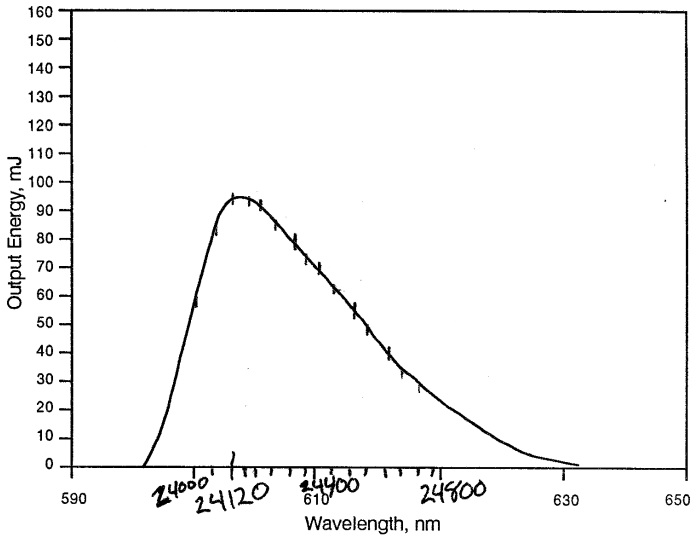

Figure 2.5: A sketch showing the tunability of Rhodamine640. The hand-drawn values correspond to the laser's dial value (4×wavelength). From [12].

2.2.1 Harmonic Generation

At first glance, harmonic generation can be thought of as the *addition of two photons to form one photon of equal energy.* This is not scientifically accurate but it gives the reader a sense of what the phenomenon is that we wish to describe and understand. We must first set the stage by discussing the phenomenon of **nonlinear susceptibility**.

As known from electromagnetism, all materials have an **electric susceptibility** (χ) which determines how charge within the material will redistribute in the presence of an electric field. This allows one to discuss the induced polarization of a material when subjected to an electric field of varying strength [25], e.g. how a dielectric functions inside a capacitor. This is

known as the 0th order χ where the reaction is only a property of the material. The first complication is that if we allow the electric field to oscillate at a frequency ω, the susceptibility can be a function of this frequency: $\chi(\omega)$. This allows us to discuss how light interacts with various materials and explain such phenomena as the blueness of the sky or dispersion by a prism. The next layer of complication is that the material can have some *orientation dependence*: $\chi(\omega, \mathbf{x})$. This means that light will react differently when passing through the top of a certain crystal than when passing through the side. Two examples of particular importance here are potassium di-phosphate (KDP) or beta-barium borate (BBO). The last complication, thankfully, is that some materials, KDP and BBO included, react differently based on the polarization of the incident light: $\chi(\omega, \mathbf{x}, \mathbf{P})$ [13].

One can take this information and, following the thorough discussion in Boyd's chapter 2.1 [13], make a wave equation out of Maxwell's equations that relates the generated wave to a driving term proportional to the nonlinear polarization:

$$\nabla^2 \mathbf{E}_n(\mathbf{r}) + \frac{\omega_n^2}{c^2}\epsilon^{(1)}(\omega_n) \cdot \mathbf{E}_n(\mathbf{r}) = -\frac{\omega_n^2}{\epsilon_0 c^2}\mathbf{P}_n^{NL}(\mathbf{r}) \tag{2.1}$$

where we can write, for example, the third index of $\mathbf{P_n^{NL}}$ as it is simply related to the nonlinear susceptibility from above:

$$P_3 = 2\epsilon_0 \chi^{(2)} E_1 E_2 \tag{2.2}$$

This third index refers to the wavelength generated by the crystal through "summing" the first and second.

This level of mathematical rigour is not desired here; we are seeking a phenomenological discussion. To point: the induced dipole moments of each unit cell in our crystal will have not only a component at the driving frequencies but also at the sum of those frequencies, analogous to the beat frequency phenomenon. It is the nonlinear susceptibility of these unit cells that gives rise to this behaviour. If we can align the unit cells inside the crystal then these radiating dipoles will be phased and the generated light will be coherent. Thus we wish to **phase match** the crystal by **angle tuning** its position such that each radiating dipole is in phase and the generated light constructively interferes. Figure 2.6 depicts this concept.

Second harmonic generation is a special case of the above discussion where the two input frequencies are equal and phased, i.e. the same laser source. Third harmonic generation is a more general case where the two input frequencies are first and second harmonics of the same source. In our experiment KDP serves the role of the second harmonic generator that gives us photons at ω and 2ω. BBO then takes these frequencies and produces photons at 3ω.

2.2.2 Stimulated Raman Scattering

For those unfamiliar, the Raman effect is an inelastic scattering of photons off of a molecule [26]. The light can either be red-shifted termed 'Stokes'

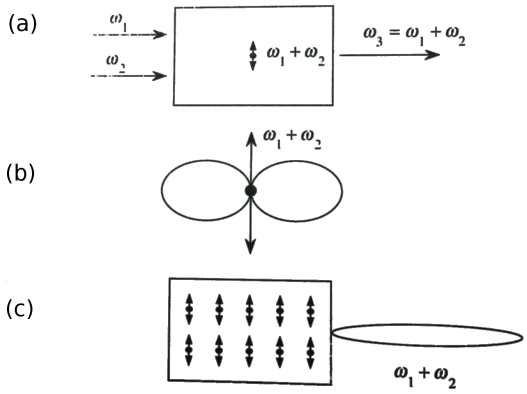

Figure 2.6: A cartoon depicting key elements from our explanation of harmonic generation inside a crystal. Part (a) establishes the phenomenon: two photons at ω go in and 1 photon at 2ω comes out. Part (b) shows that an active unit cell of the crystal functions like an antenna that radiates at 2ω. Part (c) shows how these individual antennae can coexist and simultaneously radiate from within the crystal. From [13].

or blue-shifted termed 'anti-Stokes'. The energy shift of the light will be precisely determined by the molecule's excitation. When this happens for a single photon it is the **spontaneous Raman effect** and occurs roughly with a 10^{-7} probability. The probability, or cross section, does have various depenencies but the spontaneous Raman effect is *not resonant*. We can see the same phenomenon with a much higher probability if we use a collimated, coherent light source (i.e. a laser) and focus it upon the molecules we wish to scatter off. This is how we will induce the **Stimulated Raman Effect**.

A full quantum description of this process is complicated in its rigour. Thus we will utilize the formalism established in section 2.2.1 where we seek to write a nonlinear susceptibility for this process:

$$\chi_R(\omega_S) = \frac{\epsilon_0 * \frac{N}{6m} * (\frac{\partial\alpha}{\partial q})_0^2}{\omega_J^2 - (\omega_L - \omega_S)^2 + 2i(\omega_L - \omega_S)\gamma} \tag{2.3}$$

where N is the cross section, $\frac{\partial\alpha}{\partial q}$ is the polarisability of the molecule, ω_S is the frequency of the Stokes-shifted light, ω_L is the frequency of the principle light, and ω_J is the difference in these frequencies which is also the frequency of light associated in the energy of the transition in the molecule. Modified notation from Boyd [13].

The key part of this susceptibility is that it is resonant based on the *difference* of the two driving frequencies. Once a spontaneous Raman scattering event occurs for a particular transition, the wavelength shift for this transition will "snowball" until it is the only shift we see. It is this phenomenon that we utilize to rotationally pump the molecules inside the molecular beam, see section 3.3.1.

2.2.2.1 Creation of Molecular Alignments

*An **alignment** is an anisotropic distribution of the absolute value of angular momentum projection numbers.* In the literature this is distinguished from an **orientation** which considers the helicity of the rotation, that is to say the *signs* of the projection number; our measurement technique, section 2.2.3, is insensitive to orientation and thus will not be considered.

The stimulated Raman transitions of the molecules are driven by dipole interactions. This means that the transitions will follow the selection rules $\Delta J = \pm 1$ and $\Delta m_J = 0$ (for each adsorbed photon) [27] *as long as the light*

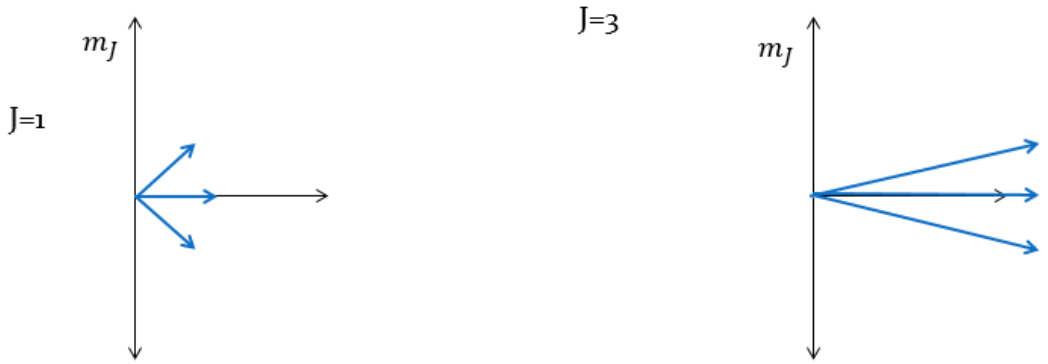

Figure 2.7: A depiction of how the angular momentum quantum numbers are changed during a pumping transition.

is ***linearly*** *polarized*. Specifically for hydrogen the $\Delta J = \pm 1$ transition is forbidden, as an anti-symmetry rule enforcement on the wavefunction, and hydrogen will undergo two of these transitions in rapid succession, as limited by the Fermi exclusion principle, resulting in these rules: $\Delta J = \pm 2$ and $\Delta m_J = 0$. The lack of changing the angular momentum projection quantum number allows us to make an **aligned molecular sample**. This is pivotal to this dissertation and cannot be emphasized strongly enough. Figure 2.7 illustrates what happens to the J and m_J quantum numbers during one of these transitions. The axis of rotation is defined by the polarization direction of the light [28].

For a detailed explanation of how we measure and quantify such alignments see section 2.3.

2.2.3 Resonantly Enhanced Multiphoton Ionization (REMPI)

In this section we will describe how we can measure the alignment of a molecular sample. We must be able to preferentially (not exclusively) ionize hydrogen that is in a particular J state with a particular m_J projection.

Let us consider the problem of ionizing hydrogen. The first electron is bound very tightly at 13.6eV. To directly ionize this, one would need an x-ray laser which is far from trivial. Instead of trying to use 1 photon to do the job of ionizing, we will use multiple. Each photon does not have sufficient energy to excite an electron. Two photons *combined* are on resonance to bring one of the electrons into an excited state. A third photon then has plenty of energy to completely liberate that electron. This is the 2+1 scheme of **Resonantly Enhanced MultiPhoton Ionization (REMPI)** that we employ [15] [28].

In the resonant transition, the first photon is absorbed and the molecule is excited to a **virtual state**. A virtual state is, as the name implies, not an observable state of the molecule. They are short-lived excitations, limited by the Fermi energy-time uncertainty principle, that if left alone will quickly de-excite and leave no trace of ever happening. If the second photon is adsorbed by the molecule within the time limit set by this uncertainty principle, then the molecule will transition to a real excited state [29].

Let us first establish an important piece of spectroscopic notation: **Q-branch** and **S-branch**. The branches refer to different transitions the observed molecule undergoes while the light of the observation interacts with it.

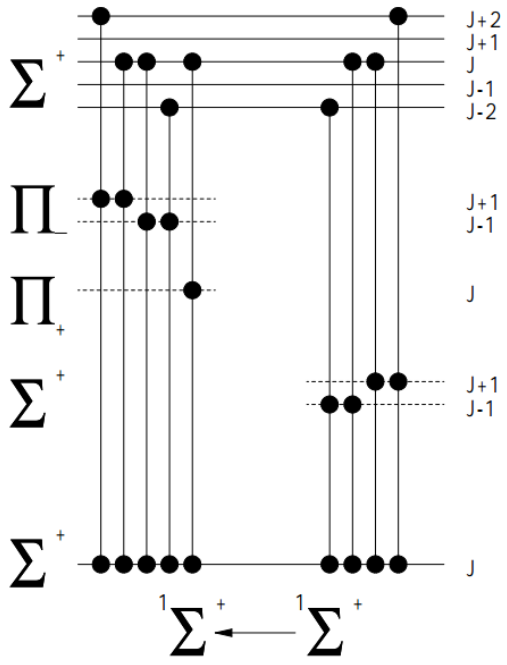

Figure 2.8: A state diagram illustrating the different virtual intermediate states and their real final states in a two photon absorption of a diatomic molecule. This is valid for all diatoms. For an explanation of molecular state notation see chapter 1 of Steinfeld [14]. From Isakson [2].

In this context, the different branches refer to different changes in the angular momentum quantum number. Q is defined as no change and the surrounding letters are assigned for integer change such that R is $J \rightarrow J+1$ and S is $J \rightarrow J+2$, see table 2.1.

Table 2.1: illustrating the letter codes for spectroscopic branch notation.

letter code	O	P	Q	R	S
change in J	-2	-1	0	+1	+2

Looking at figure 2.8, you can count how many different pathways exist between the ground and excited state for the $J \rightarrow J$ or Q-branch mode (5) and how many exist for the $J \rightarrow J+2$ or S-branch mode (2). It is important to note that both branches have at least a Σ and a Π character virtual state. These two branches are different excited state energies for H_2 and are thus observed at different wavelengths.

The state selectivity feature of this technique is described in full rigour by Hanisco [15] and Kummel et al. [30] [31] in particular with rotational alignment measurements of N_2. The formalism applies to H_2 as well. To summarize these rigorous explanations, recall the dipole interaction Hamiltonian has a spatial overlap term. Hanisco defines **path ratios** in terms of these radial spatial overlaps from the two simultaneous dipole transitions:

$$\begin{aligned} \mu_i^2 &= |R_{ei}^0 R_{fe}^0 - 2R_{ei}^{+1} R_{fe}^{-1}|^2 \\ \mu_s^2 &= |2R_{ei}^0 R_{fe}^0 + 2R_{ei}^{+1} R_{fe}^{-1}|^2 \end{aligned} \tag{2.4}$$

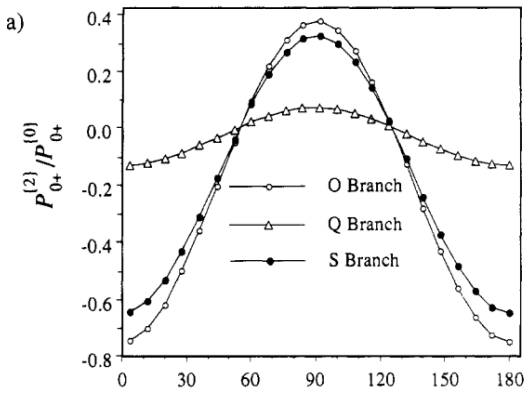

Figure 2.9: The results of calculations on the sensitivity of the Q- and S-branches in determining a diatomic molecule's alignment as performed for N_2 initially in the $J = 20$ state. The variation is qualitatively similar for H_2. From Hansico [15].

The line strength of the Q-branch depends on both μ_i^2 and μ_s^2 while the S-branch depends solely on μ_s^2. This is too many variables in the case of the Q-branch and results in not being able to use it to determine the molecular alignment. Said another way, the Q-branch can only measure alignment if the sigma or pi character of the virtual state is known; H_2 has both, and multiple at that, thus it cannot be used.

2.3 Quantifying Molecular Alignments

In this section we will outline the quantification of molecular alignments. This is pivotal to our analysis in chapter 4. We will start from the most general ideas of distributions and their moments, apply this to angular momentum projection distributions, and then provide theoretical values for the maxima of the moments in order to give a sense of scale to our later

analysis.

2.3.1 Probability Distributions and Moments

As with any distribution, the obvious things to talk about will be the mean, mode, spread, skewness, etc.. All these separate definitions are unified under the concept of **moments of the distribution**. The n^{th} moment of a distribution ($\langle x^n \rangle$) describes some aspect of the shape of the distribution. This is completely analogous to the situation in classical mechanics when dealing with distributed masses. In the classical mechanics case, we know the relevant calculations will be things like the total mass, the center of mass, and the moments of inertia (a big clue there is that "moments" was used!). Mathematically we define the moments as order parameters thusly:

$$\langle x^n \rangle = \int_{-\infty}^{+\infty} (x - c)^n P(x) dx \tag{2.5}$$

where $\langle x^n \rangle$ is the n^{th} moment of the distribution, c is the mean of the distribution (in our following case 0), and $P(x)$ is the probability distribution.

Now, under the unified theory of moments, we can simply express the various terms of a distribution that were originally treated separately as shown in table 2.2.

2.3.2 Moments of Alignment: $\mathbf{A_0^{(2)}}$&$\mathbf{A_0^{(4)}}$

It should be little surprise to the reader that we will need to concern ourselves with discrete distributions: angular momenta of atoms and molecules

Table 2.2: Moments of distributions for centralized distributions, i.e. $c = 0$.

Order (n)	Integral Form	Meaning	Notes
0	$\int_{-\infty}^{+\infty} x^0 P(x)dx$	total probability	the area (nom. 1)
1	$\int_{-\infty}^{+\infty} x^1 P(x)dx$	mean	the center, μ
2	$\int_{-\infty}^{+\infty} x^2 P(x)dx$	variance	standard deviation^2
3	$\int_{-\infty}^{+\infty} x^3 P(x)dx$	skewness	asymmetry
4	$\int_{-\infty}^{+\infty} x^4 P(x)dx$	kurtosis	peakedness

are quantized both in magnitude and direction. Let's take our moment formalism from section 2.3.1 and discretize that. Equation 2.5 will transform into a discrete sum, equation 2.6.

$$\langle x^n \rangle = \sum_{i}^{N} x_i^n P(x_i) \tag{2.6}$$

In order to apply this to angular momenta distributions we can make a further observation. There is nothing special about using increasing orders of x other than these give the statistically relevant moments ('shape') of distributions. When discussing angular momentum states of the hydrogen atom it is more relevant to express the wavefunction in terms of **Legendre polynomials**, $(P_m^l(\cos(\theta)))$. There are many reasons the Legendre polynomials are useful in general but we will leave that discussion to Griffiths [27]. For our current purposes, we need a symmetric function that will quantify the possible excess of m_J values near the equator ($m_J = -1, 0, +1$; $\theta \approx 90°$). As a reminder, the Legendre polynomials are the 2D version of the 3D spherical harmonics. We have and will be dealing solely with θ and are insensitive to

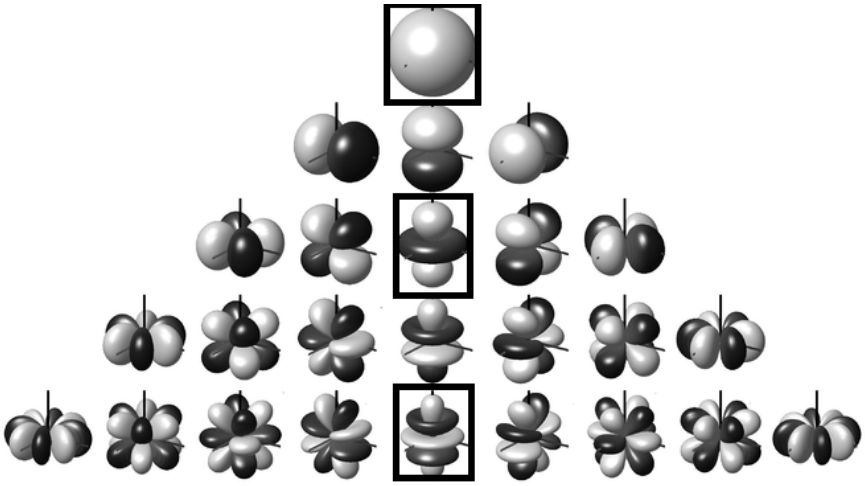

Figure 2.10: A table showing the first six families of spherical harmonics. Of particular use here are the Y_0^0, top, and Y_0^2, second row, middle. These are boxed for convenience. Original work published to WikiMedia [16].

ϕ. However, the spherical harmonics will still give us a sense of which Legendre terms we could anticipate to provide meaningful characterization of an alignment. Looking at the table of spherical harmonics, figure 2.10, we see that Y_0^2 and Y_0^4 (boxed) have the highest equatorial probability. We will need to find 'how much' our distribution is equatorial versus purely spherical so we will be comparing ratios of coefficients of the $P_0^2(\cos(\theta))$ and $P_0^4(\cos(\theta))$ to $P_0^0(\cos(\theta))$, which in the KSZ formalism is set equal to 1. It is these ratios that are often referred to as the quadrupole moment ($A_0^{(2)}$) and the hexadecapole moment ($A_0^{(4)}$) [32], equation 2.7. An attempt was made to observe a non-zero hexadecapole moment, see section 4.4.4, and was unsuccessful. Thus it will be omitted moving forward.

$$A_0^{(2)} = \langle P_0^2(\cos(\theta))\rangle = \sum_{i=1}^{N} n(\theta_i) P_0^2(\cos\theta_i)$$
$$A_0^{(4)} = \langle P_0^4(\cos(\theta))\rangle = \sum_{i=1}^{N} n(\theta_i) P_0^4(\cos\theta_i) \tag{2.7}$$

As a reminder, the algebraic forms of $P_0^2(\cos\theta)$ and $P_0^4(\cos(\theta))$ are given in equation 2.8.

$$P_0^2(\cos(\theta)) = \frac{1}{2}(3\cos^2\theta - 1)$$
$$P_0^4(\cos(\theta)) = \frac{1}{8}(35\cos^4\theta - 30\cos^2\theta + 3) \tag{2.8}$$

It is immediately obvious that to utilize equations 2.7 and 2.8 we will need to express the available m_J values in terms of θ, the angle between J and the quantization axis. Remember that, in units of $\hbar$, J and m_J are restricted to integer values. The definition of $\cos\theta$ in terms of the angular momentum quanta is equation 2.9. The allowed angles for the first 4 J levels have been calculated for convenience and are displayed in table 2.3.

$$\cos\theta = \frac{m_J}{\sqrt{J(J+1)}} \tag{2.9}$$

where θ is the angle between J and the special z-axis of quantization.

Alternatively, $P_0^2(\cos\theta)$ and $P_0^4(\cos\theta)$ can be expressed in terms of m_J and J by utilizing equation 2.9. These are equations 2.10 and 2.11. This is another common expression that one finds in the literature, notably ref. [32].

Table 2.3: Angles between J and m_J for the first 4 levels.

	m_J						
	-3	-2	-1	0	$+1$	$+2$	$+3$
$J=3$	150°	125.3°	106.8°	90°	73.22°	54.74°	30°
$J=2$	n/a	144.7°	114.1°	90°	65.91°	35.26°	n/a
$J=1$	n/a		135°	90°	45°	n/a	
$J=0$	n/a			90°	n/a		

$$\begin{aligned} P_0^2(\cos\theta) &= \frac{1}{2}\left(3\left(\frac{m_J}{\sqrt{J(J+1)}}\right)^2 - 1\right) \\ &= \frac{1}{2}\left(3\left(\frac{m_J^2}{(J(J+1))}\right) - 1\right) \\ &= \frac{1}{2}\left(\left(\frac{3m_J^2 - J(J+1)}{J(J+1)}\right)\right) \\ A_0^{(2)} = \langle P_0^2 \rangle &= \left\langle J_i \left| \frac{3J_z^2 - J^2}{J^2} \right| J_i \right\rangle \end{aligned} \tag{2.10}$$

$$A_0^{(4)} = \langle P_0^4 \rangle = \left\langle J_i \left| \frac{35J_z^4 - 30J_z^2J^2 + 3J^4 + 25J_z^2 - 6J^2}{8J^4} \right| J_i \right\rangle \tag{2.11}$$

2.3.3 The Idealized Pumping Alignment Case

We need to first establish what m_J populations we expect first in the unpumped molecular beam then what a pumping event should do to those populations. One would naively think that before a pump event the molecules should be perfectly uniformly distributed since there isn't even a well defined quantization axis yet. However, during the supersonic expansion the inter-molecular cross-section will be higher for molecules that happen to be

in a helicopter configuration than a cartwheeler. This would result in a net cartwheeler alignment near the surface. This has been observed predominantly in seeded O_2 beams by Aquilanti et al. [33]. It has not been observed experimentally here so we will treat the initial distributions as uniform.

Now for the pumping. We will assume that our pumping process is perfectly linear, such that $\Delta m = 0$ holds, and that our molecular beam has rotationally cooled to approximately 200K. We will further assert that our pumping process equilibrates the populations between the two transitioning levels: e.g. if .7 of the entire molecular beam population is in $J = 1$ (.233 per m_J) and .05 is in $J = 3$ (.007 per m_J), the population in m_J states ± 1 and 0 of $J = 1$ and $J = 3$ will be equalized to .120 each while the $m_J = \pm 2$ and ± 3 of $J = 3$ will remain untouched. If we remove the unpumped molecules from this distribution so that we only concern ourselves with the central m_J values, the relative populations among a given J value will be much more simply expressed, i.e. $\frac{1}{3}$ for the central states and 0 for the wings. **This asserts an important analysis step that must be employed later in chapter 4: we must measure the unpumped molecules in each configuration and subtract this out of our pumped data!** Figure 2.11 demonstrates the acceptable approximate values used for the above J states.

A quick aside: from this model of pumping behavior we can also make an estimate of the pumped to unpumped ratio for the $J = 3$ and $J = 2$ cases. Using the above relative populations for $J = 3$ and $J = 1$ we could expect to see half the $J = 1$ population ($\frac{.7}{2} = .35$) move up to $J = 3$ making the total

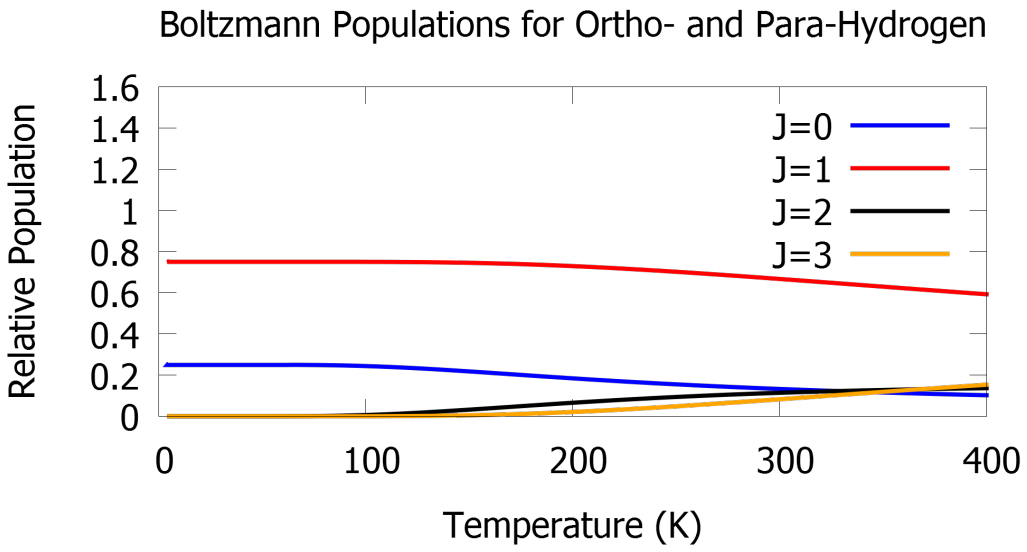

Figure 2.11: Boltzmann statistics for the rotational states of H_2 with even-to-odd state transitions forbidden. This arises from a restriction on the nuclear spin wavefunction and H_2 obeying Fermi spin statistics.

population, across all m_J states, increase from .05 to .4 or a 8-fold increase in the $J = 3$ population for measurements relatively insensitive to alignment, i.e. the Q-branch. If we use a transition that is sensitive to m_J values this ratio will further increase but linestrength factors and relative polarizations of the two lasers would then be a factor. For $J = 0$ and $J = 2$ the initial populations are .2 and .05, respectively. Pumping would then give an increase from .05 to .15 for a 3-fold increase.

We can express $A_0^{(2)}$ as a sum over the individual m_J values so that we can easily compute a range for $A_0^{(2)}$ values, equation 2.12. The same can be done for $A_0^{(4)}$, equation 2.13.

$$A_0^{(2)} = \sum_{m_J=-J}^{+J} n(m_J) \frac{3m_J^2 - J(J+1)}{J(J+1)} \tag{2.12}$$

$$A_0^{(4)} = \sum_{m_J=-J}^{+J} n(m_J) \frac{35m_J^4 - 30m_J^2 J(J+1) + 3(J(J+1))^2 + 25m_J^2 - 6J(J+1)}{8(J(J+1))^2} \tag{2.13}$$

Following our discussion above, we will background subtract our simulated populations such that m_J levels we do not interact with are treated to have zero population. Furthermore, we renormalize our populations in a given J state since we are unable to make measurements at multiple J levels simultaneously. The resulting $n(m_J)$ for the $J = 3$ case is simply $\frac{1}{3}$ for $m_J = \pm 1$ and 0 and 0 for the others. $J = 2$ is even easier since there is only 1 m_J value we populate: $m_J = 0$.

Using equations 2.12 and 2.13 with our given maximum $n(m_J)$ values we build table 2.4. We calculate the minimum, or entirely unaligned sample, by asserting a uniform, normalized population among the m_J values. This is $\frac{1}{7}$ for $J = 3$ and $\frac{1}{5}$ for $J = 2$. In both cases the arithmetic is trivial and evaluates to 0 for both $A_0^{(2)}$ and $A_0^{(4)}$.

Table 2.4: Minimum $A_0^{(2)}$ and $A_0^{(4)}$ values corresponding to perfect alignment.

	$A_0^{(2)}$	$A_0^{(4)}$
$J = 3$	$-0.83\bar{3}$	$+0.13\bar{8}$
$J = 2$	-1.000	$+0.250$

Now that we have bounds on $A_0^{(2)}$ and $A_0^{(4)}$ we can employ these during our fitting procedure in chapter 4. It is important that we understand any fitted values outside these bounds are deemed unphysical.

2.3.4 Relating this to Ion Observations

The following is a severely abridged version of the excellent paper by Kummel et al. [30]. For more details than are reported here, I refer you there.

The last complication we must consider is that our measurement process is not ideal. That is to say, the REMPI process that is sensitive to the alignment of molecules does not produce 0 ions for angles not equal to any of those listed in table 2.3 and our data will not simply be histograms like those we've seen thus far. Our real ion signal will be modulated with probe polarization angle as in equation 2.14.

$$
\begin{aligned}
I(\theta) &= C_d \times \sum_{kq} \mathcal{P}_q^k(J_i, \Lambda_i, J_f, \Lambda_f; \Omega) \times A_q^{(k)}(J_i) n(J_i) \\
&= C_d(\langle P_0^0(\cos\theta)\rangle + \langle P_0^2(\cos\theta)\rangle + \langle P_0^4(\cos\theta)\rangle) \\
&= C_d(\mathcal{P}_0^0 A_0^{(0)} + \mathcal{P}_0^2 \frac{A_0^{(2)}}{2}(3\cos^2\theta - 1) + \mathcal{P}_0^4 \frac{A_0^{(4)}}{8}(35\cos^4\theta - 30\cos^2\theta + 3)) \\
&= C_d'(1 + \frac{\mathcal{P}_0^2}{\mathcal{P}_0^0}\frac{A_0^{(2)}}{2}(3\cos^2\theta - 1)) + \frac{\mathcal{P}_0^4}{\mathcal{P}_0^0}\frac{A_0^{(4)}}{8}(35\cos^4\theta - 30\cos^2\theta + 3)) \\
&= C_d'(1 + \frac{\mathcal{P}_0^2}{\mathcal{P}_0^0}\frac{A_0^{(2)}}{4}(1 + 3\cos(2\theta)) + \frac{\mathcal{P}_0^4}{\mathcal{P}_0^0}\frac{5A_0^{(4)}}{64}(5 + 4\cos(2\theta) + 7\cos(4\theta)))
\end{aligned}
\tag{2.14}
$$

Step by step: starting at the most general expression for an ion intensity that depends on the angle between the laser polarization and molecules' quantization axis, θ, we have a detector efficiency (C_d), a REMPI branch and state dependent line strength ($\mathcal{P}_q^k(J_i, \Lambda_i, J_f, \Lambda_f; \Omega)$), a general moment representing the 'shape' of the angular distribution of momenta vectors ($A_q^{(k)}(J_i)$), and the starting population ($n(J_i)$). Based on our earlier discussion, we will only care to measure the monopole, quadrupole, and hexadecapole moments so we restrict our sum to those particular values taking us to line 2. These moments are still the expectation values of the related Legendre polynomials: $\langle P_0^2(\cos\theta)\rangle$ and $\langle P_0^4(\cos\theta)\rangle$. Moving on to line 3, we set $P_0^0(\cos\theta) = 1$ according to the GZ convention and distribute the $\mathcal{P}_0^0$ term, which will scale our detector efficiency to C_d'. On line 4 we use the double and quadruple angle formulas to reduce the order of the $\cos\theta$ terms to improve the fitting algorithm's performance. This is the exact form we will be fitting to and be able to extract $A_0^{(2)}$ and $A_0^{(4)}$ as fit parameters directly.

The linestength factors $\frac{\mathcal{P}_0^2}{\mathcal{P}_0^0}$ and $\frac{\mathcal{P}_0^4}{\mathcal{P}_0^0}$ for the S-branch transitions of $J = 3$ and $J = 2$ have been calculated by Sitz [34]. The values we have used are in table 2.5.

Table 2.5: Results of Fortran-based calculations performed by Sitz. These are for the S-branch (2+1) REMPI ionization process on H_2. These are used as constants in equation 2.14.

	$\frac{\mathcal{P}_0^2}{\mathcal{P}_0^0}$	$\frac{\mathcal{P}_0^4}{\mathcal{P}_0^0}$
$S3$	$-.47620$	.12470
$S2$	$-.40820$	.08160

2.3.5 Depolarization of Molecular Alignments

It is worthwhile to note that once molecules are pumped into a particular alignment it is not constant. The molecules will depolarize over a given time interval. See figure 2.12. This is a result of **hyperfine depolarization** where the nuclear spin and molecular angular momentum vectors couple and cause the total angular momentum to precess (classically). In the quantum explanation, the expectation value of m_J will be time dependent.

This places a restriction on our experiment: the pumping and the measuring must be done within a half-microsecond of each other. Furthermore we could anticipate any perceived loss of alignment due to this precession and account for it. If we were to use an even J state, the nuclear spin vector will be 0 and there will be no resulting hyperfine depolarization.

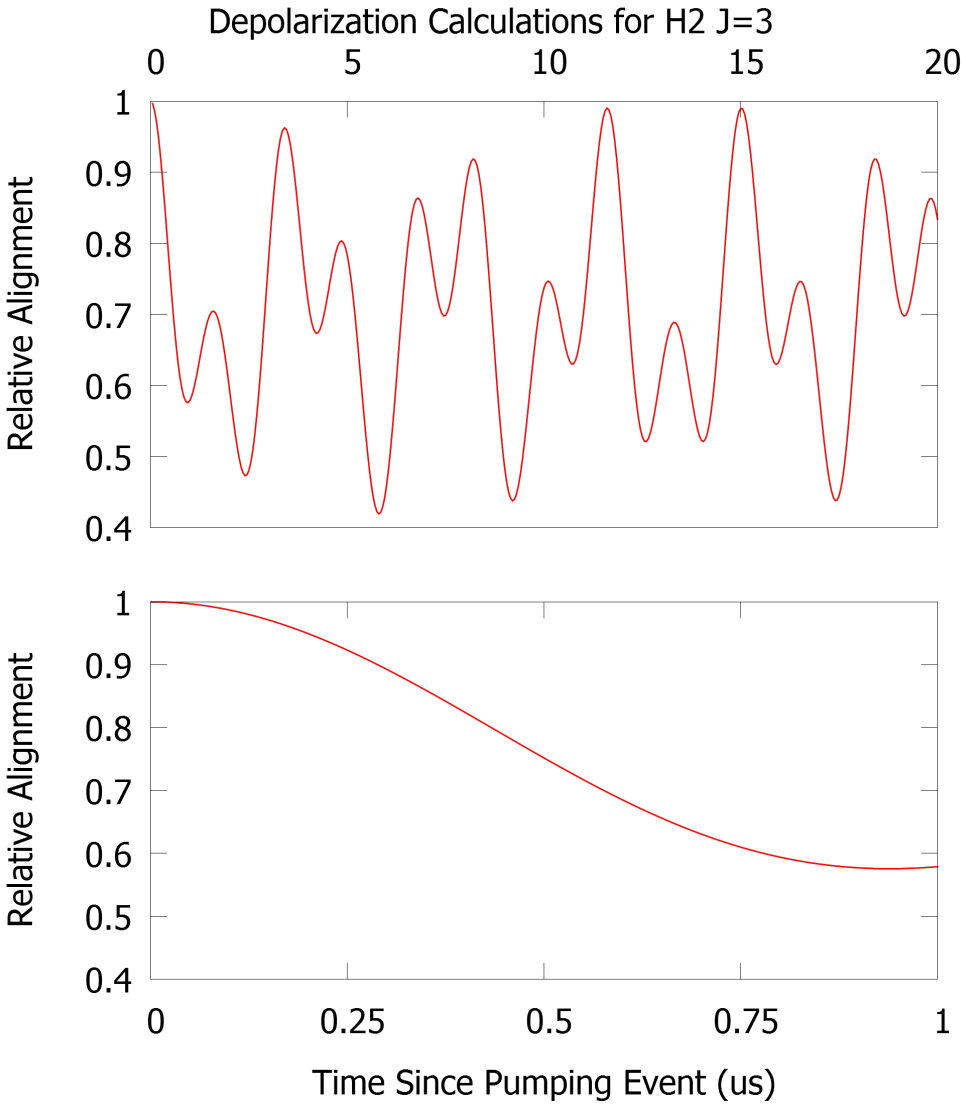

Figure 2.12: Results of a calculations performed based on work by Rutkowski et al [17]. This shows over what time scale an aligned sample of hydrogen will precess. In our experiment we pump approximately 1mm ($\approx$ 80ns of molecular travel) above the surface. The upper figure shows the long timescales as originally reported by Rutkowski. The lower figure is rescaled in time to the scales relevant for our experiment.

Chapter 3

Experimental Apparatus

In this chapter, we review all of the equipment in use in this experiment. This chapter is provided as a helping guide to future students, in particular, the diagrams within. The section on software, 3.6, should be consulted for an understanding of the general structure of the programs required to run the experiment. These programs were a large part of the author's and Chris Reilly's contributions to the lab.

3.1 Scattering Chamber

The primary apparatus for these experiments is the large, two-part vacuum chamber in the southwest corner of the lab near the front door. It is referred to in Rover's control programs as the "Main" and "Source/Buffer" chambers. Students have referred to it as "Pooh" (as in Winnie the) since Dr. Marcia Isakson's time in the lab. Both names are equivalent.

3.1.1 The Art of Making Nothing

The main chamber is subdivided into 3 chambers. See diagram 3.1. The source chamber holds the nozzle and skimmer and is pumped by a 10"

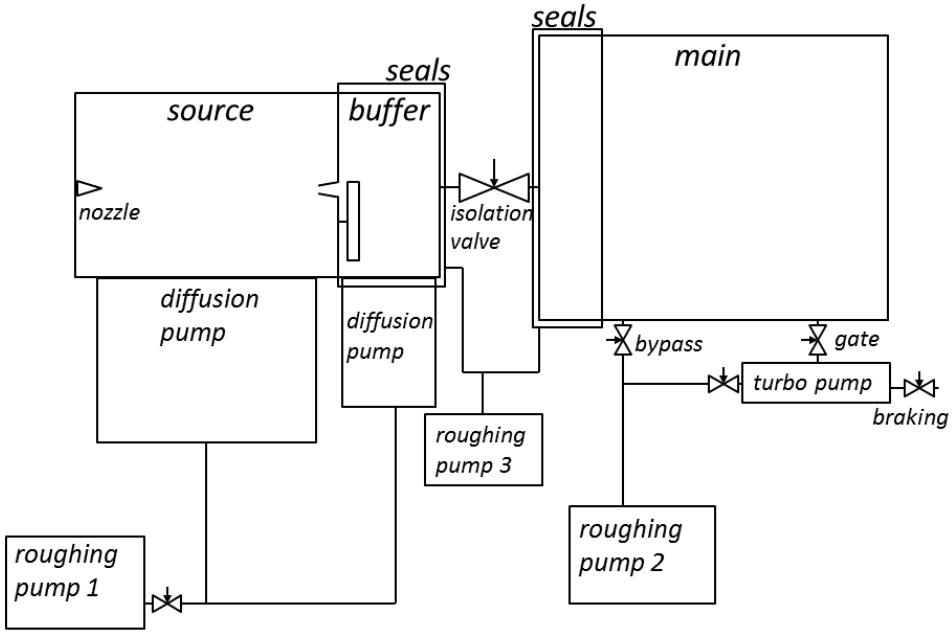

Figure 3.1: A diagram of the vacuum system for the main chamber. All valves are shown. The isolation valves are mechanical, i.e. not controlled by Rover. The braking valve is internal to the turbo pump and is automatically opened when the turbo is turning off.

Varian diffusion pump (HS-10) that is in turn backed by a mechanical roughing pump. The buffer chamber houses the chopper wheel and is pumped by a 6" Varian diffusion pump (VHS-6). There is then a mechanical isolation valve that separates the buffer from the main chamber; this should be closed each night. The main chamber has the surface sample on the manipulator suspended from the lid, electrodes for ion steering and collection, quartz lamps for baking out, an Auger spectrometer system, a LEED imager, and a QMS.

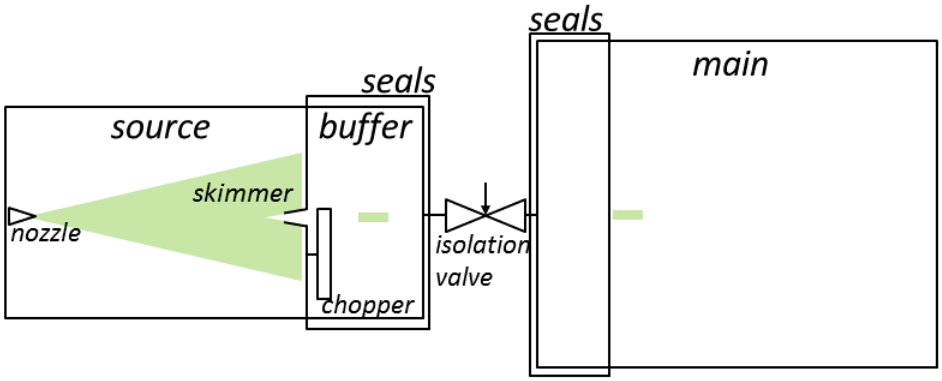

Figure 3.2: A cartoon of how the molecular beam is made inside the 3 chambers. Key pieces of equipment are the nozzle, skimmer, and chopper. The end result is a small "bullet" of hydrogen. These bullets are made at a 10Hz frequency, the operating frequency of all our experiments.

3.2 The Magic Bullet Theory

For all of our experiments, we first must create a molecular source that has a well defined speed and directed towards our surface. This section outlines all the steps taken from a bottle of hydrogen to a small bullet of well behaved molecules directed at the surface. Figure 3.2 is a cartoon depicting how our molecular beam is made.

3.2.1 Supersonic Expansion & the Nozzle

This is done by having a nozzle separate the hydrogen source lines from the high vacuum chamber. The nozzle is pulsed into an open state for approximately $600\mu s$ during which time gas leaks into the chamber. Imagine this action as quickly pressing down on a can of spray paint. The large difference in pressures, source lines are typically 1300Torr (25PSIG) or higher

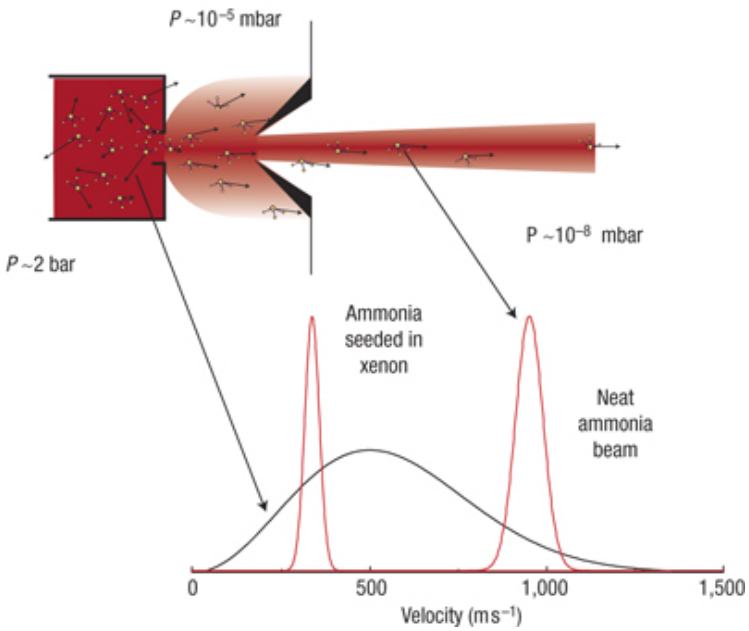

Figure 3.3: A diagram illustrating how a supersonic beam works. We do not use ammonia nor do we need to seed our beam for these experiments but the velocity profile is included as a sample. The pressures listed on the figure convert to: 2bar = 1500Torr, 10^{-5}bar = 7.5mTorr, and 10^{-8}bar = 7.5 $\times 10^{-6}$ Torr. From [18].

and the source chamber is typically 10^{-8}Torr, causes the molecules to undergo supersonic expansion. This means that they quickly go from a random walk, dense gas picture into a kinetic, individual molecule picture. The molecules will continue into the chamber with the mean velocity statistical mechanics dictates for the temperature of the nozzle. As these molecules propagate they experience collisions with one another and equally distribute their momenta resulting in a narrow velocity distribution. Reference [18] has a description of how a supersonic beam works and the key figure is reproduced here as 3.3.

3.2.2 Skimming the Cream

After we open and close the nozzle, one can imagine that we have a hemispherical shell of hydrogen molecules propagating outward in the chamber all with the same speed. We now want to select for those travelling towards the surface. This is done by using a skimmer. The skimmer is a conical piece of thin foil that has a very small, $\approx$ 1mm, opening on the top. The skimmer is very delicate and should not be removed from the chamber unless absolutely necessary. The skimmer is also the only path for molecules between the source and buffer chambers.

3.2.3 Get to the Choppah

The buffer chamber houses the chopper wheel. This is a physical blockade to further refine the velocity of the molecules. The chopper wheel is depicted in figure 3.5. This is mounted on an electric motor, Globe Motors 75A1003-2, and is spun asynchronously at 200Hz. Figure 3.4 shows the electronics used to spin the chopper.

Refer to figure 3.5. The chopper has 2 wide slits and 2 narrow slits, each 90° apart. The narrow slits are used most often when running experiments. There is a small photodiode circuit placed 3/8 of a rotation away from the skimmer/molecular beam axis that provides a binary signal when it sees either of the slits. The chopper motor synchronizer circuit has a "long" (wide slit) or "short" (narrow slit) pulse mode. This circuit provides the $t = 0$ pulse for all the resulting steps in the experiment. The nozzle is opened the appropriate

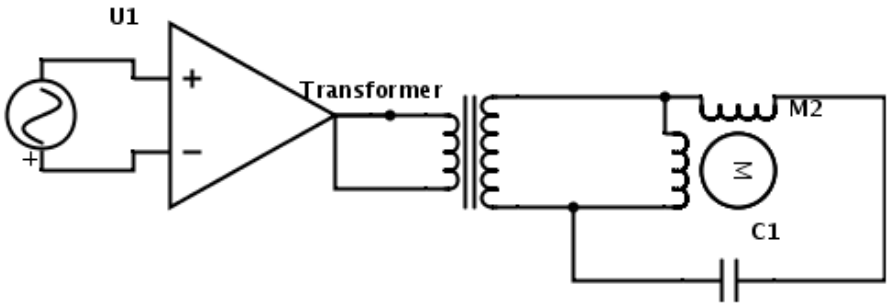

Figure 3.4: A circuit diagram for the chopper wheel driver circuit. The frequency generator makes a 200Hz sine wave that is sent to the AudioSource AMP-100 amplifier which gives the signal more current. This is sent to the step up transformer that takes this $\approx 5V$ signal to $\approx 120V$. There is a phasing capacitor between the two poles of the motor to provide the necessary 90° phase shift.

amount of time after this sync pulse such that the majority of the molecules reach the chopper just as the desired slit is behind the skimmer. For a more thorough discussion of timing, see section 3.6.4

After the beam is skimmed and chopped it will enter the main chamber. At this point it can be thought of as a small cylindrical shaped bullet of hydrogen. It is in the main chamber that the two lasers will interact with a small sample of the molecular beam pulse.

3.3 The Lasers

This experiment uses a standard pump-probe scheme of many modern physics experiments. Consequently, there are two lasers that need to be explained in detail. The pump laser establishes the molecules' state and ori-

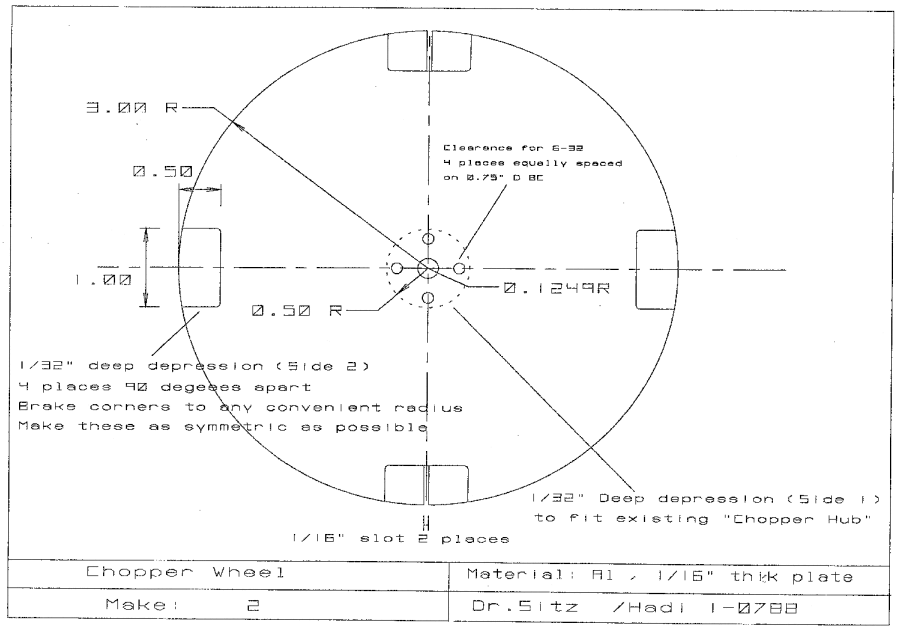

Figure 3.5: A drawing of the chopper wheel. The chopper has 2 wide slits and 2 narrow slits, each 90° apart. The narrow slits are used most often when running experiments. The wide slits allow an appreciable amount of gas through that can be registered on the pressure gauge which can be useful when troubleshooting.

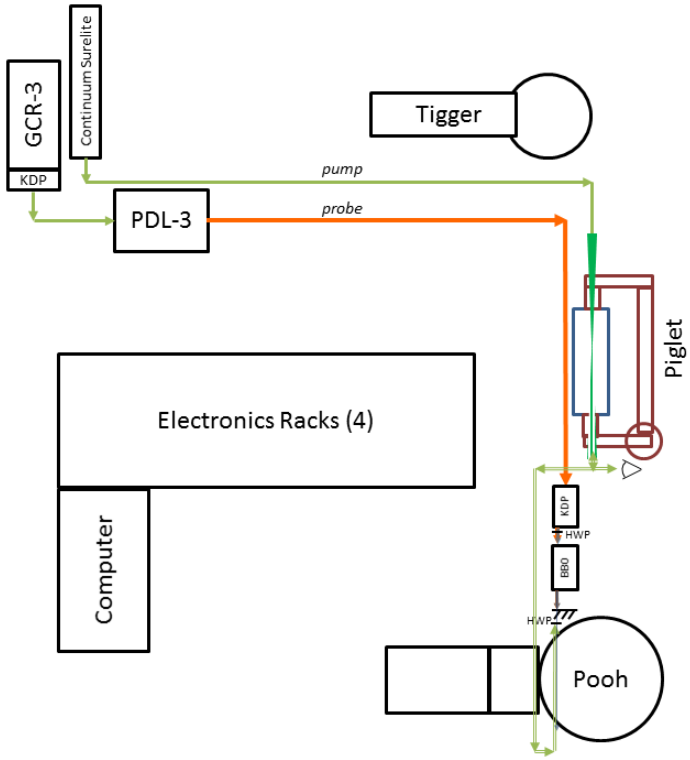

Figure 3.6: A map showing the key optics (lens and mirrors omitted) for the pump and probe lasers. For more details on the pump laser see section 3.3.1 and for more information on the probe laser see section 3.3.2.

entation. The probe laser can image molecules either before or after their interaction with the surface. Figure 3.6 is a schematic of both laser systems with their relative positions and sizes in the lab.

3.3.1 State Preparation: the Pump Laser

At this point in a run, we now have a cylinder of hydrogen molecules coming towards the surface, for details on how this is done see section 3.2.

The rotational and vibrational populations of the molecules are dictated by the temperature of the nozzle and the resulting statistical mechanics. From this randomly oriented sample of hydrogen we must make an aligned subset by pumping them with a SRS laser.

3.3.1.1 The SRS Cell - Piglet

Our pump laser starts as the standard frequency-doubled YAG: a Continuum Surelite II. It is set for $\approx .42W$ of 532nm (green) light pulsed at 10Hz. This light is then directed into our SRS cell, named 'Piglet'. Looking at figure 3.7, Piglet is a closed loop of pipe which can be circulated with hydrogen gas. On one leg of the loop, there are windows for the 532nm light to shine through. On this same leg there is a vacuum insulated, liquid nitrogen reservoir that cools the gas to 77K. The cold can is also a vacuum insulated liquid nitrogen reservoir houses a zeolite material inside a coiled section of tubing. The zeolite helps catalyse the conversion from ortho- to para-hydrogen (flips the nuclear spins). For a detailed explanation of the workings of Piglet see M. Irrgang [35].

When the 532nm laser enters Piglet, the intensity of the light and density of hydrogen is sufficient to begin the nonlinear optical phenomenon **Stimulated Raman Scattering (SRS)**. Figure 3.8 is a sample spectrum of the light after it leaves Piglet. For an explanation of SRS see section 2.2.2. Using Piglet, we can pump beam molecules from either $J = 1 \rightarrow 3$ or $J = 0 \rightarrow 2$. This change of 2 preserves antisymmetry for the molecule's wavefunction.

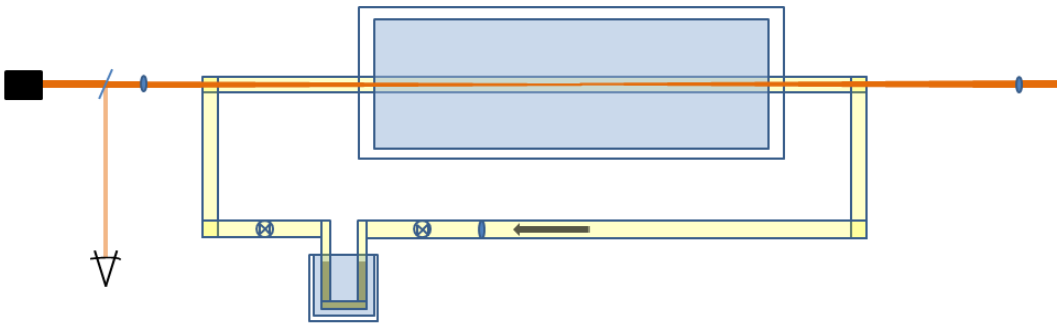

Figure 3.7: A diagram of the Piglet apparatus used to make SRS pump light. Hydrogen gas is depicted as yellow and liquid nitrogen is depicted as blue. The first optic is a convergent 1m AR coated lens. The second optic is a convergent .75m lens to recollimate the pump light. The spectrometer is positioned to look at diffuse scatter off of the exit window, drawn here as a splitter. The black box represents propagation onto the experiment chamber.

3.3.1.2 Polarization of SRS Light

We have described how the pump laser can rotationally excite beam molecules but this does not explain how we align those molecules with respect to the surface. *The axis of polarization of the pump laser determines the m_J axis of the beam molecules.* As a direct consequence we must make our circularly polarized SRS light linearly polarized. One would normally use a quarter-wave plate for converting from circular to linear polarization however that is not feasible with SRS light because the adjacent side-band wavelengths are of opposite helicity which will result in orthogonal linear polarizations [2] p.43. Thus we use a polarizing beam splitter which will only propagate one component of the polarization while ejecting the opposite in an orthogonal direction. This rejected polarization component is then wasted reducing our pump laser power by a factor of 1/2. This beam splitter places a power

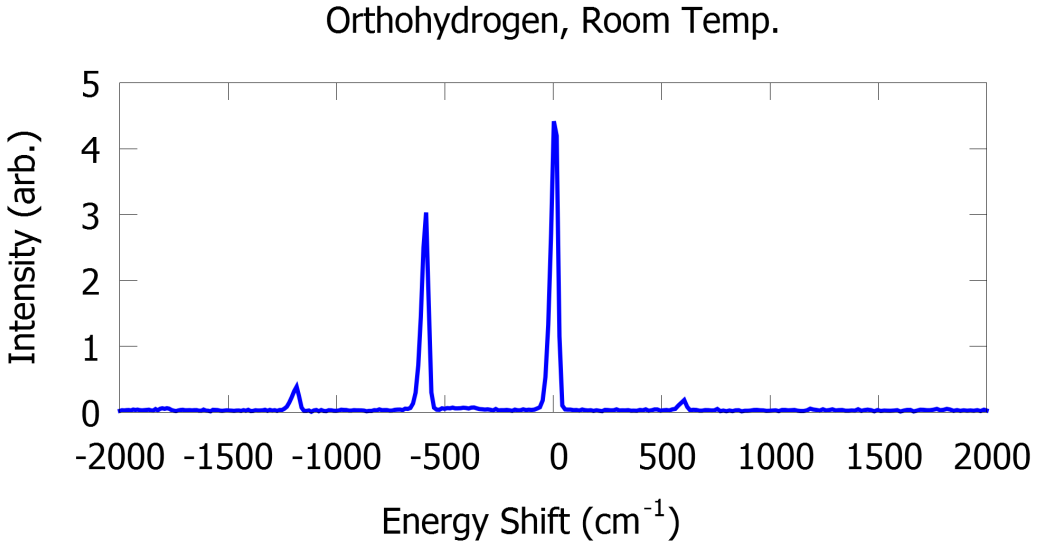

Figure 3.8: A sample spectrum of the SRS light that leaves the Piglet apparatus and is sent to Pooh (the main chamber) as the pump laser. The primary component at 532nm is the incident laser wavelength, i.e. this is light that does not interact with the hydrogen inside Piglet. The new component at $-530cm^{-1}$ is the first Raman shift as an incident laser photon rotationally excites a hydrogen molecule.

restriction on our pump laser intensity.

3.3.2 Ionization & Detection: the Probe Laser

Refer to figure 3.9. Our probe laser begins as a standard frequency doubled YAG, 532nm, 3.2W pulsed at 10Hz, a Quanta-Ray GCR-3. It then is directed into a Quanta-Ray PDL-3 dye laser, see section 2.1.2 for principles of operation, that has Rhodamine-640 dye dissolved in methanol. Rhodamine-640 gives a tunable laser source centred at 602nm, see figure 3.10. The PDL-3 has an adjustable diffraction grating that is used to select a narrow wavelength, $\approx .02nm$, for the resulting laser beam. Outside the PDL, the beam is telescoped down to $\approx .5''\varnothing$before being sent to the nonlinear crystals.

The first nonlinear crystal is monopotassium phosphate (KDP). It is an efficient frequency doubler and will convert *some* of the variable $\approx 602nm$ into $\approx 301nm$. In the second nonlinear crystal, beta barium borate (BBO), we sum frequency generate (SFG) one principle photon ($\approx 602nm$) with one doubled photon ($\approx 301nm$) to generate $\approx 200nm$ light. By tuning the dye laser wavelength, we can tune the resulting deep UV third harmonic light to ionize hydrogen. Even at these short wavelengths, hydrogen still requires 3 of these photons to ionize. This ionization is the Resonantly Enhanced Multi-Photon Ionization (REMPI) process that is explained in section 2.2.3.

Students should note that when the dye wavelength is changed the KDP and BBO crystals will need to be retuned. These crystals are angle tuned in order that the generated light is phase matched inside the crystal, see

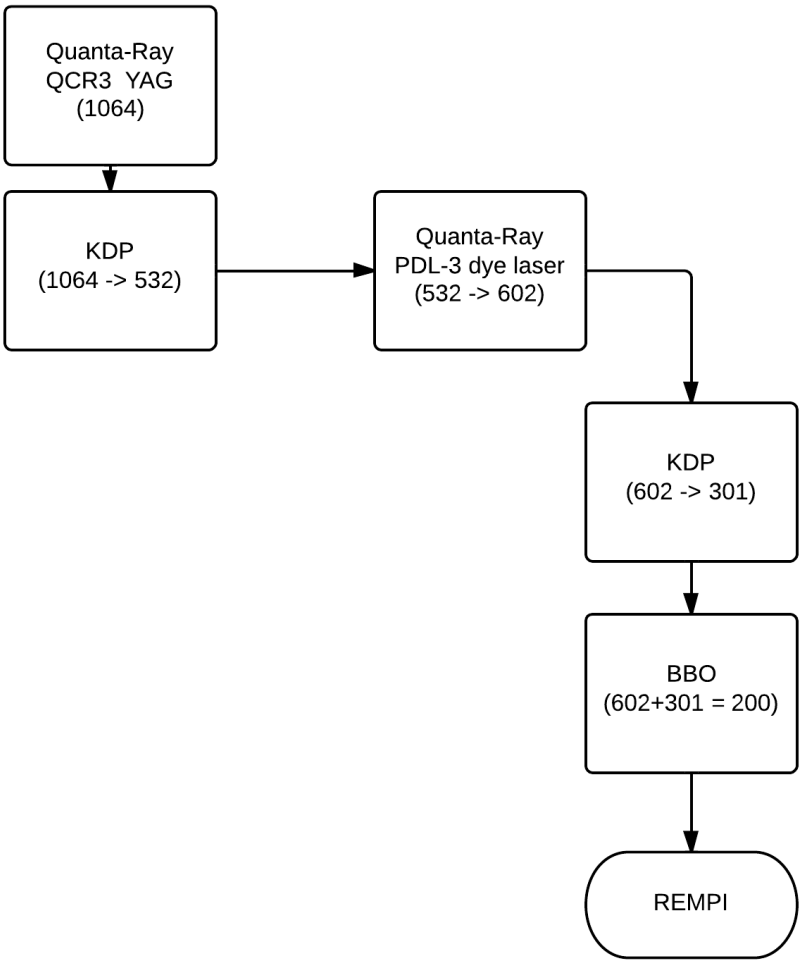

Figure 3.9: A flowchart outlining each wavelength conversion process used in the probe laser set up. All wavelengths are in nanometers.

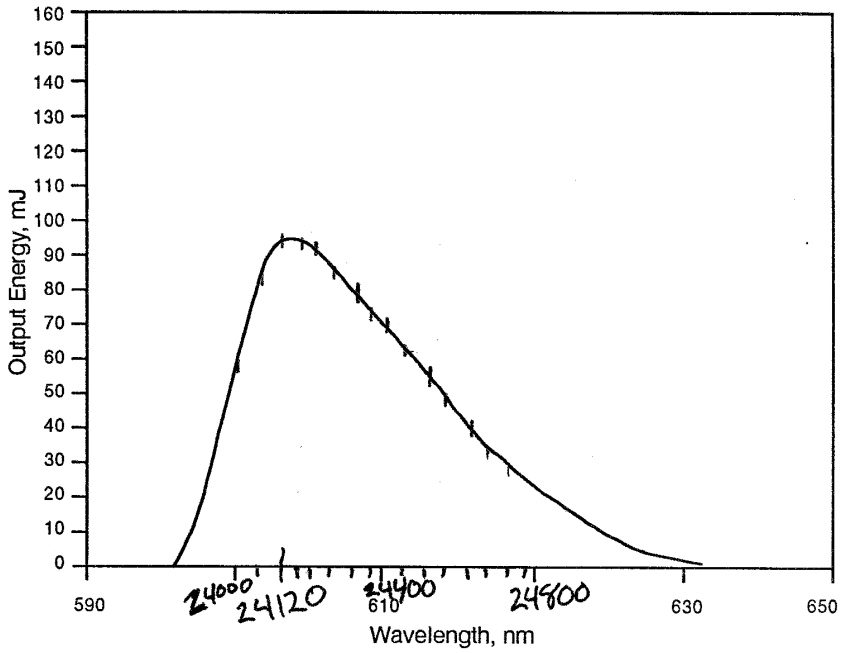

Figure 3.10: The response curve showing the tunability of Rhodamine 640. The handwritten numbers are the PDL dial values corresponding to those wavelengths.

section 2.2.1. The tuned angle is both wavelength dependent and temperature dependent. This system is far from ideal and when you are first learning to operate the experiment, you will struggle with the art of keeping the crystals in tune.

After BBO, the probe laser is comprised of 3 wavelengths, only the VUV one of which we are able to use to make ions. Thus we dump the remaining orange light using several flat pieces of glass that are reflective below the orange wavelength and direct the VUV through a half-wave plate that is mounted in a rotation mount and stepper motor. This allows us to rotate the polarization direction of this linearly polarized light and sample different orientations when at alignment dependent wavelengths. After this, the light is shown through the main chamber's north window which houses a focusing lens. Depending on the wavelength and polarization direction of this light, we can ionize various states and alignments of molecular hydrogen, see section 2.2.3.

3.3.2.1 Ion Collection

Finally we intend to ionize hydrogen with the probe. These ions must be collected and "imaged" to make observations. Enter the steering voltage plates and the Multi-Channel Plate (MCP), see figure 3.11. There is an extractor plate which has a moderately high negative voltage applied to it to draw the ions out from amidst the molecular beam and towards the MCP. The four steering plates, top, bottom, right, and left, provide control to focus the ions onto the MCP. The ions are then collected on the MCP which sits at yet

a higher still negative voltage to ensure the ions are drawn onto it. This ion current is amplified and sent externally to the chamber where it can be measured on the oscilloscope and recorded by the National Instruments DAQ board attached to the lab computer.

It is worthwhile to note that the MCP bias voltage is pulsed to provide a windowing that allows us to filter out ions from other sources being drawn into the MCP. Typically the MCP is biased at a constant -1250V and pulsed up to -1800V just as the probe laser Q-switch signal is sent to the laser. The result of this high voltage pulsing is observation of the "switching noise" on the ion current. The ions of interest will always fall within the bounds of the switching noise.

3.4 Making it All Work in Concert: Timing

Now that we have described the molecular beam, section 3.2, and the two lasers, section 3.3, we must explain how these work in concert. Since the duration of each laser pulse is $\approx 10ns$ and the molecular beam is $\approx 10\mu s$ long, establishing precise delays between these 3 events is pivotal to the experiment. These delays are depicted in figure 3.12. To make this easier and more concise over earlier incarnations of the control system, the author along with Jules Stuart, created the Digital Delay Generator (DDG).

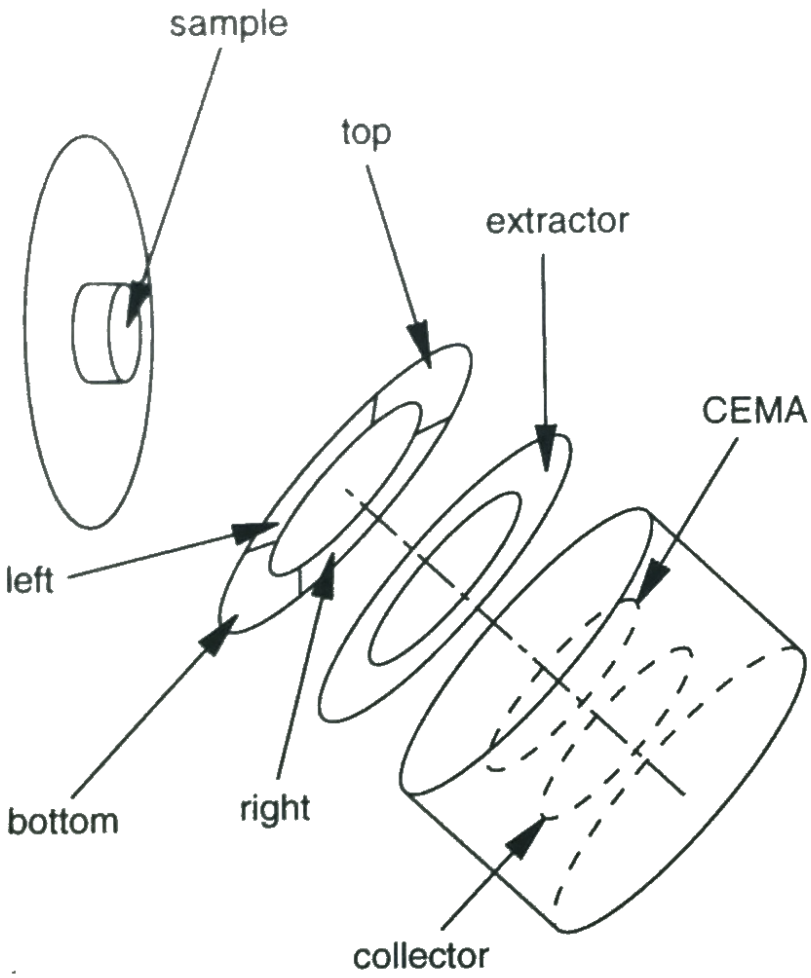

Figure 3.11: A sketch of the ion collection system where the steering plates direct the freshly made positively charged hydrogen molecules down onto the multi-channel plate. From M. Gostein's notes.

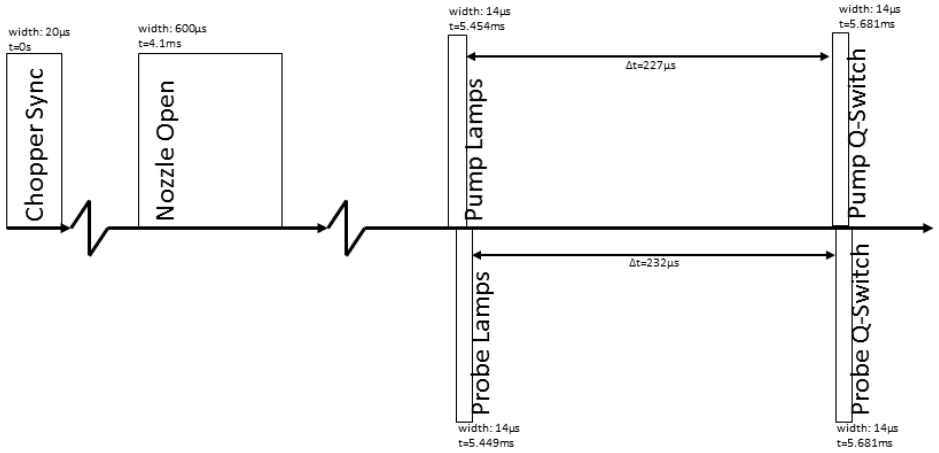

Figure 3.12: A diagram of the relevant timing signals that are generated. The specified start times are dependent on the speed of the chopper wheel. While the probe laser times are swept, they are swept on the order of 100ns which isn't visible on this scale.

3.4.1 The Digital Delay Generator (DDG) Circuit

The digital delay generator circuit is show in figure 3.13. There is extensive documentation written by Jules Stuart: [19]. If there are any problems with any of the DDG modules this document should be consulted. Here is a condensed theory of operation: in each DDG there is a fast and slow delay stage which are both programmed via an Arduino microcontroller inside the unit. The slow stage is a bank of 5 counters on the east side of the board which count whole periods of the onboard 10MHz clock (the drawing has a typo which says 20MHz). When the counters have finished counting the flip-flops are tripped which starts the charging of capacitor C4 (southwest corner) via a constant current source made by transistors Q1 and Q2. The voltage on the capacitor is compared to the programmed value of the DAC08 chip.

When the charging voltage equals the programmed voltage, the circuit fires by sending an output signal to the output amplifiers.

The Arduino is interfaced with directly by the delay generator suite of our Python programs, see section 3.6.4. It is loaded with a "driver" sketch which is set up to expect a certain input format over a USB connection from the computer. The sketch will take the requested delay, compute the number of clock cycles and the voltage level that must be generated by the fast stage for the comparator. This data is then sent from the Arduino to the onboard shift registers through a bitshifting scheme.

Currently, there are few limitations with our design. It has a random jitter between multiple units of exactly 1 clock cycle. This jitter happens with roughly a 2% occurrence rate and can be seen easily if observing the photodiode signal and watching the relative delays in pulses between the pump and probe lasers. This problem is exaggerated when more units have their clocks shared, thus why only the two Q-switch units share a clock. Clocks can be buffered to prevent this issue but it was not known at the time of design. Secondly, the intended accuracy of 1ns is generous: it is actually accurate to 2-3ns. Both of these problems can be avoided in a future design which should be done using Surface Mount Technology (SMT) because faster components exist solely in this form factor.

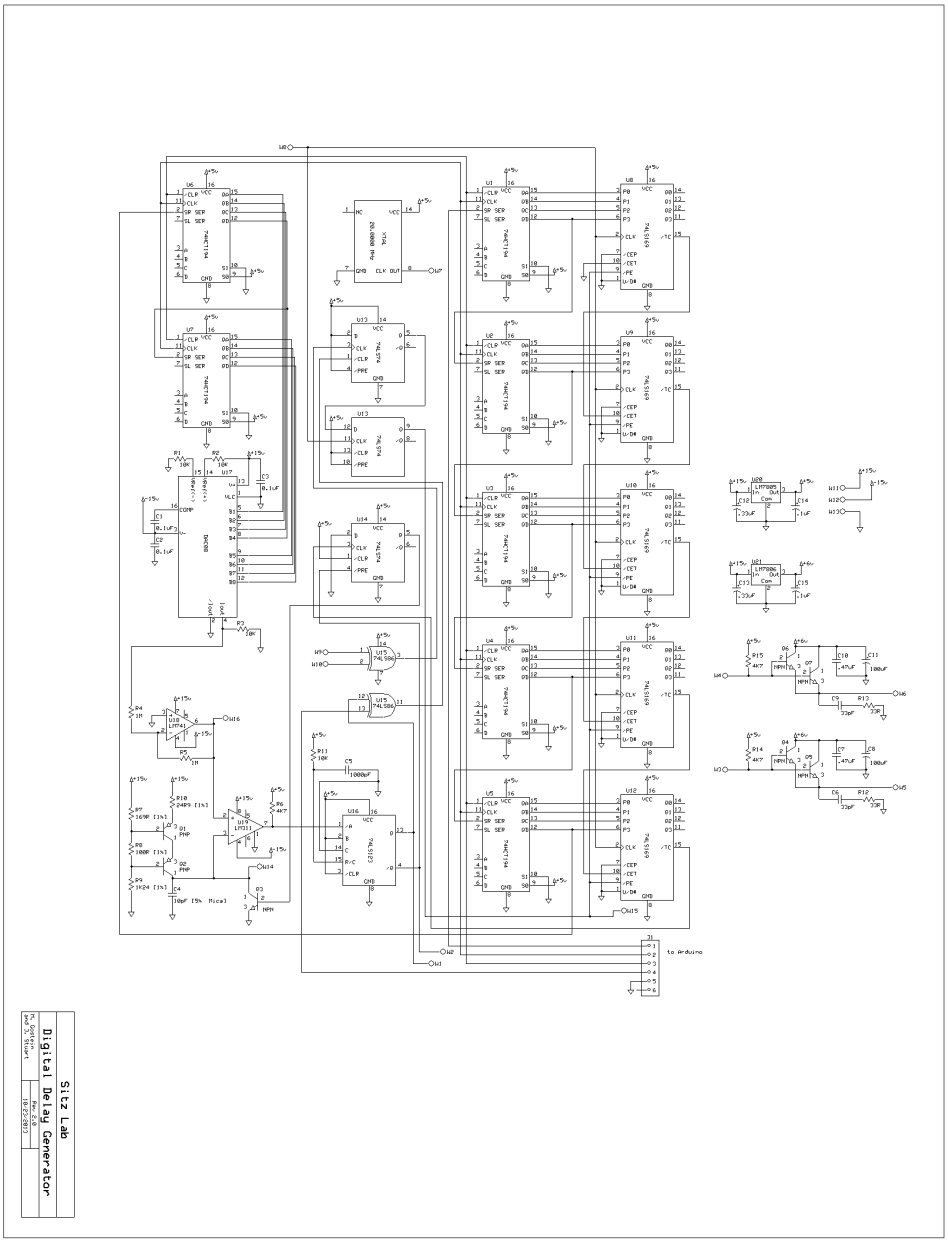

Figure 3.13: The circuit diagram for the DDGs. Reprinted with permission from J. Stuart, [19].

3.5 The Surface

For these experiments a sample of Silicon(100) is used. It is suspended below the rotatable chamber lid on the surface mount system that is often referred to as the "tophat". This is depicted in figure 3.11.

3.5.1 Surface Temperature

The surface temperature is monitored by a thermocouple attached directly to it. The temperature is regulated by a filament ribbon that is mounted directly behind the surface with a controllable current flowing through it. A homebuilt circuit monitors the surface temperature, compares this to a set point temperature, and regulates the filament current accordingly. The manipulator structure is water cooled with the same pump system as the chopper motor cooling.

3.5.2 Cleaning

In order to clean the surface we first monitor the chamber pressure by setting the QMS to the 18AMU-water peak and slowly increase the filament current at a lower voltage ($\approx 500V$). This will first eject material from the filament. Once the filament is clean, i.e. there is no pressure dependence on variable current, the voltage can be slowly increased towards the operating value of 1kV. As the filament bias voltage is increased, a current should be put through the filament and cleanliness should be confirmed. In this process we are cleaning the surrounding materials of the mount. Once we are at

1kV we will certainly be cleaning the surface by heating it with these ejected electrons from the filament. We heat it to 600C for a few minutes and we see no noticeable change in the QMS signal for variable filament currents. It is suspected that, at the time of writing, the thermocouple has partial contact with the surface and the actual temperature is much higher than 600C.

3.6 Software Developments

A recent development in Sitz lab has been our complete conversion from Fortran 77 operating code to Python 2.7. This has been solely a project begun by the author and Chris Reilly. The source code can be downloaded by anyone through Github: `https://github.com/creilly/sitzlabexpcontrol`. It is protected under the GNU license (open source).

In general terms, our software operates National Instruments DAQ devices to collect and generate signals to interface with other devices. This role is normally occupied by LabView, however this can be very restrictive with a steep learning curve for new students. Python is the polar opposite of this. Students that do not have any programming experience should spend some time learning Python at CodeAcademy `http://www.codecademy.com/en/tracks/python`.

For help specifically with our code, you should read the documentation in the project's documentation folder. Great care was taken to comment the code (and it should be maintained!). If there is ever a question about what device should be plugged into what channel, that information is kept

dynamically in the config folder, this is what programs refer to at runtime.

3.6.1 Design Principles

We have written every program in a highly modularized object-oriented fashion. This is the first rule of the software project: to **write code in as many generalized small chunks as possible in order to reduce duplication of code**. At first glance, this makes the size of the project daunting. The first, of many, advantage of this style is that our programs are easily diagrammed out, see figure 3.14.

The second-most important design principle of this project is **to keep it simple**. Code should be written in as few lines as possible while still being human-readable. Python is a beautiful language where most of that beauty emanates from its simplicity. It is easy to write ugly code that nobody else can read, update, or fix. Writing bad code is a good way to have your contributions erased by a future student. Pay good code forward.

The third and final rule of the project is: **comment, comment, comment**. Comments are easy. They take very little time if you comment as you write your code. In fact, if you start by making a plain text outline of a program, those bullet points easily become your comments. Code without comments is the worst thing you can inflict on another human being.

Each class of device (e.g. stepper motors) has a whole suite of programs written for managing those types of devices in the lab. The suites all follow the flowchart shown in figure 3.14. Individual devices are separate objects

that are all managed by a **server**, e.g. steppermotor/steppermotorserver.py. Users are not allowed to interface with servers directly and unless the computer loses power the servers should always be left running. A server is interfaced with through a **client** which can either be a command-line version, e.g. steppermotor/steppermotorconsoleclient.py, or a graphical version, e.g. steppermotor/steppermotorgui.py. Both of these clients will use many of the same commands to interface with the server so these are stored in a mini-library called the **client mini-library**, e.g. `steppermotorclient.py`.

3.6.2 Stepper Motor Suite

At the time of writing, five key devices in operating the experiment are attached to stepper motors. They are: the PDL, the KDP crystal, the BBO crystal, the pump laser polariser, and the main chamber lid. Each stepper motor is configured in a redundant read-write configuration where every step that is written by the software is read back in hardware. This was done originally as a troubleshooting measure but was kept because it was convenient for maintaining absolute calibration. Each stepper motor then occupies at least 4 hardware channels: write steps, write direction, read steps, and read direction. The lid and polariser are also connected with an enable relay making a 5th channel. A table of what devices are plugged into which hardware channel is omitted here; it is apt to change as new students come into the lab. You should refer to the config folder for any such connection issue.

In accordance with our design principles, see section 3.6.1, steps are

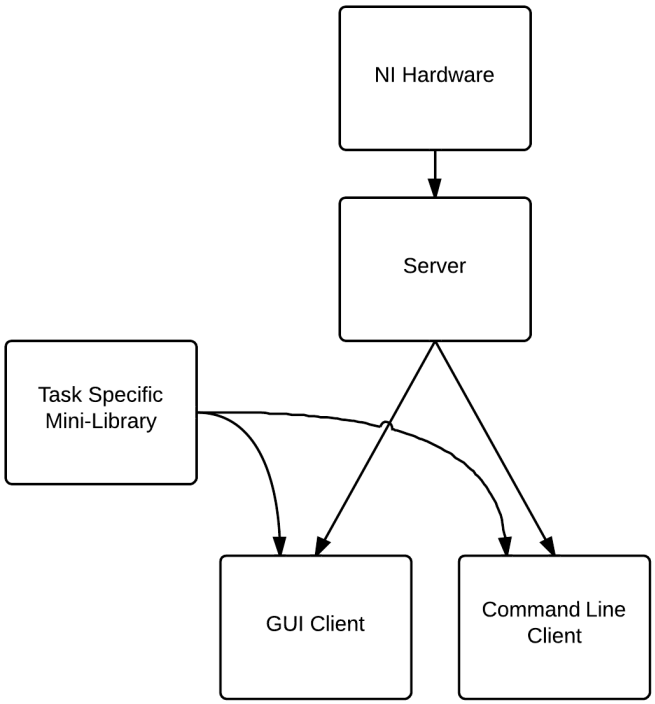

Figure 3.14: A flowchart of how each software suite is organized. There exists a suite for every class of device used in the experiment (e.g. stepper motors or delay generators).

measured or generated by a server and read or written by either the console client or a graphical version. Both clients inherit methods to interface with the server from the stepper motor client library.

In addition to the stepper motor programs, there are some ancillary programs that run alongside to make operating the experiment easier. They are the wavelength server and client that maps the stepper motor position of the PDL grating from "step-space" to "wavelength-space". Much care was taken to also give this server the ability to "track" the wavelength which makes the KDP and BBO crystals follow along as the wavelength is changed in an effort to keep third harmonic power constant. Analogously, albeit not as complicated, there exists the polariser server and client which maps the probe laser's half-wave plate from "step-space" to "degree-space".

Table 3.1: List of programs for controlling stepper motors throughout the lab. Asterisks indicate required use at time of writing.

function	program name
*server	`steppermotorserver.py`
basic client	`steppermotorconsoleclient.py`
*GUI client	`steppermotorgui.py`
*custom library	`steppermotorclient.py`
tracking server	`wavelengthserver.py`
GUI tracking client	`wavelengthgui.py`
HWP server	`polarizerserver.py`
HWP GUI	`polarizergui.py`

3.6.3 Voltmeter Suite

As with any experiment, there are voltages that need to be measured and recorded. For our experiment there are currently six key voltages that we record: dye laser photodiode, dye laser power meter, crystals power meter, crystals photodiode, and the MultiChannel Plate (MCP) integrated signal (i.e. ions made by the probe laser). In accordance with our design principles, see section 3.6.1, these voltages are recorded by a server and stored there until read by either the console client or the graphical client. Both clients inherit methods to interface with the server from the voltmeter client library file.

Table 3.2: List of programs for collecting voltages. Astrisks indicate required use at time of writing.

function	program name
*server	`voltmeterserver.py`
basic client	`voltmeterconsoleclient.py`
*GUI client	`voltmetergui.py`
*custom library	`voltmeterclient.py`

3.6.4 Delay Generator Suite

In order to make both lasers and the nozzle operate according to the timing diagram, see figure 3.12, we have the delay generator suite. According to the design principles, section 3.6.1, we have the server that manages the individual delay generator circuits, see section 3.4.1, and is interfaced with through the graphical user interface. The GUI inherits client-specific methods from the mini-library.

Table 3.3: List of programs for managing timing in the experiment. Astrisks indicate required use at time of writing.

function	program name
*server	`delaygeneratorserver.py`
*GUI client	`delaygeneratorgui.py`
*custom library	`delaygeneratorclient.py`

A key feature of the delay generator server is the partnering of two delay generators. This allows you to keep one delay generator at a fixed time shift with respect to its partner and vice versa. This is especially useful for operating the lasers which need two signals: a lamps fire signal and then approximately $230\mu s$ later a Q-switch fire signal. This feature can be overridden in the GUI which acts at a server level, thus if you disable the partnering in the delay generator GUI and another program changes the delay (e.g. smartscan.py, see 3.6.5) the partner will not change its delay. This allows for easy optimization of laser power for relative lamp to Q-switch delay.

3.6.5 Scanning Application

Putting all these programs together, sections 3.6.2, 3.6.3, and 3.6.4, we are able to perform experiments. A distinct advantage of our design scheme, section 3.6.1, of having a server-client pair is that we can write a single program: `apps/smartscan.py` that scans an independent variable on one server while measuring a dependent variable on another. For example, we can sweep the probe laser Q-switch delay and measure the integrated ion signal (MCP) on the voltmeter server. This amounts to imaging the molecular beam's phys-

ical extent. This is only a simple example, there are many experiments that smartscan.py allows you to perform and it will be the primary program with which users interface.

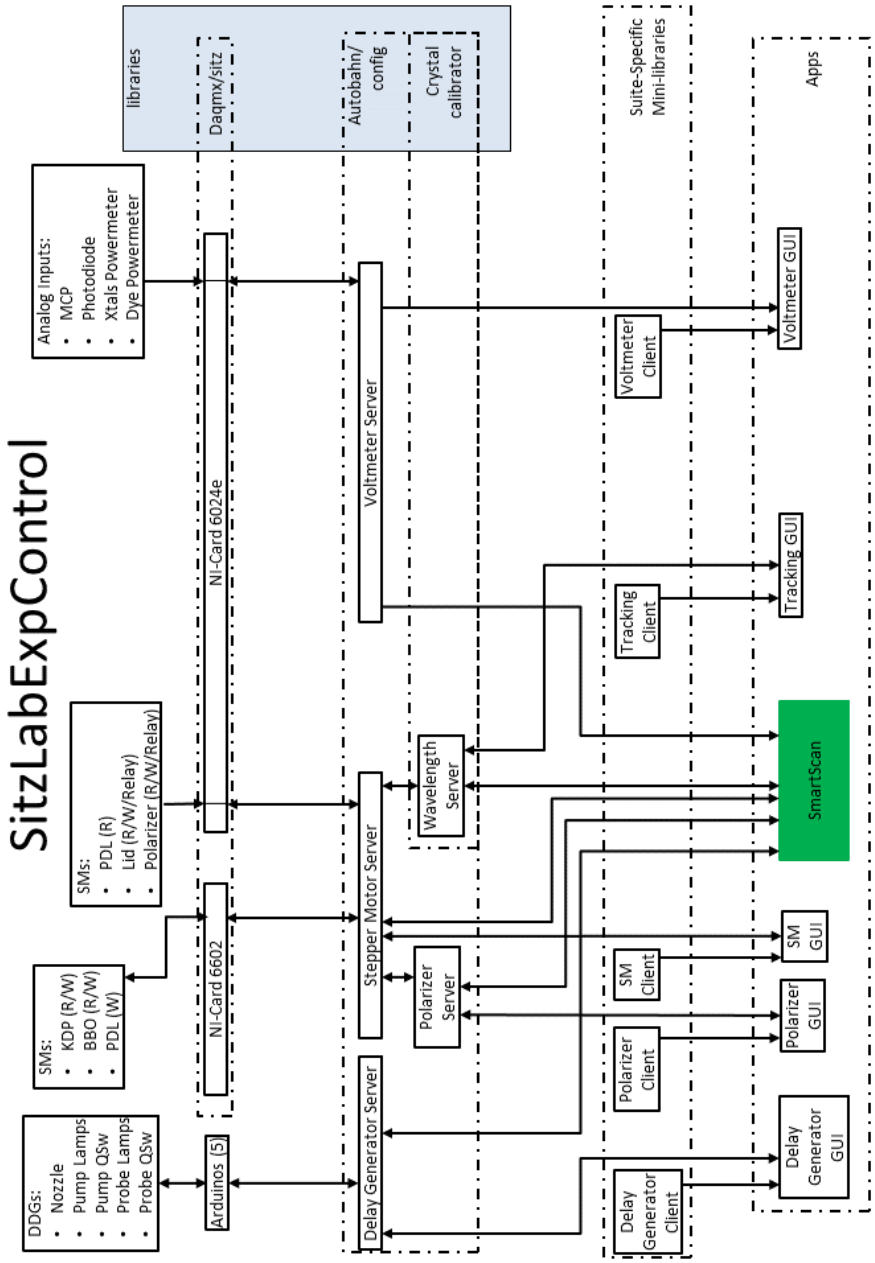

Figure 3.15: A flowchart showing all three suites and how they work together with hardware.

Chapter 4

Experiments

In this chapter we first outline all the calibration experiments that must be done before one can scatter molecules off of a surface. These experiments result in a characterization of the molecular beam and finding the proper timing delays and alignment for the pump and probe lasers. These experiments are necessary for any future students to perform and are presented in the order in which they should be completed: that of increasing difficulty. This chapter can be seen as a detailed roadmap where the only the final destination will differ. Said final destination in our case will be the novel experiment that is the nucleus of this dissertation.

4.1 Characterization of Molecular Beam

We must first generate a molecular beam pulse: without any molecules there would be nothing to interact with the surface. Future students should use these values to get a sense of scale and relative accuracy needed to make the specified observation. The absolute values will be different after any one of the lasers' prisms or micrometers are adjusted, lab temperature changes, nozzle temperature is changed, or a myriad of other variables that can drift.

We will do all the following experiments with the surface not in the scatter position.

A quick note about laser power requirements: as you progress through these experiments you will need more and more laser power to observe weaker and weaker fluences of molecules that have weaker linestrengths. Most of the molecular beam optimization can be done with a modest 1mW of third harmonic energy. In contrast, to observe the S3 reflection off the highly corrugated Si(100) surface required a strenuous 6mW. Laser power is your primary concern moving forward; if you expect to see something and don't, this is your likely culprit.

4.1.1 Centering on Maximal Molecular Density

As explained in detail in section 3.2, the molecular source in our experiment is pulsed, skimmed, and chopped, all before reaching the vacuum chamber where the surface lives. The skimmer is a fixed, metal conical section so it is not a timing concern. The chopper wheel is spun at some rate, for these experiments 250Hz, and as these slits pass between a LED and photodiode we obtain a signal that we can count cycles of and generate a $t = 0$ signal for our experiments. We must then open the nozzle at the right time such that molecules will reach the chopper as the desired slit comes around. The nozzle is typically opened for $600\mu s$ which is much longer than the slit open duration, as will be shown. We will back the nozzle with $50PSIG$ of high purity H_2 and pulse with $84.3V$. These parameters were found to work

but some other combination could be better suited to your application. Beware that these variables are coupled to the time of flight of the molecules. Let's put this into practice by performing experiment 4.1. For this experiment you will just watch the main chamber pressure readout, or you can set the computer up to record. You're only looking to get a slight pressure rise of a $\approx 2 - 3 \times 10^{-10} Torr$ and we will more accurately tune this parameter using ions in a minute.

Experiment 4.1: Nozzle Delay Tuning - Coarse

Independent Variable:	nozzle delay
Dependent Variable:	main chamber pressure
Goal:	get molecules into main chamber
Example Value:	$2.2 \pm .1$ ms

Once there are some molecules reaching the main chamber we can begin to use the probe laser to measure the molecular beam. The particular rotational state observed is not vital for this experiment. One of the thermally populated Q-branch transitions are obvious choices for their abundance of molecules and substantially stronger linestrength. Once the probe laser wavelength is set close (within .2nm) to one of these resonant wavelengths, we need to find the molecules that are reaching the main chamber. Vertically the molecular beam is roughly .4in wide and will be about 30 μs long for a $250 Hz$ chopper speed. You will see something even if your focus is set before or after the molecules because the Rayleigh length of the lens is on the order of the molecular beam width. Thus we should start with a wide time scan on

the probe Q-switch in increments less than 30 μs and keep an eye on the raw MCP signal (not integrated yet). This is experiment 4.1.

Don't forget that now that we're attempting to observe ions so the MCP should be turned on with its voltage pulsed from $1200V$ to $1850V$ triggered off the probe laser Q-switch signal and the steering voltages should be set to the free space values. Example steering voltages are given in table 4.2.

Table 4.2: Sample Steering Voltages

Electrode	Surface Far Away	Surface Scatter
Extractor	-27V	-295V
Bottom	-11V	-335V
Top	-19V	-13V
Right	-203V	-127V
Left	-114V	-79V

The ionization signal should look something like figure 4.1. We will digress a moment to discuss all the features shown on this trace to orient new users. Key features (from left to right) are the photoelectron peak, gain switching noise, ion signal, and reverse gain switching noise. The gain switching noise events result from the high voltage being gated on the MCP typically from 1200V up to 1850V. The photoelectron peak will be much higher once the probe laser is in proximity to the surface and can be used to find the lid angle for which the surface is parallel to the laser. These photoelectrons are a result of light being scattered into the MCP and then liberating electrons. This must be the case because the steering electrodes are kept at negative voltages *orders of magnitude* higher than the available kinetic energy of liberated

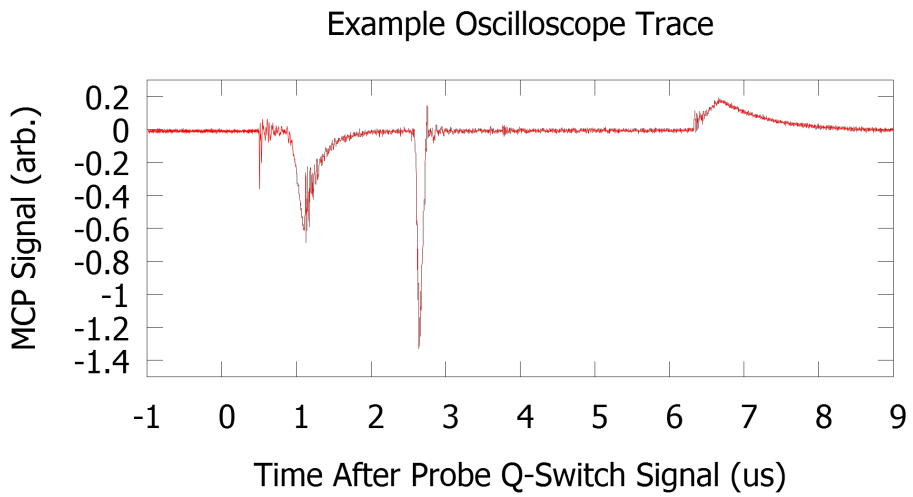

Figure 4.1: A sample trace of the oscilloscope showing the amplified voltage on the MCP. Key features (from left to right) are the photoelectron peak, gain switching noise, ion signal, and reverse gain switching noise. This trace was taken at Q2 for unpumped molecules when the surface was out of position. Once the surface is in position the photoelectron peak will be roughly 5 times stronger.

electrons. Any ion signal higher than the depicted will begin to saturate the MCP and higher fluences of ions will no longer be linear. If you are trying to make quantitative measurements at brighter lines such as Q1 or pumped Q3 you should use neutral density filters on the probe beam to limit the available laser power present in the chamber.

Now that we are seeing some molecular ionization it is time to make that signal as big as possible by iterating through nozzle delay, probe wavelength, probe Q-switch delay, probe vertical, and probe focus. To make this maximization quantitative we'll be using the gated integrator centered on the molecular beam pulse. Be careful to have the gate set wide when doing a vertical scan because the arrival time of the ions will differ significantly as they are produced closer or further from the MCP. Iterating through these variables will need to be repeated to bring the beam into an optimal configuration but will not need to be repeated unless the chamber is vented. These experiments will be quick and are really of the same goal so we've considered them as a single experiment: 4.3.

It is worth noting that the steering voltages can influence the observed ion flux, albeit slightly. You should take a moment now to play around with them and get a feel for how de-balancing the top/bottom or right/left pairs can cause the molecules to miss the MCP. This will give you a feel for the tolerance. Some example steering voltages are given in table 4.2.

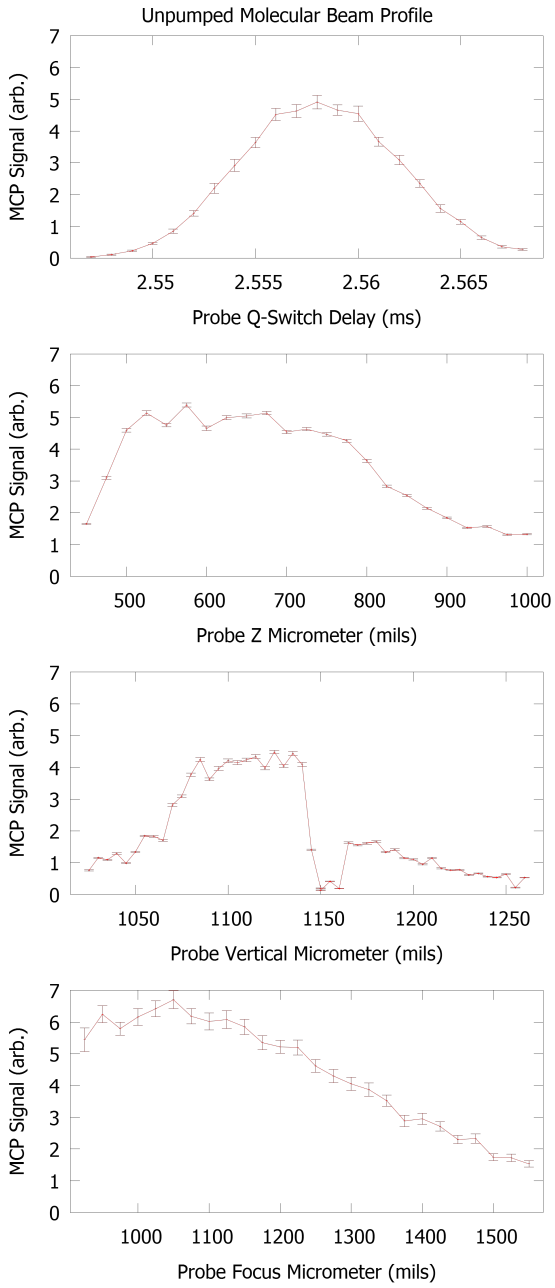

Figure 4.2: Examples of scans over all 4 probe dimensions showing the extent of the molecular beam pulse. We will want to centre up on the peak of each of these and align our pump and probe lasers there. It is worth noting that the Q-switch delay (time) and the molecular beam travel direction (z) are coupled.

Experiment 4.3: Molecular Beam Tuning

Independent Variables:	nozzle delay, probe wavelength, probe delay, probe vertical, probe focus
Dependent Variable:	Q3v0 ions
Goal:	set probe on most dense section of molecules
Example Values:	nozzle delay - $1.56 \pm .2ms$, probe wavelength - 24210, probe delay - $2.5575 \pm .002ms$, probe vertical - $1.12 \pm .2in$, probe focus - $1.05 \pm .1in$

4.1.2 Aligning Pump and Probe

Now that we have plenty of molecules that we can reliably hit with one laser it is time to fold in the second laser. Let's first center two apertures on the probe beam immediately before and after the windows of the main chamber. This will define a line that we want both lasers to propagate along. Now change the probe wavelength to the $J = 1$, first vibrational excitation (Q1v1) ionization. This is used because there are not enough molecules thermally populating this state to exceed our detection limit which means there's no background signal and this is an all-or-nothing game. Turn on the pump laser and rotate the quarter wave plate so you see a vibrational spectrum out of Piglet, see figure 4.3.

This alignment has been the hardest step for all previous students (including this one): don't get discouraged! A few pointers have been listed in

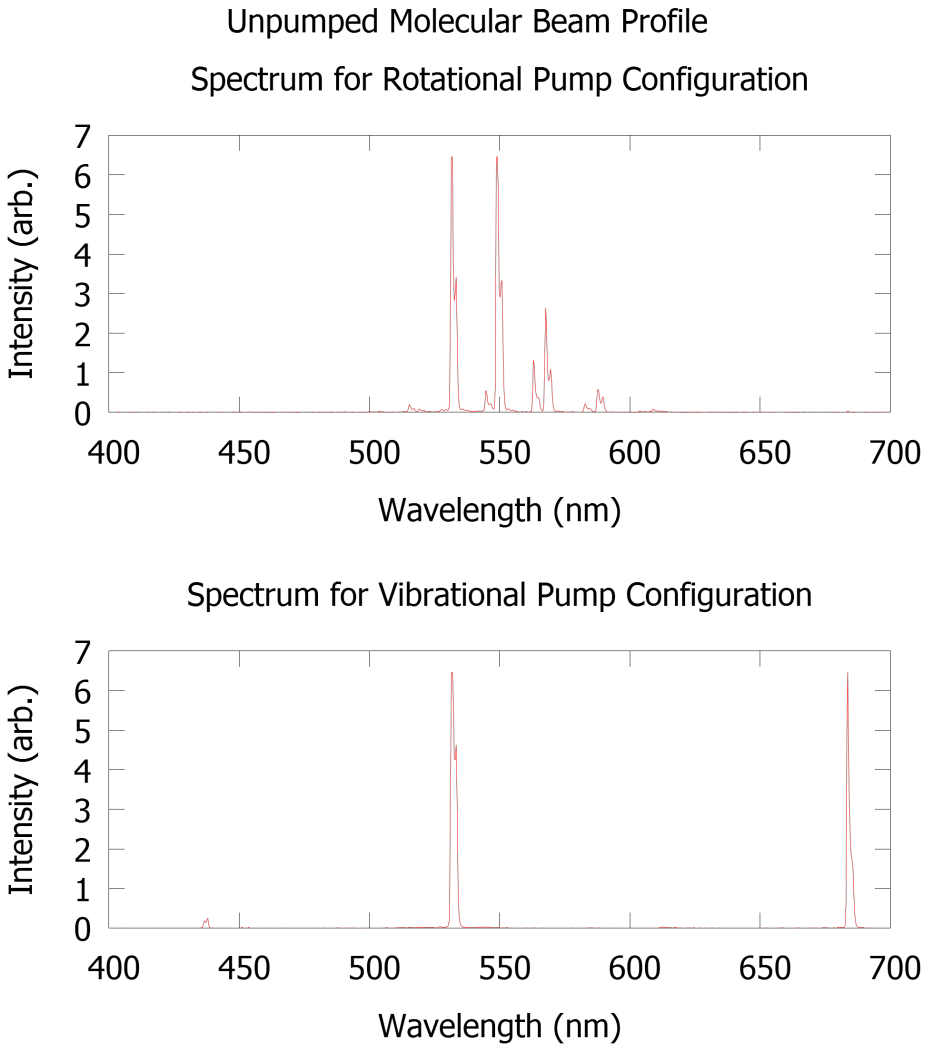

Figure 4.3: Example spectra of Piglet's output for linear and rotational pump polarizations.

Marcia Isakson's dissertation [2] but I will provide my own method here. I'll start by quoting the eminent sage Rick Sanchez: "sometimes science is a lot more art, than science. A lot of people don't get that." You are looking to make the brightest part of each laser pass through both apertures. This is a qualitative measure and thus can be subjective. It helps to have a second person make redundant observations. Start by getting the brightest part through the closer aperture with the more upstream of the last two steering prisms. Now fully dilate the first prism and using the last steering prism get that bright point through the second aperture. Go back and forth between these two until you see very little change in the throughput when the first aperture is narrowed. Repeat this for the other laser.

Now it is time to look at the MCP. Most likely you will see nothing but the switching noise (queue sad trombone). Offset the pump and probe delays by 200ns. Using the probe's vertical and up-/down-stream micrometers slowly sweep the probe up and down, back and forth in increments of a few mils (thousandths of an inch) while watching the MCP signal. You're looking for a tiny signal to start happening predictably. Once you think you have something use a card to block and unblock each laser in turn seeing if this signal disappears for *either* blocked states. If you have it, congratulations! Now start tuning it up following the same procedure as used on the molecular beam in experiment 4.3. If you don't have it, keep looking. If you're having trouble, Chris Reilly has made some animated GIFs of what a weak pumped signal looks like on the scope and these can be really helpful in preparing your

eyes for recognizing that pattern.

Now that we have aligned pump and probe we are successfully pumping molecules into an under-populated state. We also adjusted the steering prisms for the probe so the positioning on the molecular beam might no longer be optimal. The use of the apertures should have minimized this effect but keep this in mind as we move on.

4.1.3 Rotational Pumping

If you are doing a vibrationally pumped study then you don't need to read on. Let's start by switching the pump laser from vibrational mode to rotational by rotating the quarter wave plate approximately 45 degrees, adjusting for maximal rotational Raman transitions. See figure 4.3. Now change the probe wavelength to the $J = 3$, ground vibrational (Q3v0) line, at approximately 24276.9 on the PDL dial. At this wavelength you will have some background which will make optimizing the pumped signal harder at first. The alignment achieved at the vibrational should be close but not perfect: there are some slight shifts to the probe laser's trajectory caused by the change in wavelength. By shuttering the pump beam you can quickly confirm you are still aligned.

4.1.3.1 Maximizing the Pumped Signal

Start by optimizing the pumped signal by yet again iterating through probe wavelength, delay, and vertical position. You should have something

that looks like figure 4.4. Once that is done, block the pump, log the probe's micrometer positions for the pumped signal, and check the probe's vertical positioning on the molecular beam. You might find that you're high or low on it. Find the shadow and mark a value that is approximately 10 mils either above or below it, whichever seems to have more molecules to hit. This is your target value. Unblock the pump, move the probe back to the pumped position, and walk both lasers to the target value on the probe. It is easiest to move the probe until the pumped signal is weaker but not gone, then adjust the pump past the peak, and continue stepping until you get to the target. You cannot simply jump to the desired value because you might have the beams slightly crossed and would lose your pump-probe alignment. This walking procedure will have to be done again for the molecular beam axis micrometers once the surface is brought in.

It is also worthwhile to block the pump and optimizing the background for probe Q-switch delay and probe focus. You will then be able to unblock the pump and adjust the pump Q-switch delay by the same delay. Then do a pump focus scan for maximum signal. Remember that these focus scans are very gentle curves because the Rayleigh length of these lenses are close to the width of the molecular beam.

4.1.3.2 Making a Detectable Alignment

Now we need to add some optics to do alignment-based experiments. As of right now, we have circularly polarized pump light and linearly polarized

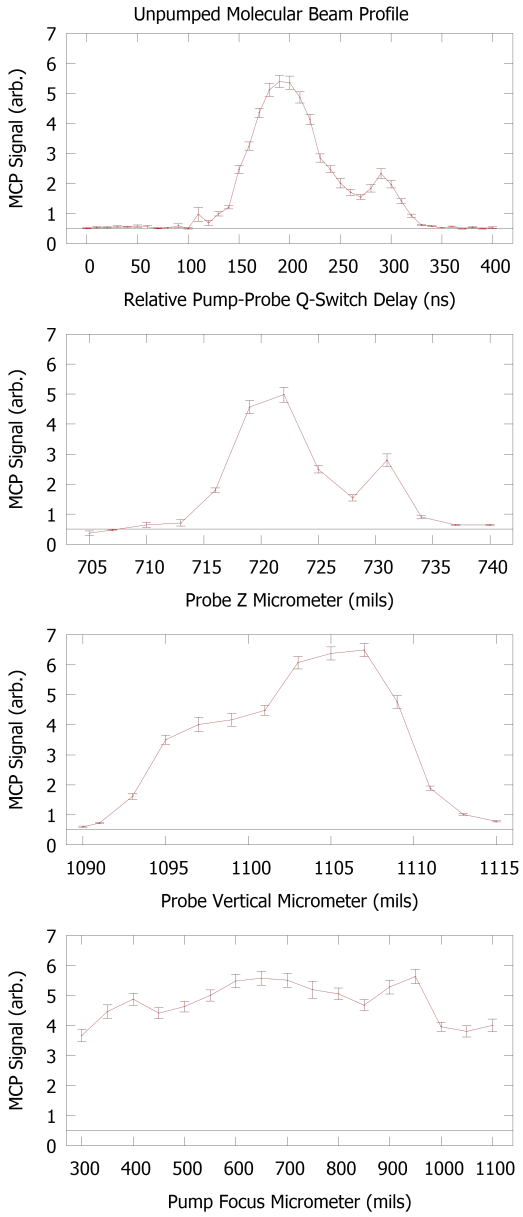

Figure 4.4: Examples of scans over all 4 probe dimensions showing the extent of the pumped molecular beam pulse. Comparing to figure 4.2, the extent of the pumped pulse is far smaller than the unpumped pulse. The odd secondary rise at longer times and Z position is not a reflection; it is an artefact of having being in the optimal vertical position. This behavior typically disappears on the second pass of tuning.

probe light incident on the molecules. The circularly polarized pump light can rotationally pump molecules but it does not have a well-defined, constant direction of polarization so it will not be preserving the initial m-state of the molecules, i.e. aligning them (for a rigorous explanation see section 2.3). To accomplish this we need linearly polarized light. One would normally use a quarter wave plate but this does not work because the relative phases of adjacent Raman wavelengths to have perpendicular polarizations, see Isakson [2]. So we instead use a polarizing beam splitter which will only transmit half of our current pump power. This now must be placed in the pump beam with special care taken to capture the rejected light with a beam block. Put it in with the laser at the lowest lasing power setting and align the retroreflection back along the beam path, it will be coming at a downward angle so it is not a concern for damaging optics upstream. Turn the laser power back up and confirm that pumping is still observed. You should remaximize pumping now.

We must be able to vary the probe polarization so we can quantify molecular alignment, see section 2.3. So we add a half wave plate to the probe beam. First verify that it is clean and take care with the motorized mount leads because they are fragile. Try to center the probe on the wave plate so that any inhomogeneity in the wave plate will not modulate your ion signal by modulation of transmittance. Verify pumping. Remaximize.

4.1.3.3 Demonstration of Alignment

At this point, we are still at the Q3v0 wavelength which, as explained in section 2.2.3, is not very sensitive to alignments of molecules. To observe alignments we must move to S3v0 which is far more sensitive, see figure 2.9. Unfortunately, the S3 linestrength is much weaker than Q3. The ion signal will reduce by 2 orders of magnitude requiring probe laser power to pick up the slack. Change the wavelength of the probe and remaximize pumping. Once that is optimized we can scan over the half wave plate angle and look for a modulation at twice the wave plate angle, which is the angle of polarization of the laser. You should see something like figure 4.5.

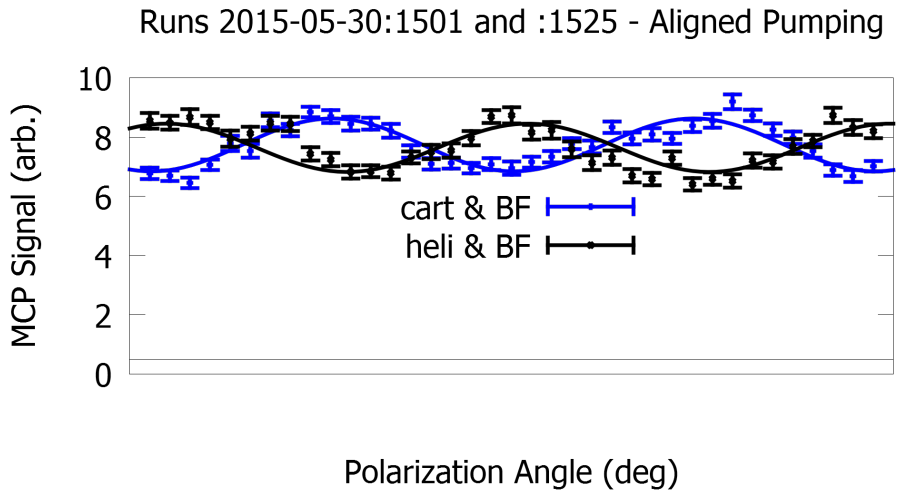

Figure 4.5: Data taken on 2015-05-30 demonstrating alignment of pumped molecules at S3. This was taken without the surface in position. The lines are the best fits to equation 4.1. A_0^2 was measured to be $-.336 \pm .030$ and $-.310 \pm .041$ for the beam splitter angles 200 and 290, respectively.

We can now apply our understanding from section 2.3 to fit this data

to an equation of the form:

$$I(\theta) = C'_d(1 + \frac{\mathcal{P}_0^2}{\mathcal{P}_0^0}\frac{A_0^{(2)}}{4}(1 + 3\cos(2\theta))) \tag{4.1}$$

where the quadrupole moment, which quantifies the degree to which the molecules are aligned, is given by $A_0^{(2)}$, and $\frac{\mathcal{P}_0^2}{\mathcal{P}_0^0}$ are the relative linestrength factors for S3, the ratio of which is plotted in figure 2.9. For the data shown in figure 4.5 the A_0^2 was measured to be $-.336 \pm .030$ and $-.310 \pm .041$ for the beam splitter angles 200 and 290, respectively.

4.1.3.4 Check for Depolarization of Alignment

As explained in section 2.3.5, molecular alignment is not constant. We will check for this phenomenon now, with the surface out of position, to demonstrate that any depolarization that occurs on the time scales we will take data at is at or below our detection limit. Results are plotted in figure 4.6.

The source of discrepancy between theory and measurements in figure 4.6 is not known. Isakson [2] suggested that an imperfect pump polarization, slight ellipticity, could cause this. However, we have analyzed our pump beam after the polarizing beam splitter and not observed any ellipticity. It is possible that this could be caused by inhomogeneity in the pump laser profile and maximum ion signal does not correspond to maximum alignment. It warrants further study.

Now we have walked through all the steps starting at not having any

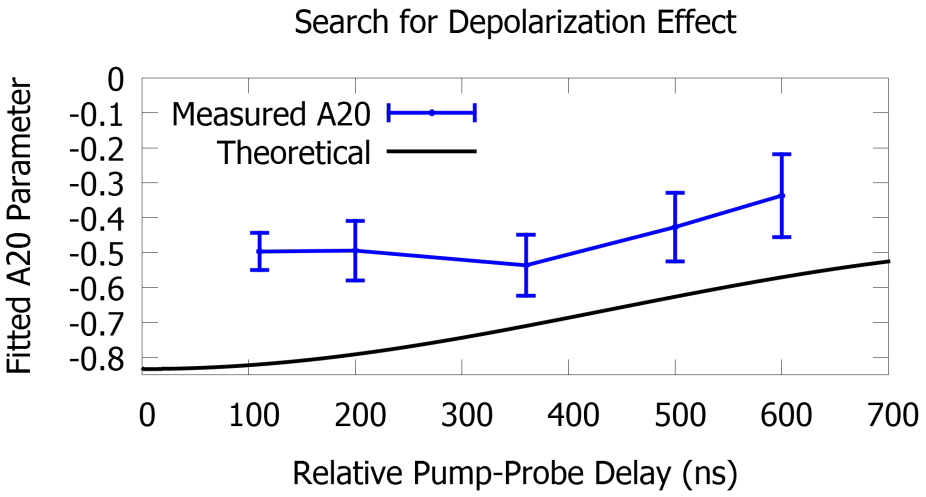

Figure 4.6: Data taken on 2014-11-05 demonstrating alignment of pumped molecules at S3 versus time between the pump and probe lasers. The experiment will be performed over the first 500ns and we see agreement within error for the quadrupole moment for these HWP scans. The plotted line shows the theoretical maximum $A_0^{(2)}$ as it precesses by the depolarization ratio plotted in figure 2.12. The source of discrepancy between theory and measurements is not known.

molecules in the main chamber to having a rotationally aligned molecule sample that we can send at a surface.

4.2 Surface Cleaning and Characterization

In this dissertation we are concerned with the molecular interactions with Silicon(100). It may seem like this chapter has ignored the silicon sample up until this point. That's true, we have. The surface is far easier to deal with experimentally than the lasers or molecular beam: it just has to sit there. If we want to make any sort of usable, general observations we need to develop a technique by which to clean it. This technique will differ for other samples but the method will likely stay the same.

4.2.1 Cleanliness Measurement: Auger Spectroscopy

We use Auger spectroscopy to detect any surface contaminants. Yes, our sample lives in an ultra-high vacuum chamber that nominally never sees pressures higher than a few nanoTorr but silicon has a habit of developing an oxide layer. And, as any scientist who uses vacuum systems will tell you, water is very hard to eliminate from a vacuum system.

In our system we will bombard the surface with 600V electrons from a filament. Behind the filament we place a filtering electrode that we will bias at the electron voltage we want to observe; this is a high-pass filter. If we also dither the voltage on the filter at a well defined frequency we can pick out the contribution of the electrons with energies close to our filter bias.

We then have a collection electrode behind the electron source (filament) that we will send the voltage of to a lock-in amplifier. The lock-in will filter for signal modulated at twice the filter's dither frequency. By sweeping the filter electrode over from a low, approximately 50V, baseline up to our filament bias of 600V, we will be able to gather data like that shown in figure 4.7. As can be seen in this plot there are several contaminants on the surface. By using reference data taken from Palmberg et al. [20] we are able to identify these contaminants as carbon, oxygen, and silicon-oxide. All that needs to go.

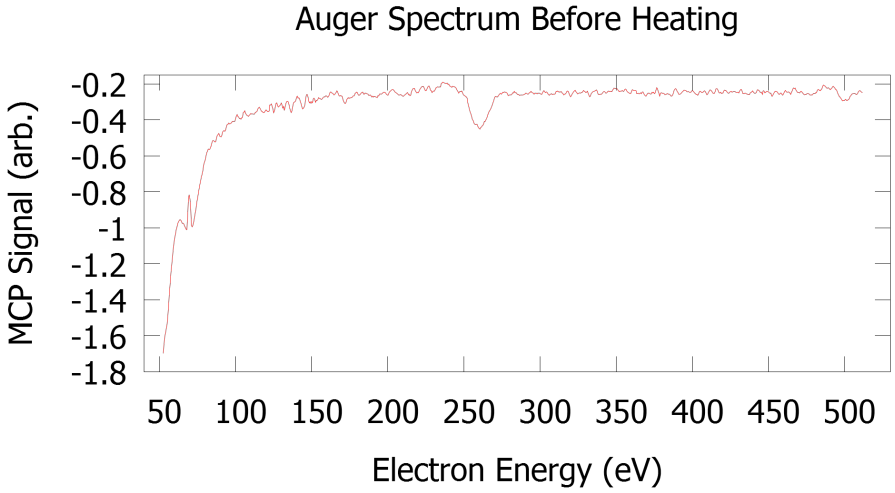

Figure 4.7: An Auger spectrum of the surface before any heating had been performed for more than a few months. Key features here are the peaks at 260eV and 500eV which correspond to carbon and oxygen, respectively [20].

4.2.2 Cleaning Procedure

First and foremost, **ensure the surface has a path to ground!** In our setup this is done through an ammeter that is then connected to one of

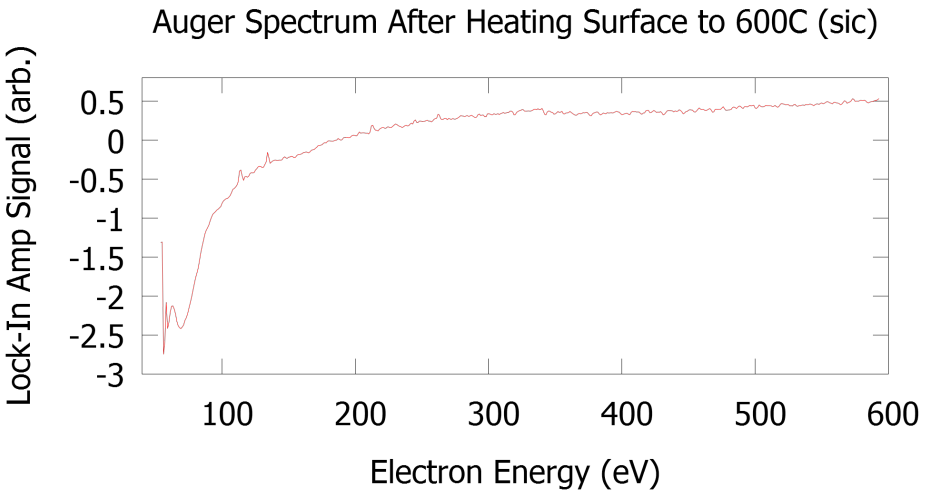

Figure 4.8: An Auger spectrum of the surface after it had been heated to 600C on the thermocouple. Compare to figure 4.7 and notice the absence of peaks at 260eV and 500eV corresponding to carbon and oxygen. In actuality the surface temperature was much hotter as evidenced by the work outlined in Zhang [21].

the flanges of the vacuum chamber. Not long after the experiments began, however, there was an incident. The cleaning procedure uses hot electrons from a filament mounted behind the surface to bombard and heat the back of the surface holder. Electrons have charge. If enough charge builds up in one place and doesn't have a path to ground, it will make one. This ablated the surface all over the chamber leaving very little surface to do science with. Ground. The. Surface.

Turn off the MCP HV supplies. See Zhang [21]. Next, turn on the AC power supply and high voltage DC power supply for the filament. These will provide the current necessary to heat the filament and give us electrons which

then will be pushed off the filament outwards, some towards the surface holder. This process is controlled by a home built temperature monitor and regulator circuit. It will only do this if it is unblanked on its front panel. Then we will increase the allowed filament current until we see a surface current of 25mA keeping a careful eye on either the main chamber pressure or the water peak if using the QMS. The goal here is to liberate unwanted elements from the surface without flooding the main chamber and stressing the vacuum pumps. Keep going until the surface current reaches 120mA and the surface thermocouple should show approximately 1050C. For these experiments the thermocouple was not in good contact and it never exceeded 600C. Regardless, cleanliness was confirmed by taking Auger spectra like the one pictured in figure 4.8.

For my experiments, the surface was cleaned before data was expected to be recorded. Sometimes this was as much as 8 hours before actual data recording began. In practice, it takes days for the silicon surface to accumulate enough contaminant to see large pressure rises in the main chamber gauge. Other, more reactive surfaces, will need more regular cleaning with a different procedure.

4.3 Surface Complications

Now it is time to move the surface into the molecular beam path. This can be tricky depending on where the lasers are in relation to the surface scattering position. A few complications are worth noting first.

4.3.1 Finding the Scattering Position of the Surface

As described in section 3.5, the surface is mounted at the end of the manipulator which is in turn mounted to the rotatable lid of the vacuum chamber. The lid is attached to a stepper motor so its angle is quantized. There are several step down gears in this system and resulting step size is approximately 4.5 arc seconds. Surface angle is not resolution limited thus there is a lid position for which the surface is perpendicular to the molecular beam well within our detection limit. Finding this position can be done by tracking the photoelectric pulse that precedes the switching noise and as a function of lid position. This signal will be maximized when the probe laser is travelling parallel to the surface. The origin of these additional photoelectrons is suspected to be laser light diffusely scattering off of the surface that ends up in the MCP housing and liberating electrons.

4.3.2 Steering Voltages with the Surface

The surface is kept grounded. Because of this the ionized molecules are "harder" to pull down into the MCP because of the image potential phenomenon. The description is more complicated for a semiconducting material such as silicon but we will not concern ourselves with that here. The workaround is to increase the steering voltages from the surface out-of-position values. If you do not remember to retune these voltages after moving the surface in position there will be no ion signal. Some example voltages for the surface in position are found in table 4.2. It was also observed that for some

ranges of voltages the ion signal could be "fracked" into two distinct arrival times. Simulations performed in SimIon by Alex Fairchild suggested this corresponded to strongly focusing the ion beam which would undergo Coulombic filamentation along the travel path. Effort was taken to avoid this phenomenon during data acquisition.

4.3.3 Positioning the Lasers Above the Surface

We will need to have the positions of the lasers be within .01 inch above the surface to do our experiments. The depolarization of pumped molecules (section 2.3.5) puts a time limit on our alignment of approximately 500 nanoseconds. The speed of our molecules being approximately .008 inches per 100 nanoseconds means that at most our molecules could be allowed to travel .032 inches before depolarization would be a significant concern. More importantly, silicon is strongly corrugated meaning reflected molecules spread out into a wide angle following the interaction. So we really need to be within .001 inches of the surface to have an observable reflection at S3.

After aligning the lasers in the free space of the chamber it is more or less random what their relative position above the surface will be. Find the z position for which the probe laser touches the surface. Touching will be evident when the MCP signal becomes saturated with an incoherent stream of particles. Touching should generally be avoided since the MCP and surface are difficult to replace and we are unsure if this contact will cause damage. Now you have an ending location for the probe and a starting location being where

the lasers are aligned for pumping. We will now employ the same walking method described in section 4.1.3.1. This is best done at Q3v0 for the copious amounts of signal reason. Also move the surface out of the scattering position so that you are not walking your pumped molecules in a potential with a steep gradient.

4.3.4 Ghost Polarization

The last and most troublesome complication due to the surface-laser proximity is a variation in the gated integrator signal as a function of probe polarization angle. This was first observed by accident by the author and proved to be vitally important for the results reported. If you have the probe laser within .01 inches of the surface, turn the molecular beam *off*, and sweep the HWP angle you will observe a modulation on the gated integrator signal on the order of the expected modulation representing perfectly aligned molecules (1 volt peak to peak on the 5mV scale). The periodicity of this modulation is the same. Thus it is not an optic absorption phenomenon but rather having to do with the polarization axis of the laser. If you further investigate this phenomenon by setting up the gated integrator on the photoelectric pulse and sweeping the HWP angle you will find the photoelectrons are being modulated at the same periodicity with a phase shift of 180 degrees. These results are shown in figure 4.9.

What appears to be happening is that as the polarization is rotated between parallel and normal to the surface, more probe light is being scattered

Experiment 4.4: Ghost Polarization

Independent Variable:	probe polarization angle
Dependent Variable:	gated integrator signal (5mV), molecular beam off
Goal:	demonstrate a "ghost" polarization
Ideal Value:	approx 1V (integrated) peak to peak

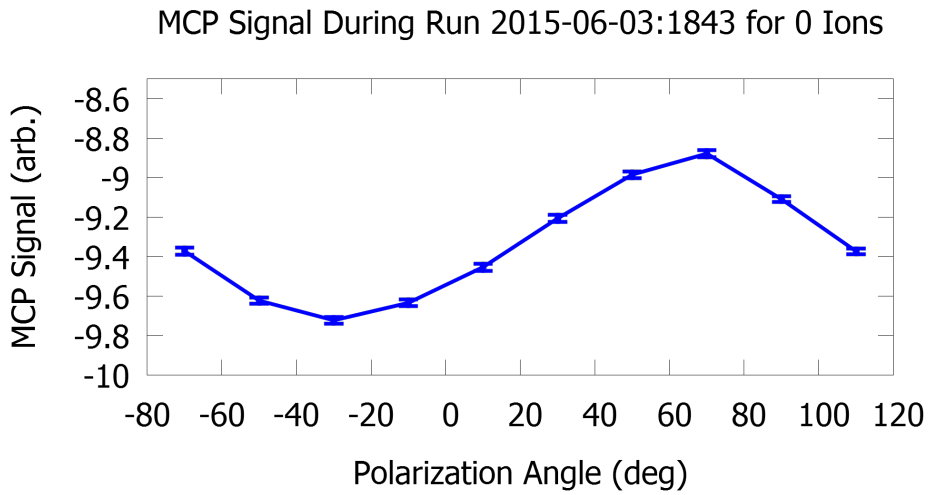

Figure 4.9: Example data taken from a run on June 3rd, 2015 of integrated MCP signal versus probe half wave plate angle (polarization) when *molecular beam is off!* Data such as these were taken for every scan to do a background subtraction. This has not yet been explained.

into the MCP where the photoelectrons are being produced. These photoelectrons are somehow affecting the DC voltage level in the ion arrival time. A few workarounds were investigated but the best control is to measure this "molecular beam off" during every data run by moving the probe Q-switch delay to well before the molecules have a chance to reach the main chamber. Then these values will be subtracted out of data taken at other delay times providing a background correction. There was a recent discovery that by turning up the switching voltage on the MCP this effect disappeared. This applies for data taken after 2015-06-10 where 950+900V were used.

4.4 Alignment of S3 Before and After Reflection

We will first explain in detail how data was collected, followed by the processing and analysis that was done before reaching a measure of alignment before and after the surface interaction.

4.4.1 Procedure of Data Collection

We will be as explicit as possible with the procedure such that future students can follow in these steps. In order to control for any slow drift of environment variables (e.g. laser power) data were taken in a repeated, rastered fashion. Here were the steps performed for each data run:

- Optimize probe laser power via KDP and BBO tuning.
- Record a time of flight scan from 150ns before the incoming signal to

50ns after the reflection signal in 15ns increments at 50 shots per point. See figure 4.10.

- Pick out the times of interest relative to pump Q-switch delay: background (nom. -6000ns), unpumped (nom. -300ns), incoming (nom. 190ns), and reflected (nom. 500ns).
- Run a script that records 30 shots at each time of interest, increments the HWP by 10 degrees from 0 to 90 degrees, then reverses HWP sweep direction, repeating this for 5 total round trips.
- We would then rotate the BS angle to the other orientation and repeat all these steps again.

Data files were written in a log fashion. That is to say that each "entry" is the result of the 30 shots at some delay and HWP angle for the third harmonic photodiode signal and MCP integrated signal. Each entry is automatically prepended with a timestamp. This will allow us to first test for any systematic laser power drifts, and if observed, correct for them. Each of these data runs took approximately 27 minutes to complete which is just when the laser power begins to measureably fall by approximately 5%. See figure 4.11. Thus before the start of another run we begin by reoptimizing laser power.

Moving forward, the analysis steps we'll need to perform are to subtract out the unpumped molecules and combine each of our 10 30 shot measurements into a single measurement at each point.

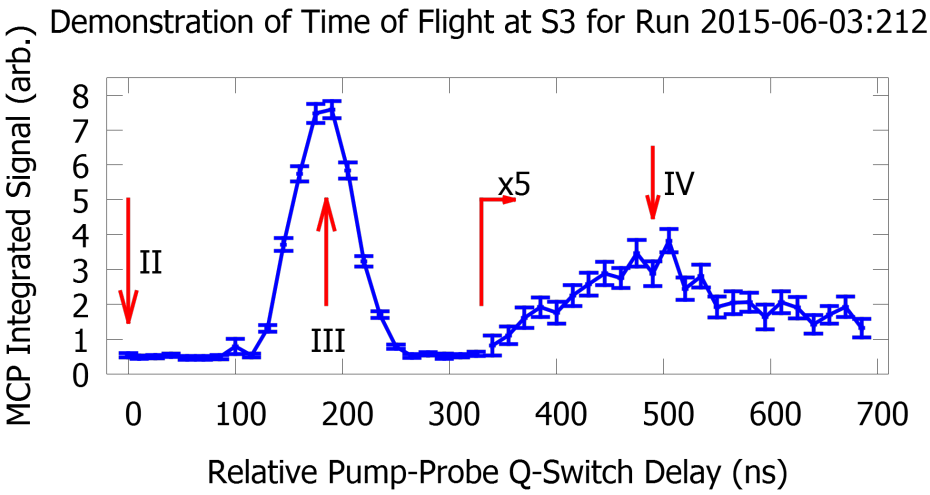

Figure 4.10: A sample time of flight scan that is used to identify the peak incoming and reflection signal delays. The points of interest, when delays for which data were recorded against HWP angle, are marked on the plot. II is the unpumped. III is the incoming. IV is the reflection. The molecular beam off time is not pictured which is $5\mu s$ before this plot begins.

4.4.2 Data Analysis

4.4.2.1 Data Processing

Our data are recorded in a rastered fashion so we first must collect together all the measurements in equivalent configurations and combine their averages and standard deviations of the mean. We will compute a combined average of these averages which will give us a value. Now to combine their standard deviations into a value representing the error. Standard deviations will combine in an RMS fashion. However, we record the standard deviation of the mean, so it differs by a factor of $\sqrt{N_{shots}}$, and we first scale by this factor. It should not take much convincing that if you wish to combine two measurements

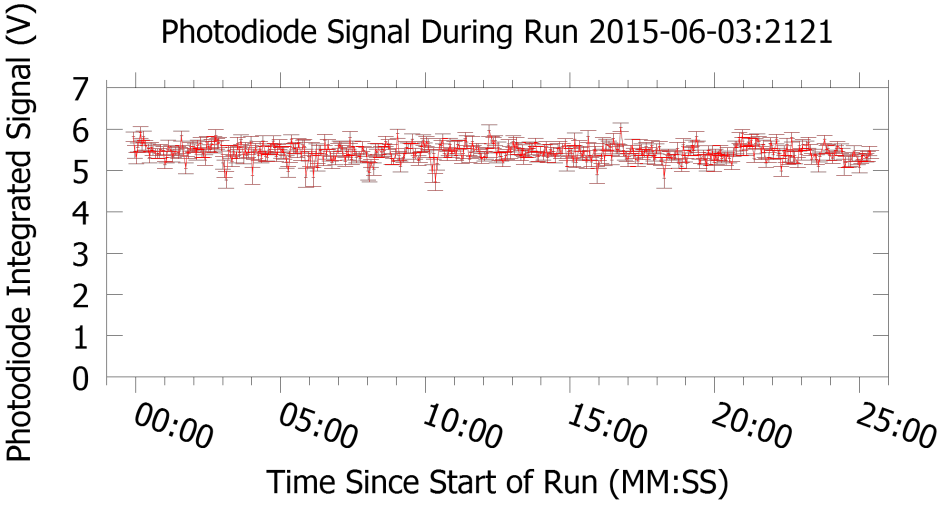

Figure 4.11: Example photodiode data taken from a run on June 3rd, 2015 of integrated photodiode signal as data was collected for the 2121 run. The starting and ending powers are within error of each other so we expect no advantage in attempting a power correction. Of note are the spontaneous downward spikes at random times. These could correspond to a missed shot or shots. This is scaled so that 0V would be 0mW laser power.

and for which the error bars do not overlap, the resulting error should be larger than the individual measurements' errors. So there's another factor in the combined standard deviation that goes as the square of the difference of each measurement's average with the average of all measurements. See equation 4.2.

$$\sigma_{total} = \sqrt{\frac{\sum_{i=1}^{N} n_i \sigma_i^2 + n_i(\mu_i - \mu_{total})^2}{\sum_{i=1}^{N} n_i}} \tag{4.2}$$

where i indexes the iteration in the run, n_i is the number of laser shots recorded on that iteration, σ is the standard deviation, μ is the mean, and N is the

total number of iterations. We will further divide by another factor of $\sqrt{N * n}$ to compute the total standard deviation of the mean. This will be our uncertainty.

It is now time to fit equation 4.1 to the incoming and reflected signals and compute A_0^2 to make quantitative comparisons. The resulting data and fits will produce something like figures 4.12 and 4.13.

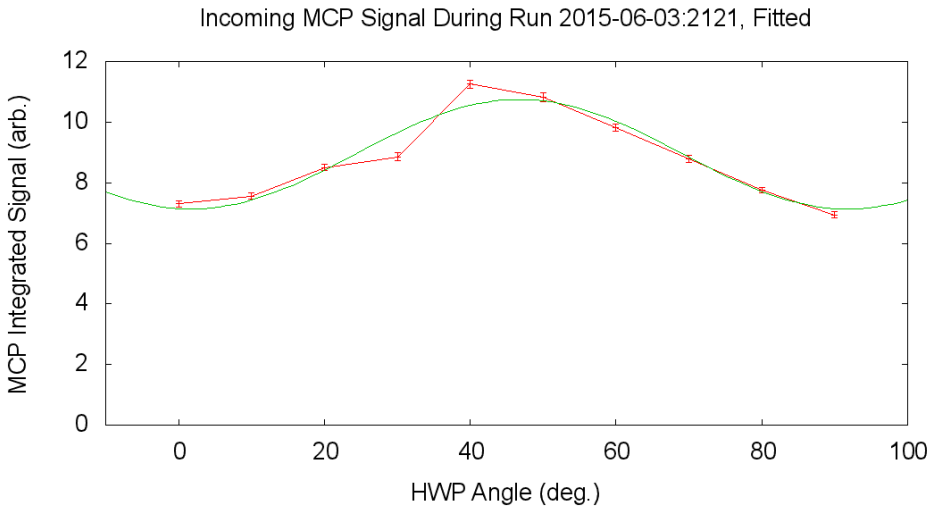

Figure 4.12: Data resulting from 300 total shots per HWP angle for the incoming signal as taken on 2015-06-03:2121. The resulting A_0^2 is -0.630 ± 0.060.

All the steps outlined in this section will be performed on all available runs and results for similar rotational states and alignments will be presented in their own sections. We will skip showing plots for each repeated run.

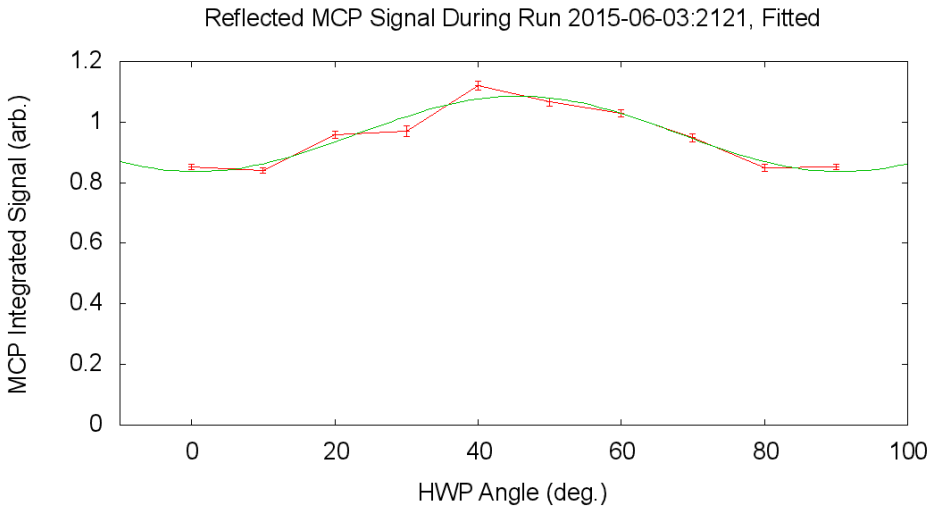

Figure 4.13: Data resulting from 300 total shots per HWP angle for the reflected signal as taken on 2015-06-03:2121. Here the fit to equation 4.1 has been performed. The resulting A_0^2 is -0.529 ± 0.080.

4.4.3 Observed Rotation of Polarization

It was discovered that the *incident* molecules' alignment appeared to be rotated out of the helcopter mode. As seen in figure 4.5, the phase between helicopter and cartwheeler modes is 90 degrees. When we perform the experiment with the surface in position, this relative phase is inexplicably shifted to -30 degrees. This was discovered in all of our runs across multiple days. It is particular to the presence of the surface. Figures 4.14 and 4.15 show this improper phasing with the best fit traces from figure 4.5 superimposed.

The fields and dipole moment of H_2 are not strong enough to cause a physical rotation of alignment. Thus we expect these observations are of a noise phenomenon with the detector. It cannot be photoelectric (as in electrons

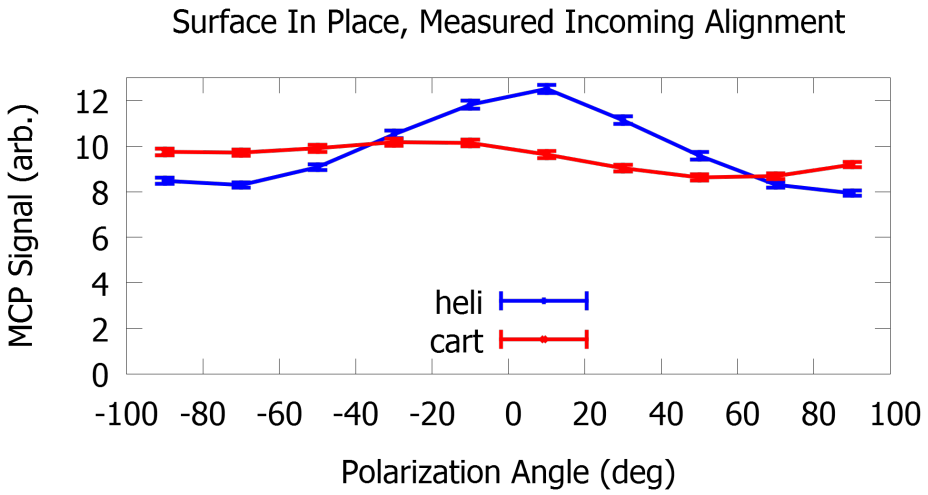

Figure 4.14: Data resulting from 300 total shots per HWP angle for the incoming signal as taken on 2015-06-03:2006 and 2015-06-03:2046. Note the -30 degree phase between the helicopter and cartwheeler modes. We suspect this is unphysical.

from the silicon) in nature because the steering voltages are kept on the order of 100V and this exceeds those kinetic energies by 2 orders of magnitude. It might be a photoelectric phenomenon from stray probe light scattering into the detector housing and making photoelectrons there. This is the same explanation we provided for the ghost polarization. The phase between the ghost and the data are not equal so we do not anticipate that we are improperly correcting for the ghost.

Very recent work, on the day of defending, Chris Reilly and Andy Hutchinson were able to observe alignment of molecules using the O-branch in free space. Then they were able to move the surface in place and make measurements of alignment before and after scattering. There is no apparent phase

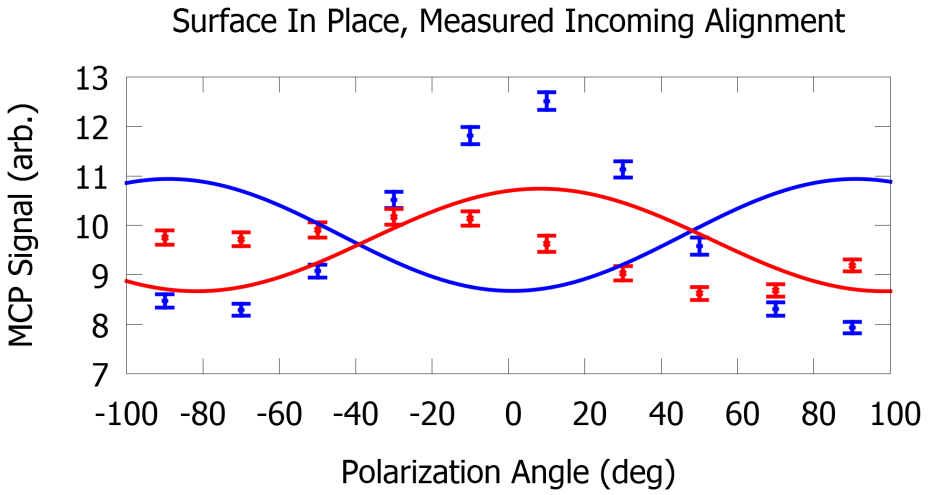

Figure 4.15: Data resulting from 300 total shots per HWP angle for the incoming signal as taken on 2015-06-03:2006 and 2015-06-03:2046 along with traces of the best fit from figure 4.5.

shift between initial configurations with and without the surface in position. This line has an overall linestrength that is half that of the S-branch but alignment sensitive linestrengths approximately 3 times larger than S. Preliminary reflection data do not show preservation of either alignment.

4.4.4 Searching for $A_0^{(4)}$ Alignment

It is expected that we should be able to detect a nonzero hexadecapole moment ($A_0^{(4)}$) to the alignment alongside the quadrupole moment (($A_0^{(2)}$). Taking data from the 2015-06-12:1843 run we fit two functional forms to this data: one with only the $A_0^{(2)}$ term and another with both the $A_0^{(2)}$ and $A_0^{(4)}$ terms. We are looking for two key differences. We would expect that $A_0^{(4)}$ will

be nonzero and the resulting reduced chi-square value should be lower since we have another parameter in the fit. These are equations 4.3. Figure 4.16 shows this test.

$$I(\theta) = C'_d(1 + \frac{\mathcal{P}_0^2}{\mathcal{P}_0^0}\frac{A_0^{(2)}}{4}(1 + 3\cos(2\theta)))$$
$$I(\theta) = C'_d(1 + \frac{\mathcal{P}_0^2}{\mathcal{P}_0^0}\frac{A_0^{(2)}}{4}(1 + 3\cos(2\theta)) + \frac{\mathcal{P}_0^4}{\mathcal{P}_0^0}\frac{5A_0^{(4)}}{64}(5 + 4\cos(2\theta) + 7\cos(4\theta))) \tag{4.3}$$

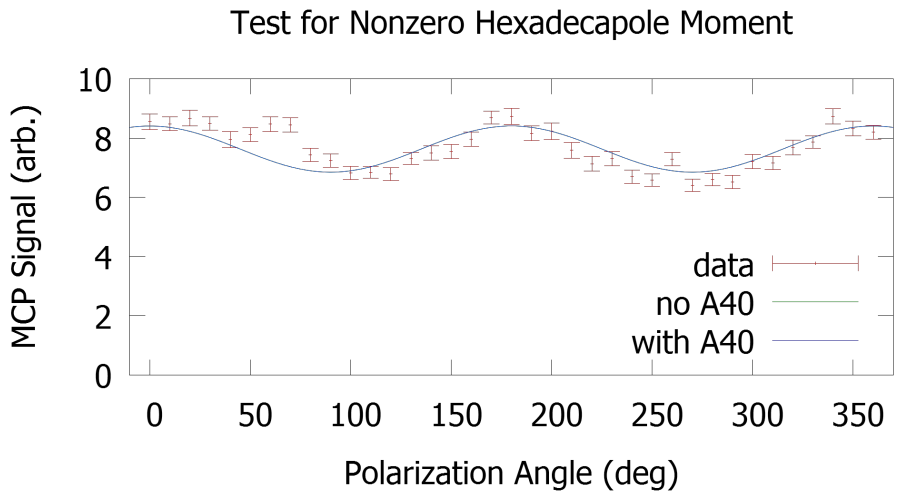

Figure 4.16: Test fits for only $A_0^{(4)}$ and $A_0^{(4)}$ with $A_0^{(4)}$. By including the $A_0^{(4)}$ term we find a value that is zero within error and an *increased* reduced chi-square.

The fitting of the two models in equation 4.3 returns the values in table 4.5.

Given these results we have ommitted fitting to an $A_0^{(4)}$ term in this

Table 4.5: Fitted alignment parameters testing for the existence of the hexadecapole moment.

	$A_0^{(2)}$	$A_0^{(4)}$	χ^2
without $A_0^{(4)}$	$-.598 \pm .062$	N/A	6.915
with $A_0^{(4)}$	$-.594 \pm .066$	$.179 \pm .340$	7.728

analysis.

4.5 Preparing the Pump for S2 Alignment

Now moving on to the other rotational state we wish to scatter off silicon. There is a disadvantage since at room temperature the Raman transition cell, Piglet, will primarily produce light capable of pumping J=1 to J=3. Looking at figure 4.18, we see the relative populations in the rotational states of ortho- and para-hydrogen as a function of temperature. J=1 clearly dominates so there are better chances for the spontaneous Raman scattering off J=1 to further seed the stimulated Raman scattering process, see section 2.2.2. If we were to cool Piglet to liquid nitrogen temperatures (77K) we would see roughly equal populations of J=0 and J=1. To further aide the J=0 population we circulate the hydrogen over a liquid-nitrogen cooled zeolite which helps either trap or convert J=1 (ortho-hydrogen) molecules. This apparatus has been detailed elsewhere, Irrgang [35] and section 3.3.1.1, so we will assume familiarity in the following discussion.

As we cool Piglet and the attached cold can, which houses the zeolite, and monitor the spectral profile of the pump laser at Piglet's exit we will see a

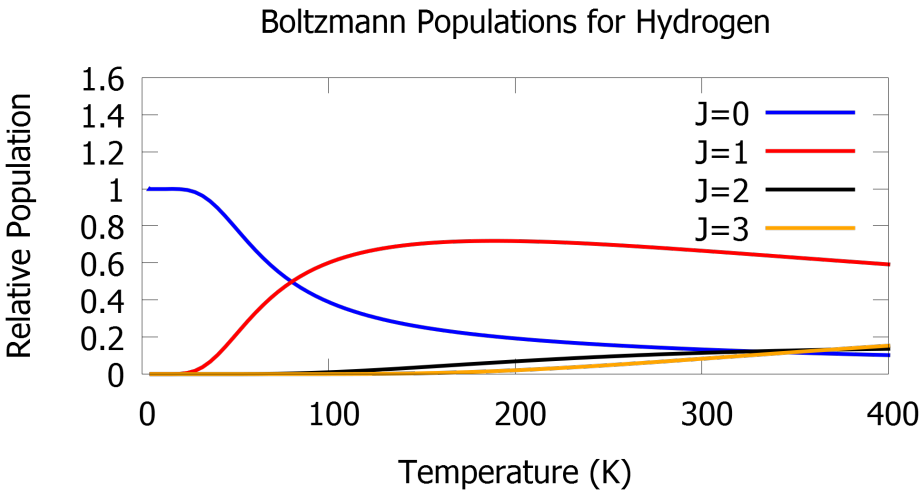

Figure 4.17: The relative populations of hydrogen, if we do not consider the nuclear spin states and how the inability to spontaneously flip these spins gives rise to the ortho- and para-hydrogen 'families'. This is recovered by use of the zeolite.

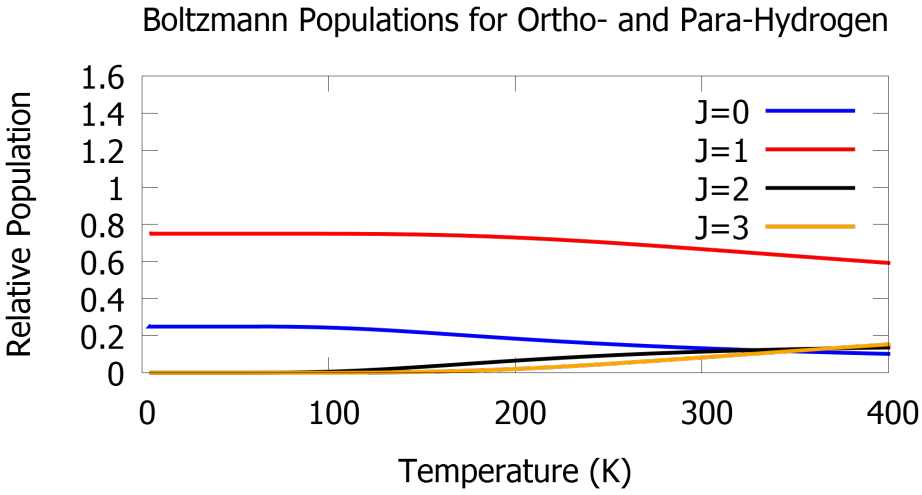

Figure 4.18: The relative populations of ortho-hydrogen and para-hydrogen. This is what we would see if we did not use the zeolite.

transition between the two profiles shown in figure 4.19. This processing takes approximately a half hour before the $J = 0 \rightarrow 2$ transition becomes brighter than the $J = 1 \rightarrow 3$. This spectrum will be preserved for up to 5 days and can be recovered by simply re-cooling Piglet and keeping the cold can isolated. Now we can send this pump light to Pooh and use it to pump the $J = 0 \rightarrow 2$ transition within the molecular beam.

4.5.1 Pressure Dependent Pumping Efficiency

As a quick aside, we would like to mention the observed pressure dependence on pumping efficiency. This experiment was performed with a warm Piglet and just looking at the $J = 1 \rightarrow 3$ pumping mode. Looking at the spectrometer we see that for higher pressures of H_2 we get more *vibrational* transitions ($\nu = 0 \rightarrow 1$) even with our circularly polarized light. We suspect that these modes are still active within the molecular beam and subsequently actively work against our pumping process by "stashing" molecules in another quantum state we are not observing. We find that a pressure of $7 \pm 1.5 PSIA$ provides the most Q3 pumped signal.

4.5.2 Scattering S2

We were unable to resolve the S2 reflection signal. We do not expect the underlying principles of alignment preservation to be different for the S2 case so this probably would not have impacted our results. If one were to do a reactive study of the $J = 2$ state they would be able to use the significantly,

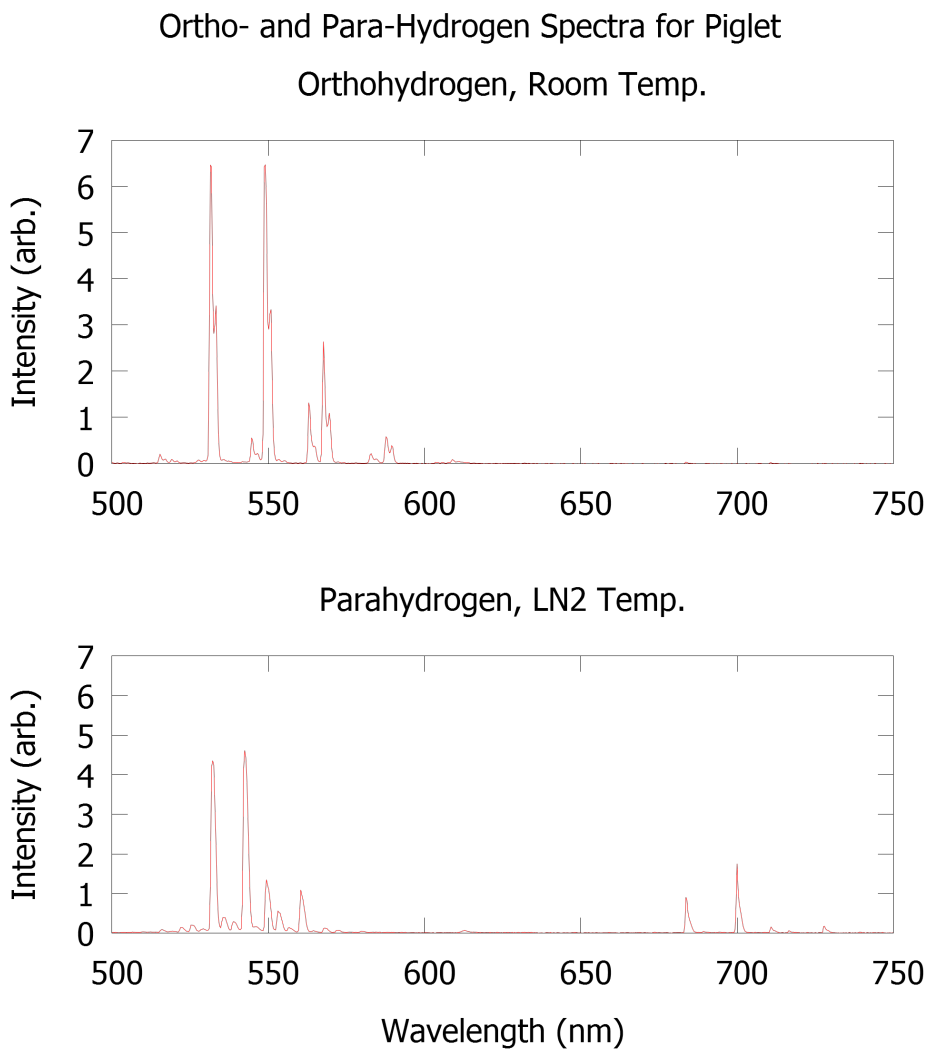

Figure 4.19: Spectra showing the pump laser wavelength composition for both the hot and cold & processed configurations. In both cases Piglet was charged to -7PSIG at the desired temperature. This means the resulting density for the cold case is higher and thus why the vibrational lines are so prevalent in the cold spectrum. It is hypothesized that if we can instead match the density we will recover our same vibration-free pumping spectrum.

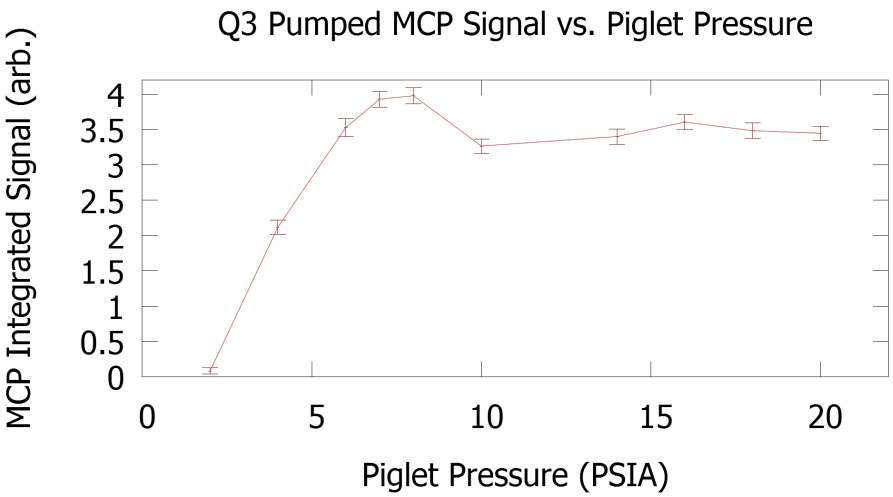

Figure 4.20: Measurements of the pumped Q3 signal as the pressure of H_2 in Piglet is increased from 0. There is an ideal value for the pressure before which the vibrational mode begins to have a measurable contribution to the spectrum. It is hypothesized that this is density phenomenon rather than a pressure phenomenon as at the same maximum pressure with a cold cell we see the vibrational lines strongly.

factor of 100, brighter Q2 line and make reflectivity measurements as Isakson did for Q3 [2].

4.6 Future Work

This work directly impacts projects looking at the possibility of alignment influencing sticking probabilities of hydrogen off of reactive surfaces, primarily palladium(111). It was the work of Marcia Isakson [2] to study this reaction at Q3 for aligned molecules. Sources of noise and complications with the apparatus prevented being able to see a statistically significant change in the reactivity for cartwheelers versus helicopters.

We would also like to see the author's original intended project, scattering of J=2 off of Pd(111), to be completed someday. As discussed in section 2.2.2.1, the alignment of the J=2 molecules will be much more constrained (only one m_J state involved) and any alignment effects will be demonstrated more readily.

Bibliography

[1] G. J. Kroes, E. J. Baerends, and R. C. Mowrey, "Six-dimensional quantum dynamics of dissociative chemisorption of H_2 on Cu(100)," *J. Chem. Phys.*, vol. 107, pp. 3309–3323, 1997.

[2] M. J. Isakson, "The Effects of Alignment on the Dissociation of H_2 on Pd (111)," Doctoral, The University of Texas at Austin, 2002.

[3] G. R. Darling and S. Holloway, "The Dissociation of Diatomic Molecules at Surfaces," *Reports on Progress in Physics*, vol. 58, pp. 1595–1672, 1995. [Online]. Available: http://iopscience.iop.org/0034-4885/58/12/001

[4] M. Durr and U. Hofer, "Dissociative Adsorption of Molecular Hydrogen on Silicon Surfaces," *Surface Science Reports*, vol. 61, no. 12, pp. 465–526, Dec. 2006. [Online]. Available: http://linkinghub.elsevier.com/retrieve/pii/S0167572906000896

[5] M. Durr, M. B. Raschke, and U. Hofer, "Effect of beam energy and surface temperature on the dissociative adsorption of H 2 on Si(001)," *Journal of Chemical Physics*, vol. 111, no. 23, pp. 10 411–10 414, 1999.

[6] G. Scoles, *Atomic and Molecular Beam Methods*, 1992.

[7] C. Crespos, H. F. Busnengo, W. Dong, and a. Salin, "Analysis of H[sub 2] dissociation dynamics on the Pd(111) surface," *The Journal of*

Chemical Physics, vol. 114, no. 24, p. 10954, 2001. [Online]. Available: http://link.aip.org/link/JCPSA6/v114/i24/p10954/s1\&Agg=doi

[8] S. F. Shane, K. W. Kolasinski, and R. N. Zare, "Recombinative desorption of H_2 on Si(100)-(21) and Si(111)-(77): Comparison of internal state distributions," *The Journal of Chemical Physics*, vol. 97, no. 100, p. 1520, 1992. [Online]. Available: http://link.aip.org/link/JCPSA6/v97/i2/p1520/s1\&Agg=doi

[9] A. E. Siegman, *Lasers*, 1986.

[10] V1adis1av, "Stimulated Emission," p. 1, 2008. [Online]. Available: http://commons.wikimedia.org/wiki/File:Stimulated_Emission.svg

[11] Lakkasuo, "Laser Cavity," p. 1, 2010. [Online]. Available: http://commons.wikimedia.org/wiki/File:Lasercons.svg

[12] Quanta-Ray, "Quanta-Ray PDL-3 Instruction Manual," p. 150, 1980.

[13] R. Boyd, *Nonlinear Optics*, 3rd ed. Boston: Academic Press, 2008.

[14] J. Steinfeld, *Molecules and Radiation: An Introduction to Modern Molecular Spectroscopy*, 2nd ed. Dover, 2005.

[15] T. Hanisco and A. Kummel, "Resonantly Enhanced Multiphoton Ionization of N2 a"1Sigma_g_+ ¡- X1Sigma_g_+. Alignment and Orientation Measurements." *J . Phys. Chem.*, vol. 96, pp. 2982–2993, 1992.

[16] F. Zotter, "Spherical Harmonics," p. 1, 2013. [Online]. Available: http://commons.wikimedia.org/wiki/File:Spherical_Harmonics_deg5.png

[17] M. Rutkowski and H. Zacharias, "Corrigendum to Depolarisation of the spatial alignment of the rotational angular momentum vector by hyperfine interaction [Chem. Phys. 301 (2004) 189]," *Chemical Physics*, vol. 310, no. 1-3, pp. 321–322, Apr. 2005. [Online]. Available: http://linkinghub.elsevier.com/retrieve/pii/S0301010404006378

[18] A. Barron, "Structures of Element and Compound Semiconductors," p. 1, 2009. [Online]. Available: http://cnx.org/content/m23905/1.6/

[19] J. Stuart, "Documentation for Digital Delay Generator Mk . II a . k . a . DDG Dox ," Tech. Rep., 2014.

[20] P. W. Palmberg, G. E. Riach, R. E. Weber, and N. C. MacDonald, *Handbook of Auger Electron Spectroscopy.* Physical Electronics Industries, Inc., 1972.

[21] S. Zhang, "Effects of Surface Temperature in Gas-Surface Interaction : Quantum-State Resolved Studies of H 2 Scattering from Si(100)," Ph.D. dissertation, University of Texas, Austin, 2010.

[22] J. E. Lennard-Jones, "Processes of adsorption and diffusion on solid surfaces," *Transactions of the Faraday Society*, vol. 28, p. 333, 1932. [Online]. Available: http://xlink.rsc.org/?DOI=tf9322800333

[23] J. T. Law, "Adsorption of Hydrogen on Silicon," *The Journal of Chemical Physics*, vol. 30, no. 6, p. 1568, 1959. [Online]. Available: http://scitation.aip.org/content/aip/journal/jcp/30/6/10.1063/1.1730240

[24] M. C. Downer, "Lecture Notes for Phy395K: Nonlinear Optics and Lasers," p. 300, 2011.

[25] D. Griffiths, *Introduction to Electrodynamics*, 1999.

[26] G. W. F. Drake, *Atomic, Molecular, & Optical Physics Handbook*, 1996.

[27] D. Griffiths, *Quantum Mechanics*, 2nd ed. Upper Saddle River: Prentice Hall, 2005.

[28] G. O. Sitz, "Gas surface interactions studied with state-prepared molecules," *Reports on Progress in Physics*, vol. 65, no. 8, pp. 1165–1193, 2002. [Online]. Available: http://stacks.iop.org/0034-4885/65/i=8/a=202?key=crossref.b37b65642057ba19e671cc9e15596b69

[29] RGrey, "Understanding the virtual states referenced in multiphoton absorption studies," p. 1, 2014. [Online]. Available: http://physics.stackexchange.com/questions/89131/understanding-the-virtual-states-referenced-in-multiphoton-absorption-studies

[30] A. C. Kummel, G. O. Sitz, and R. N. Zare, "Determination of population and alignment of the ground state using two-photon nonresonant excitation." *J. Chem. Phys.*, vol. 85, no. December, pp. 6874–6897, 1986.

[31] ——, "Determination of Orientation of the Ground State using Two-Photon Non-Resonant Excitation," *Journal of Chemical Physics*, vol. 88, no. 11, p. 6707, 1988.

[32] G. O. Sitz and R. L. Farrow, "Preparation and decay of alignment in N2 (v=1)," *The Journal of Chemical Physics*, vol. 101, no. 6, p. 4682, 1994. [Online]. Available: http://link.aip.org/link/JCPSA6/v101/i6/p4682/s1\&Agg=doi

[33] V. Aquilanti, D. Ascenzi, D. Cappelletti, and F. Pirani, "Magnetic analysis of nearly effusive and moderately supersonic beams of oxygen molecules," *International Journal of Mass Spectrometry and Ion Processes*, vol. 149-150, pp. 355–371, 1995.

[34] G. O. Sitz, "H_2 Linestrength Polarizations," 1998.

[35] M. E. Irrgang and G. O. Sitz, "Stimulated Raman Scattering and mixtures of Ortho- and Para-Hydrogen," 2010.